Shibaura Institute of Technology

Graduate School of Engineering and Science
Regional Environment Systems [Environmental Materials Science and Engineering]

DOCTORAL DISSERTATION

Study on Fabrication Method of High Performance MgB_2 Bulk Superconductor and Improvement of Pulse Magnetization Property

Joseph Longji Dadiel

Declaration

I certify that the intellectual content of this thesis is the product of my own work and that all the assistance received in preparing this thesis and sources have been specified in the text and acknowledged. Except where specific reference is made to the work of others, the contents of this dissertation is original and have not been submitted in whole or in part for consideration for any other degree or qualification in this, or any other university.

Joseph Longji Dadiel

March 2022

Acknowledgements

First of all, I remain grateful to my supervisor, Professor Naomichi Sakai for his exceptional guidance and supporting me throughout the course of my doctoral program. He motivated me, gave me the opportunity to collaborate with other experts in the field. Thank you so much for the opportunities you have opened for me.

Secondly, I would like to thank the former President of Shibaura Institute of Technology, Professor Masato Murakami for supporting me in the course of this journey towards my Ph.D. pursuit. Accepting me into the superconducting material research laboratory at Shibaura Institute of Technology has been the best thing that has happen to me in my academic career. I would also like to specially appreciate Prof. Miryala Muralidhar who initially supported me in my previous research of which some important data were considered for more developments in this work. Also, I would like to thank Prof. Paolo Mele, Prof. Akito Takasaki for their valuable guidance, support, advice, and constructive criticism to make this work better.

I would like to express my deepest thanks to Prof Tetsuo Oka, who also supported my work and provided the ground for me to collaborate with other research experts, most especially the Yokoyama labs at Ashikaga University with the guidance and support of Prof Kazuya Yokoyama. I gratefully acknowledge the support, suggestions and guidance of Dr. Hiraku Ogino and Dr. S Pavan Kumar Naik who provided most of the infrastructure for the completion of a chapter of this work at the Advance Institute of Science and Technology (AIST) Tsukuba Labs. I wouldn't have achieved this without you. Thank you very much for supporting me. Also my sincere gratitude of support goes to Dr. Pawel Peckowski of the Cardinal Stefan Wyszynski University who gave me the opportunity to collaborate with the Poland research group.

I would also appreciate my family most especially the Dadiels, and some friends for their motivation, prayers and support throughout my studies at Shibaura Institute of Technology. The accomplishment of this project will not be complete without you.

Dedication

This document is dedicated to God Almighty.

Abstract

This thesis is focused on the processing techniques of improving the superconducting performance of polycrystalline and high density magnesium diboride (MgB_2) as well as the effective cost of production. This intermetallic material is highly attractive for practical applications because of its excellent and unique features which ranges from it's simple stoichiometry and high critical temperature for a non-oxide superconductor, low density, high upper critical field and strong trapped field among other features for the samples produced in the bulk form. Several techniques have been suggested and researched to improve the density and connectivity, grain sizes with the resulting effect on the critical current density (J_c), to be utilized for practical applications of the bulk such as magnetic resonance imaging (MRI), nuclear magnetic resonance, trapped field magnets, motors and generators, magnetic separations, flywheel storage, levitation, innovative applications such as biomedical. Classically, most of the samples prepared by conventional powder metallurgy leads to low relative densities which affect the final properties of the bulk materials. Different methods have been used for enhancing the grain refinement, connectivity and densifying the material such as high pressure sintering, hot isostatic pressing (HIP), hot compactions, and nonconventional field assisted sintering techniques (FAST) or spark plasma sintering (SPS) process. However, the challenges in the optimization of the microstructures and material density for effective self-field J_c improvement and high trapped field is still at large.

As a remedy to the aforementioned issues, suggested possible methods were used in this thesis to enhance the critical current density and flux pinning of bulk MgB_2 as well as connectivity between grains. In order to improve the bulk superconducting performance, two different perspectives were considered; the material development aspect and the application aspect. In the material aspect of this thesis, the chemical doping technique was initially adopted to improve the flux pinning properties of MgB_2 bulk superconductor material, these techniques were effective for the samples produced at the course of this chapter. Three different techniques were discussed in order to compare the effect of different additives on the superconducting performance of bulk MgB_2 superconductor. The first series was based on nanoscopic diamond powder addition. Optimization of the nanoscopic diamond powder at 775 ^oC sintering temperature for 3 hours played a vital role in improving the flux pinning performance of the bulk MgB_2 material resulting in high self-field J_c at ~300 kA/cm^2 for 0.8 wt.% of nanoscopic diamond addition. To further improve the superconducting performance of the bulk, synthesis of the product by silver (Ag) addition using the same processing technique and conditions was employed. XRD and SEM micrograph analyses indicated AgMg secondary phase as nanoparticles embedded in the MgB_2 matrix in the samples with Ag addition. Optimization was achieved for 4.0 wt.% added Ag which showed improved self-field J_c of 398 kA/cm^2 at 20 K. The study showed Ag addition contributed to formation of more effective pinning medium in bulk MgB_2 and helps to further improve

performance of the bulk. Nanodiamond and Silver are very expensive raw materials for bulk MgB_2 synthesis which could further make the final product costlier. To solve this problem, a cost effective technique of ball-milled charcoal powder within the range of 60-100 nm sizes was considered. Doping was done on MgB_2 with resulting optimization at 0.4 % charcoal doping for a superconducting J_c improvement to about 467 kA/cm^2.

In order to achieve high performance by simultaneous structural control and density enhancement of bulk MgB_2 for practical applications, this work suggests synthesis of bulk MgB_2 samples via spark plasma sintering *in-situ* and also utilized *ex-situ* processing by optimizing the sintering temperatures and observing the effects on the bulk density and microstructure. The microstructural characterization by FE-SEM reveals some Mg-O inclusions for the *ex-situ* process, better grain connectivity and the size of the MgB_2 grain was statistically analyzed to be within the range of ~100 to 120 nm. The distribution of the generated impurity phases which occurred due to the effect of our processing condition were studied by transmission electron microscope. The onset of the critical temperature, T_c determined by superconducting quantum interference magnetometer was ~38 K showing slight effect of secondary phases in the sample microstructure. The critical current density, J_c is influenced by the sintering temperature for both *ex-situ* and *in-situ* process exhibiting $J_{c,s}$ of the order ~500 kA/cm^2 at self-field and 20 K. The density by SPS *in-situ* is superior to the previous reports by SPS in-situ processing. This work urge that the flux pinning was highly promoted by the interactive contributions of the grain refinements and controlled minor secondary phases towards improving the superconducting performance compared to the bulk MgB_2 synthesized by the conventional methods.

To complement the application aspect of this study, a modified bulk MgB_2 was subjected to trapped field measurements via pulse field magnetization (PFM). Degrading of trapped fields B_T in bulk MgB_2 superconductor due to the occurrences of flux jumps has been a lingering challenge due to the anisotropic thermal property of bulk MgB_2. This section of the thesis presents the method for characterizing the propagation of the magnetic flux in an artificially drilled MgB_2 bulk superconductor fabricated via spark plasma sintering (SPS) which was achieved by studying the effect of applied fields, B_A on the bulk MgB_2 embedded with low melting alloy of Bi-In-Sn alloy and aluminum rods within the holes. The bulk MgB_2 sample was redesigned to enhance both the thermal properties and to suppress flux jumps during pulse applications. The magnetic flux dissipation, the flux motion, and performance by evaluation of the capture field ratio B_T/B_P were discussed. We achieved 0.7 T trapped field at 1.8 T applied field without flux jumps which is a vital breakthrough for high magnetic field applications. This study helps to solve the flux jump problem in the bulk superconductor resulting from poor heat dissipation. This is an experimental breakthrough that supports existing simulation studies and reports giving way for more prospects for high field applications in the development of bulk MgB_2 superconductors.

List of Publications:

A. Achievements from Doctoral Course:

[1] **Dadiel J.L**, N. Sakai, K. Yokoyama, K. Takemura, M. Miryala, M. Murakami, Jacques Noudem "Field-Trapping Performance of Drilled MgB2 Bulk Superconductor Embedded with Bi-In-Sn Alloy and Al-rod in Pulse-Field Magnetization Processes*" IEEE Transactions on Applied Superconductivity* (*Published in early access area on IEEE Xplore, Online ISSN: 1558-2515)*

[1] **Dadiel, J.L.;** Naik, S.P.K.; Pęczkowski, P.; Sugiyama, J.; Ogino, H.; Sakai, N.; Kazuya, Y.; Warski, T.; Wojcik, A.; Oka, T.; Murakami, M. "Synthesis of Dense MgB_2 Superconductor via In-Situ and Ex-Situ Spark Plasma Sintering Method" *Materials* 2021, Vol. 14, Issue 23, 7395

[2] Paweł Pęczkowski, Piotr Zachariasz, Marcin Kowalik, Waldemar Tokarz, Sugali Pavan Kumar Naik, Jan Żukrowski, Cezariusz Jastrzębski, **Longji Joseph Dadiel**, Wojciech Tabiś, Łukasz Gonde" Iron diffusivity into superconducting $YBa_2Cu_3O_{7-\delta}$ at oxygen-assisted sintering: structural, magnetic, and transport properties", *Journal of the European Ceramic Society*, Vol. 41, Issue 14, 2021, Pages 7085-7097

[3] T Oka, M Furusawa, K Sudo, **L Dadiel**, N Sakai, H Seki, M Miryala, M Murakami, T Nakano, M Ooizumi, K Yokoyama, M Tsujimura," Feasible waste liquid treatment from electroless nickel plating by intense magnetic field of HTS bulk magnets" *The Korean Society of Superconductivity and Cryogenics* 2021**,** Volume 23, Issue 3, pages 37-40

[4] Rémi Dorget, Kévin Berger, **J Longji Dadiel**, Kimiaki Sudo, Naomichi Sakai, Tetsuo Oka, Masato Murakami, Jean Lévêque "Modelling of the pulse field magnetization of a REBaCuO bulk with a superconducting weld" *IOP J. Phys. Conf. Ser.* 2021, 2043. 012001

[5] Tetsuo Oka, Kengo Yamanaka, Kimiaki Sudo, **Longji Dadiel**, Jun Ogawa, Kazuya Yokoyama, Walfgang Häßler, Jacques Noudem, Kévin Berger, Naomichi Sakai, Muralidhar Miryala, Masato Murakami "Shielding Effect on Flux Trapping in Pulsed-Field Magnetizing for Mg-B Bulk Magnet" *IOP Journal of Physics: Conf. Ser.* 2021, 1975. 012019

[6] N Sakai, T Oka, K Yamanaka, **L Dadiel**, H Oki, J Ogawa, S Fukui, J Scheiter, W Häßler, K Yokoyama, J Noudem, M Miryala and M Murakami *"Occurrence of Flux Jumps in MgB_2 Bulk Magnets during Pulse-Field Magnetization"*, *IOP Journal of physics: Conf.*

Series 2020, 1559 012057

[7] T Oka, A Takeda, H Oki, K Yamanaka, L Dadiel, K Yokoyama, W Häßler, J Scheiter, Naomichi Sakai, Masato Murakami "Magnetic Flux Trapping and Flux Jumps in Pulsed Field Magnetizing Processes in REBCO and Mg-B Bulk Magnets", *IOP, Journal of Physics: Conf. Ser.* 2020, 1590 012025

[8] Tetsuo Oka, Akira Takeda, Oki Hayami, Jun Ogawa, Satoshi Fukui, Juliana Scheiter, Wolfgang Hasler, Kazuya Yokoyama, **Longji Dadiel,** M. Miryala, N. Sakai, M. Murakami, Jacques Noudem "Study on Magnetic Flux Dissipation and Field-Trapping Performance of HTS Bulk-Shaped Magnesium Diboride in Pulse-Field Magnetizing Processes" *IEEE Transactions on Applied Superconductivity,* 2019, **29** 8678817

B. Contributed Master's Course Work:

[1] **J. Longji Dadiel**, M. Muralidhar, S Pavan Kumar Naik, M. Murakami (2018), "Processing and Characterization of Charcoal Added Bulk MgB_2 Superconductor", *IOP Journal of Physics: Conf. Ser.* 2019, 1293 012047

[2] **J. Longji Dadiel**, M. Muralidhar and M. Murakami (2018), "Improved Superconducting Performance of Ag-added nano-diamond doped MgB_2", *Superconductivity and Particle Accelerators SPAS* 2019**,** Proc. SPIE 11054

[3] **J. Longji Dadiel**, M. Muralidhar and M. Murakami, "Flux Pinning and Superconducting Properties of MgB_2-Diamond nanocomposites", International Symposium on Superconductivity, *IOP Journal of physics Conf. Ser.* 2018 **1054** 012052

Presentations

A. During Doctoral Course:

[1]. ***Oral***, **J. Longji Dadiel**, N. Sakai, K. Takemura, T. Oka, M. Miryala, and M. Murakami "Improved Connectivity of MgB_2 Superconductor via *In-Situ-Ex-Situ* Co-Synthesis" International Workshop on Processing and Application of Superconducting Bulk Materials (PASREG 2021) Shanghai Nov. 11 – 14, 2021

[2]. ***Oral***, **J. Longji Dadiel**, N. Sakai, K. Takemura, T. Oka, K. Yokoyama, M. Miryala, and M. Murakami, "Field trapping Performance of Drilled MgB_2 Bulk Superconductor Filled

with Bi-In-Sn Alloy and Al-rod using Pulse Field Magnetization Process" 15th European Conference on Applied Superconductivity (EUCAS 2021) Moscow, Russia September 5 – 9, 2021

[3]. ***Oral***, **J. Longji Dadiel**, N. Sakai, T. Oka, M. Miryala, and M. Murakami. Comparative Study of the Effect of Nanodiamond and Charcoal on the Superconducting Properties of MgB_2 Bulk Superconductor" 33rd International Symposium on Superconductivity" (ISS 2020), Tsukuba, Japan Dec. 1 – 3, 2020

[4]. ***Poster Presentation***, **J. Longji Dadiel,** M. Miryala, and M. Murakami. Optimization of Sintering Conditions for Synthesizing Dense MgB_2 bulk Superconductor via Ex-situ Spark Plasma Sintering" 32nd International Symposium on Superconductivity" (ISS 2019), Kyoto, Japan, Dec. 3 – 5, 2019

[5]. ***Poster Presentation***, Jun Sugiyama, M. Miryala, **J. Longji Dadiel,** N. Sakai, T. Oka, K. Yokoyama, H. Ogino, S. Pavan Kumar Naik, and M. Murakami, "Improved Performance of MgB_2 Superconductor Produced via Combination of In-situ and Ex-situ Method" 32nd International Symposium on Superconductivity" (ISS 2019), Kyoto, Japan, Dec. 3 – 5, 2019

B. During Master Course:

[6]. ***Poster Presentation*** **J. Longji Dadiel**, S. Srikanth, M. Miryala, S.P.K Naik and M. Murakami "Processing and Characterization of Charcoal Added Bulk MgB_2 Superconductor" 31st International Symposium on Superconductivity (ISS 2018), Tsukuba, Japan, Dec. 12 -14, 2018

[7]. ***Invited Talk***, **J. Longji Dadiel,** M. Miryala, and M. Murakami "Improved Superconducting Properties of Ag-Added Nano-diamond Doped MgB_2" Superconductivity and Particle Accelerators (SPAS 2018) Krakow, Poland, Nov. 27 – 29, 2018

[8]. ***Oral***, **J. Longji Dadiel,** M. Miryala, and M. Murakami "Improved Superconducting Properties of MgB_2 Bulk Superconductor" 12th South-East Asian Technical Students Consortium, (SEATUC 2018), Yogyakarta, Indonesia, March 12 – 13, 2018

[9]. ***Poster Presentation***, **J. Longji Dadiel**, M. Miryala, and M. Murakami. Flux Pinning and Superconducting Properties of MgB_2-Diamond Nanocomposites. The 30th International Symposium on Superconductivity (ISS 2017) Tokyo, Japan, Dec. 13 – 15, 2017

[10]. ***Poster Presentation***, **J. Longji Dadiel**, M. Miryala, and M. Murakami "Flux Pinning and Superconducting Properties of MgB_2-Diamond Nanocomposites" 10^{th} International Workshop on Processing and Application of Superconducting Bulk Materials (PASREG 2017), Tokyo, Japan, Dec. 11 – 12, 2017

TABLE OF CONTENTS

CHAPTER I

INTRODUCTION

1.0 General Overview

Superconductivity is a phenomenon showing several interesting characteristic properties viz: zero resistance below a critical temperature (T_c), the Meissner Effect (perfect diamagnetism) below a critical field (H_c), The Josephson Effect and so on. Superconductivity is a term used to describe the phenomenon of strongly correlated behavior in a many-body system, which is important and is still an unsolved mystery in physics. The onward discovery of surprising properties in this field drives experimentalists and theorists to understand and complete the puzzles [1]. Superconductivity in magnesium diboride (MgB_2) was discovered by Akimitsu *et al.* in 2001. However, research on MgB_2 itself began over one hundred years ago [1][2], shortly after Kamerlingh Onnes' discovery of superconductivity in mercury [3]. MgB_2 was first appeared in the literature in 1881 as a product of the reduction of B_2O_3 with Mg [2]; however, at the time it was identified as Mg_3B_2. In 1954, Russell [4] determined the lattice parameters of MgB_2 by using X-ray diffraction (XRD), thereby fixing the composition at MgB_2 for the lowest boride phase based on geometric constraints. The observation was then confirmed by many authors [1], who categorized MgB_2 into a P6/mmm space group. A transition temperature T_c of about 39K means the MgB_2 superconductor can be operated under closed-loop refrigeration instead of in a liquid helium bath. The possibility of applications at 20-25 K make MgB_2 cost competitive compared to Nb-based alloys and intermetallic superconductors which have been well studied [5]. Although the $T_{c,s}$ of several cuprate-based high temperature superconductors are in the range of 90K [6,7], their highly anisotropic properties and weak-link problems which require a high degree of grain alignment, as well as cost, limit the industrial applications of these materials. Additionally, MgB_2 is synthesized from relatively inexpensive constituent elements (Mg and B), contains no weak links, and it is relatively easy to fabricate. All these advantages make it a good candidate for future applications.

In spite of the aforementioned advantages, several obstacles limit the actual application of MgB_2 superconductors: (i) low connectivity, due to its porous structure and the presence of impurity phases; (ii) low critical current density, J_c, which is proportionally related to its flux pinning behavior, and (iii) low values of the upper critical field, B_{c2}, compared to those of Nb_3Sn and some cuprate-based superconductors, a deficiency that limits its high magnetic field application. Extensive studies have been devoted to the resolution of these issues [8-11]. Chemical doping has been seen to be an efficient way to enhance the properties of MgB_2 superconductor, especially flux pinning and upper critical

field H_{c2}. After successfully liquefying helium (He) at the boiling point of 4.2 K, which was accomplished in July 1908, Dutch physicist Kamerlingh Onnes measured temperature dependence of resistance of mercury (Hg) and found that at approximately 4.2 K the resistance of Hg dropped suddenly to zero. This suggested that the metal had undergone transition to a new state, which he called the superconductive state [2-3]. From studies on several elements, many other elements have been found to be superconducting with different transition temperatures (T_c) [4-8]. Onnes was awarded Nobel Prize for Physics in 1913. Meissner and Ochsenfeld in November 1933 found that superconductors are normal metals above their critical temperature and allow all magnetic field lines from an external field to penetrate into the samples. After entering into superconducting state, superconductors expel the external magnetic field lines by generating equal and opposite fields on their own, thus exhibiting perfect diamagnetism below its critical temperature. This property is known as Meissner effect and it determines whether a compound is in its normal state or in superconducting state [9]. Meissner and Ochsenfeld also found that there is a limit to the magnetic field value (H_c) below which the superconductivity is sustained. If the magnetic field becomes stronger than H_c, then superconductivity will be destroyed. H_c is temperature dependent. Meisner effect will be discussed more in the next paragraph.

Over the years' superconductivity has been discovered in many metals and metallic compounds with increasing critical temperatures. In most of the applications before 1986 the superconductors used were alloys like NbTi, Nb_3Sn, V_3Sn, and NbN and were used to construct the first superconducting high field magnets. Even though the field and current carrying properties were satisfactory, the fact that the highest critical temperature is around 25 K had limited their applications, since liquid helium was preferred to utilize these superconductors. The alternative coolant liquid hydrogen (boiling point is 20 K), required special safety considerations, the low temperature of the liquid hydrogen causes the atmospheric air to condense on the outside of any installed component that haven been insulated. Through the partial evaporation of nitrogen, the liquid air could become enriched with oxygen and when coming into contact with combustible substances becomes explosive. It is possible to avoid the build-up of an explosive atmosphere in areas surrounding hydrogen installations by building hydrogen storages in well ventilated areas, making certain that hydrogen storages are leak-proof and stay that way, hence the need for cryo-refrigerators, which made their operation complex and hence was not attractive. However, the cost of liquid helium being high made any application costly to maintain or operate.

However, in 1986, Alex Muller and Georg Bednorz [10] discovered a whole new class of superconductors in $La_{2-x}Ba_xCuO_4$, with the highest known critical temperature, at that time, of 35 K, now known as the first member of cuprate superconductors. For this invention they were awarded

Nobel prize for physics in 1987. After this great discovery, the search for high temperature superconductors was amplified. Since 1986, the number of researchers working in the field of superconductivity increased tremendously.

With variations introduced to the crystal structure such as addition of transition-metal impurities, the critical temperature of these materials quickly increased to 90 K and above. Because of this jump in T_c, these superconductors are often referred to as high temperature superconductors (HTSC or HTS). In 1987, a joint group of Wu and Chu had discovered a superconductor of composition $YBa_2Cu_3O_{7-\delta}$ (referred to as YBCO or Y-123) with a transition temperature of 93 K [11]. Subsequently Bi and Tl containing compounds were discovered with transition temperatures of 110 K and 125 K respectively in 1988 [12-13]. The high critical temperature of 135 K transition was achieved for the tallium-based compounds at 150 kbar of applied pressure. This thallium-doped mercuric-cuprate ($HgBa_2Ca_2Cu_3O_8$) discovered was discovered in 1993 [14-15]. The highest transition temperature for superconductors achieved till date belongs to the family of the hydrides, reaching room temperature superconductivity at high pressure of 267 GPa [16]. Many cuprate superconductors have transition temperatures above 77 K, and this unlocks the practical applications which were not economically viable with conventional low temperature superconductors. Since these superconductors can be easily cooled in liquid nitrogen (LN_2, boiling point is 77 K), which is significantly cheaper than liquid helium, the opportunity for research as well as the ability to use them in industries has drastically increased.

1.1. Types of Superconductors:

Based on their response to the applied magnetic properties, superconductors can be divided into two types (Type I and Type II). Type I superconductors are pure metals and they display perfect diamagnetism and zero electrical resistance below their critical temperatures. They expel the external magnetic field completely and are able to levitate over a magnet, but the levitation is unstable because they can move about on the magnetic field lines due to the absence of the mixed state. Type II superconductors are alloys or intermetallic compounds which also display zero electrical resistance below their critical temperatures but are able to trap some external magnetic fields in certain magnetic field range. Type II superconductors can stably levitate over a magnet. They can also suspend underneath the magnets which is because they possess a property known as flux pinning, discussed in further sections.

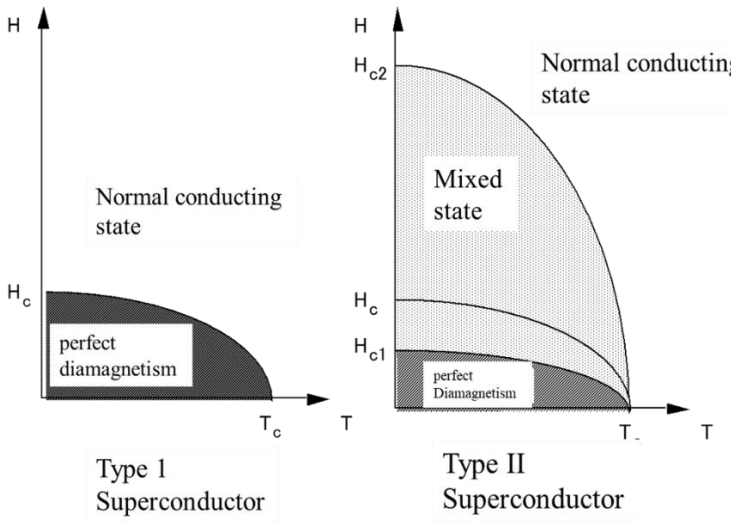

Figure 1.1. Typical H Vs T phase diagram for a Type-I and Type-II superconductors. Note only one critical field exist in Type-I superconductor meanwhile type-II superconductor show existence of two critical fields (H_{c1} and H_{c2}).

Type I superconductors exist in two phases (i) non-superconducting phase which is above their T_c (normal state) and (ii) superconducting phase below T_c where it shows complete Meissner effect. On the other hand, Type II superconductors also have a non-superconducting (normal phase) and a Meissner phase. Along with these two phases they consist of a mixed phase between them. This phase contains regions of normal state within the volume of the Meissner state. These superconductors have two critical magnetic fields, namely the lower critical field ($H_{c1}(T)$) and the upper critical field ($H_{c2}(T)$), which are the limits for the Meissner state and the mixed state respectively. When the external magnetic field is equal to H_{c1}, the magnetic flux abruptly enters the sample. The penetration of the magnetic field increases parabolically until H_{c2} into the superconductor, where it reaches normal state [16-18]. H-T phase diagram of both the superconductors (Type-I and Type-II) is shown in fig. 1.1. In the mixed phase, the magnetic flux enters the superconductor in the form of a series of magnetic flux lines called the flux line lattice. Each flux line (called a vortex) carries a quantized flux, $\Phi_o = h/2e = 2.07 \times 10^{-15}\,\mathrm{Tm}^2$, generated due to the supercurrents circulating around the flux [17, 19]. The center of the vortex is in the normal state, which is non-superconducting, and the vortex is surrounded by the material in superconducting state; hence the name “mixed state”.

1.2 Meissner Effect (perfect diamagnetism)

When a superconductor is cooled below the critical temperature T_c, it expels the magnetic field and does not allow the magnetic field to enter inside it, which is an easier way to explain the concept of perfect diamagnetism. The Meissner effect is the name for this occurrence. The Meissner effect is the expulsion of a magnetic field from a superconductor during its transition to the superconducting

state. The German physicists Walther Meissner and Robert Ochsenfeld discovered this phenomenon in 1933 by measuring the magnetic field distribution outside superconducting tin and lead samples The Meissner effect is shown in figure 1.2.

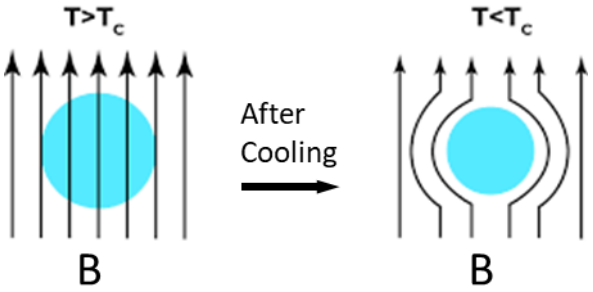

Figure 1.2: Meissner effect

As the applied magnetic field or the average flux density increases, the distance between vortices decreases, and when the applied field reaches the value of H_{c2} of the superconductor then the vortices begin to overlap causing the order parameter to decrease until it vanishes. If the superconductor contains impurities or defect i.e. if it is not a perfect single crystal, magnetic field lines may be pinned or trapped through such defects in the superconductor, this phenomenon is referred to as flux pinning. These vortices (and their normal cores) may be stationary or mobile depending on the specific superconductor.

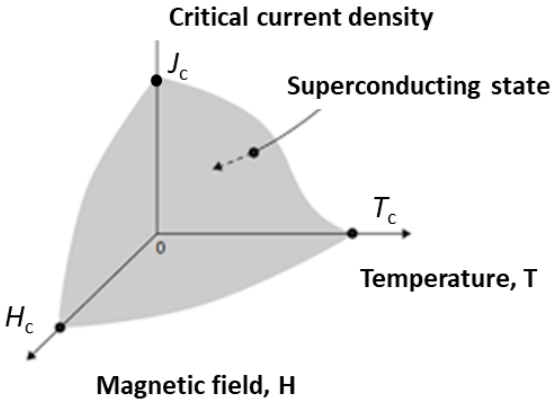

Figure 1.3. Phase diagram of a superconductor.

Further research revealed that the current, applied magnetic field, and temperature define the superconducting limits of a material as a phase diagram for a superconductor as is shown in fig. 1.3. It is these upper limits of T_c, H_c and J_c that material scientists and engineers make attempts to improve in order to realize applications.

The critical temperature is unique to each element or material. The evolution in the T_c of the superconducting materials, over years, from elementary mercury to various High-T_c superconductors, is shown in figure 1.4. Recent discoveries in this field are also included. The critical temperature is unique to each element or material. The evolution in the T_c of the superconducting materials, over years, from elementary mercury to various high T_c superconductors, is shown in figure 1.4. Recent discoveries in this field are also included. However, another important discovery in recent times leading to room-temperature superconductivity is the pressure-driven disproportionation of hydrogen sulfide (H_2S) to H_3S, with a confirmed transition temperature of 203 K at 155 gigapascals. Both H_2S and CH_4 readily mix with hydrogen to form guest–host structures at lower pressures, and are of comparable size at 4 gigapascals. The photochemically synthesized C–S–H system becomes superconducting with its highest critical temperature being $T_c = 287.7 \pm 1.2$ K at 267 ± 10 GPa. The temperature probe's accuracy as reported is ±0.1 K [16].

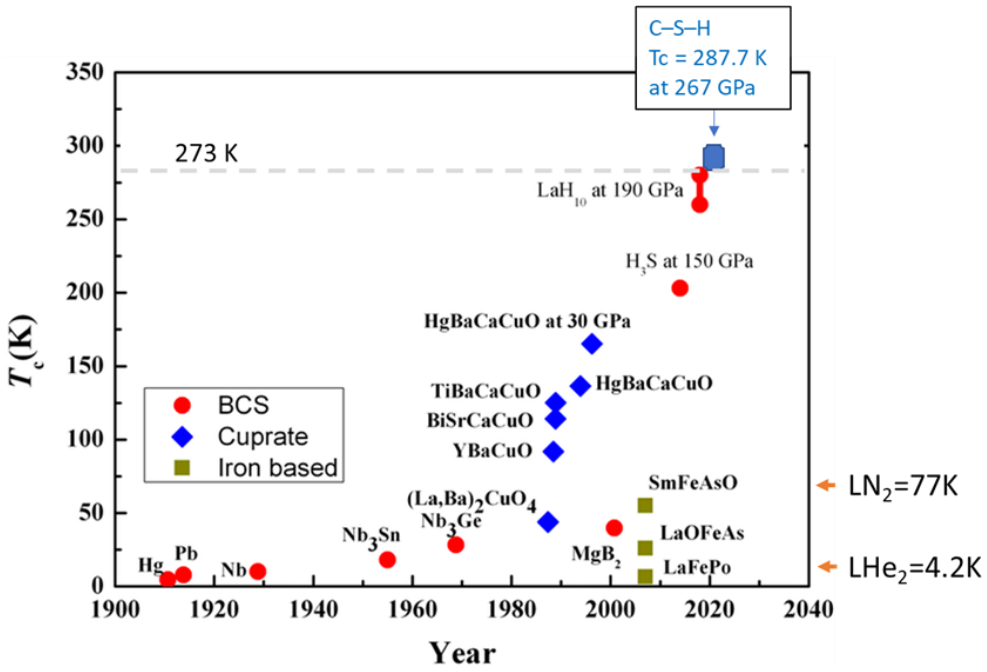

Figure 1.4. Critical temperature discoveries of the various superconducting materials over the years.

The different class of materials and the T_c ranges are given in table 1.1 with the exception of MgB_2 which is described in details in the sub-section that follows.

Table 1.1. T_c range of different types of superconductors, where m=1 and 2 and n=1, 2, 3….

Notation	Stoicheometry	T_c (K)	Class
Hg-BaCa-Cu-O	$Hg_mBa_2Ca_{n-1}Cu_nO2_{n+m+2}$	97-135	Cuprate based
Bi-Sr-Ca-Cu-O	$Bi_mSr_2Ca_{n-1}Cu_nO_{2n+m+2}$	34-110	
RE-Ba-Cu-O	$REBa_2Cu_3O_{7-x}$	89-96	
RE-Fe-As (O,F)	$REFeAsO_{1-x}F_x$	26-55	Iron based
Nb-Sn	Nb_3Sn	18	Metallic
Nb-Ti	NbTi	10	
Nb	Nb	9.2	Elemental
Hg	Hg	4.2	
Ir	Ir	0.11	

Among all the cuprate superconductors, REBCO has drawn more attention because of low flux creep and easy preparation. Even though the T_c's are little less compared to other HTS cuprates, applications can be realized because T_c of REBCO materials are well above 77 K, the boiling point of LN_2. Even though the properties of the LREBCO (where LRE= light rare earth elements such as Nd, Sm, Gd etc.,) materials are better than YBCO, the YBCO superconductors are found to be more interesting because of ease of preparation. YBCO can be prepared in air atmosphere, whereas for preparation of LREBCO materials inert atmosphere need to be provided to reduce the formation of solid solutions that deteriorate superconducting properties.

1.3 The Josephson Effect

The Josephson effect is a phenomenon that occurs when two superconductors are placed in proximity, with some barrier or restriction between them. It can be best describe as a phenomenon in which a superconducting current flows between two weakly coupled superconductors due to the tunnel effect (in quantum mechanics where a wave function propagates beyond a potential barrier) of superconducting electron pairs. In 1962, it was theoretically guided by Brian Josephson, then a graduate student at the University of Cambridge, and experimentally validated by Anderson and Lowell of the Bell Labs. In 1973, Brian Josephson, along with Leo Esaki and others, won the Nobel Prize in Physics for his work on the Josephson effect [20]. It can be said that it is the phenomenon that most clearly shows the characteristics of superconductivity in that the microscopic quantity of the phase of the wave function can be observed macroscopically. There are also important practical examples of quantum mechanical circuits with the Josephson effect, such as the Superconducting Quantum Interference Device (SQUID). The Josephson effect has many

practical applications because it exhibits a precise relationship between different physics quantities, such as voltage and frequency, facilitating highly accurate measurements [21].

The Josephson effect produces a current, known as a supercurrent, that flows continuously without any voltage applied, across a device known as a Josephson junction (JJ). These consist of two or more superconductors coupled by a weak link. The weak link can be a thin insulating barrier (known as a superconductor–insulator–superconductor junction, or S-I-S), a short section of non-superconducting metal (S-N-S), or a physical constriction that weakens the superconductivity at the point of contact (S-c-S)[22]. A simple illustration of the Josephson effect is shown in figure 1.5

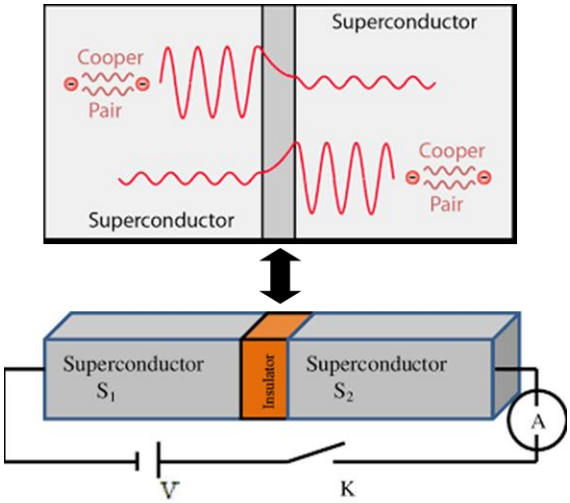

Figure 1.5. Simple illustration of the Josephson effect [22]

1.3 Superconducting materials

It has been established that mercury was the first material to show superconductivity, followed by metals, alloys, intermetallic, amorphous compounds, organic materials, oxides, cuprates, doped fullerenes, chalcogenides, and pnictides, all of which were found to be superconductors at critical temperatures ranging from a few mK to 164 K [23-25]. It's remarkable that noble metals like Cu, Ag, and Au, which are known for being good conductors, never displayed superconductivity at the lowest temperatures possible. At the same time, materials that are good superconductors at low temperatures are good insulators at ambient temperatures. Compounds containing ferromagnetic components like iron are not intended to be superconductive since superconducting materials are recognized for their diamagnetic properties, however there are exceptions. Furthermore, under normal processing circumstances, non-superconducting materials can convert to superconducting by providing sufficient pressure, generating acceptable charge carriers, or by correct irradiation. [26].

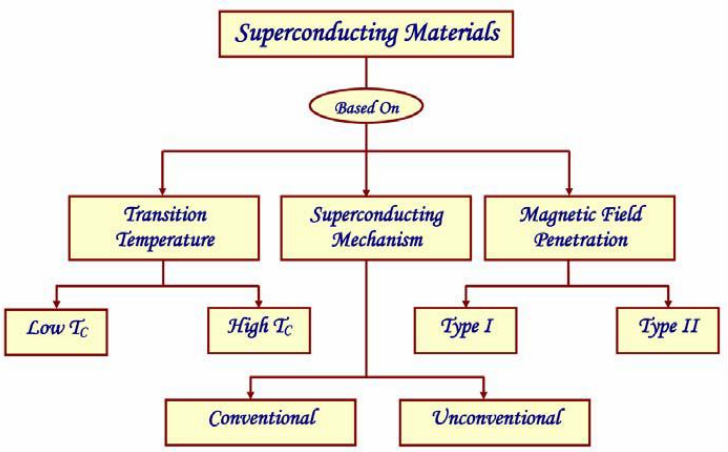

Figure 1.6: Schematic representation of the superconductor classification [84]

Superconducting materials can be classified in a variety of ways, as shown schematically in Figure 1.6. Superconductors are classified primarily by their critical temperature, electromagnetic properties, and underlying process. Superconductors are categorized into two types based on their behavior under an external magnetic field: type I and type II superconductors. Conventional superconductors are those that can be explained by BCS theory or its derivatives, whereas unconventional superconductors are those that cannot be explained by BCS theory. The BCS theory describes how, at low temperatures, a stream of electron pairs flows without resistance in certain materials. According to the idea, this can happen when a single negatively charged electron disrupts the lattice of atoms in the superconductor, attracting a little surplus of positive charge toward it. In turn, this excess attracts a second electron. The electrons are bound together as a Cooper pair by this weak, indirect attraction. Ceramic materials, on the other hand, are projected to be insulators rather than superconductors. However, in 1986, Bednorz and Muller investigated the conductivity of a LaBaCuO ceramic, which produced a superconducting transition at 30 K, signaling the start of a new era in superconductivity [27]. In 1987, Yttrium was used to replace Lanthanum in the LaBaCuO combination, resulting in an astonishing Tc of 92 K [28, 41]. For the first time, a material known as YBCO was discovered that could be superconducting at temperatures higher than liquid nitrogen boiling point. The substitution of Bi for La in LaSrCuO with a stoichiometry $Bi_2Sr_2CuO_6$ (commonly called Bi-2201) with a T_c about 10 K was the first report of superconductivity in the BiSrCaCuO system [42]. Later, Maeda et al. raised the T_c in the Bi-2201 system by adding Ca, resulting in T_c= 80 K for $Bi_2Sr_2CaCu_2O_8$ (Bi-2212) and $Bi_2Sr_2Ca_2Cu_3O_{10}$ (Bi-2223) [33]. Tl-based high T_c superconductors were found by Sheng and Hermann [30]. When Ca was added to the TlBaCuO system, there was a corresponding increase in the T_c. Tl-based systems were classified into two groups [31, 32]. Tl2Ba2CaCuO8 (Tl-2212) has a T_c of 110 K and $Tl_2Ba_2Ca_2Cu_3O_{10}$ (Tl-2223) has a T_c of 125 K [37]. Mercuric cuprates are the current ceramic superconductor system with the greatest critical temperature. In 1993, one of these chemicals was synthesized for the first time. The C–S–H system (T_c= 287.7 K) at 30 GPa pressure has the highest reliable T_c ever recorded [16]. The discovery of high-temperature superconductors sparked a flurry of work, with the goal of developing materials that might display superconductivity at ambient

temperatures, which is now a reality. The promise of chilling using liquid nitrogen, which is less expensive and more practical, sparked anticipation of extensive commercial uses. Further study on these materials revealed that a Mott insulator with antiferromagnetic ordering can produce superconductivity on optimal carrier doping (highly interacting electrons due of their complicated connection with high-temperature superconductors). To unravel the enigma of cuprate superconductors and anticipate future high T_c superconductors, a variety of theoretical approaches to the process have been used.

Nonetheless, arsenic's extreme volatility and toxicity, as well as the need for an inert environment and high processing temperatures, necessitate much more basic study before it can be molded for technological uses. MgB_2 is the most recent possibility for superconducting companies searching for innovation in their goods, despite the fact that there have been numerous breakthroughs in the superconducting sector. Borides had been studied intensively since the 1950s with the goal of increasing T_c. By using neutron scattering spectroscopy, it was predicted that light boron atoms would have a high characteristic frequency, which would increase T_c according to the BCS (Bardeen–Cooper–Schrieffer) formula.

The borocarbide superconductors $RENi_2B_2C$ with Tc up to 16.5 K appeared to partially realize this promise in the 1990s. The finding of superconductivity in MgB_2, a molecule that had been widely known since the 1950s and was already commercially accessible in significant quantities at the time [42], was a great surprise in 2001. In wire/tape geometry, its comparatively high T_c (39 K), J_c (10^5-10^6 A/cm^2 at 4.2 K and in the self-field), and Hc_2 (15-20 T at 4.2 K) values make it a good contender for practical applications. In many aspects, MgB_2 superconducting characteristics differ from those of LTS and HTS. MgB_2 possesses a long coherence length, low anisotropy, and clear grain boundaries, in addition to a reasonably high T_c. MgB_2 has outstanding superconducting qualities without sacrificing its affordability or toughness, and it is one of the best candidates for 20-30 K operation when formed into wires with YBCO. Because ferromagnetism competes with cooper pair production, iron as a ferro-magnet was thought to be the least favorable element for realizing superconductivity. According to the BCS theory, the cooper pairs are the arbitrarily tiny attraction caused by electron-photon interaction, which is responsible for superconductivity. Surprisingly, a group from Tokyo Institute of Technology, Japan, found a novel superconductor based on iron, LaFeOP, in 2006, with a T_c of 4 K regardless of hole/electron doping. The same group discovered a substantial rise in T_c up to 26 K in $LaFeAsO_{0.89}F_{0.11}$ in 2008 [43]. By substituting La with other rare earth ions of lower radius, the T_c of this material was enhanced to 43 K at a pressure of 2 GPa and to 55 K at ambient pressure, a T_c that is second only to the high T_c cuprates [44, 45].

Table 1.2: Superconducting materials under various categories

Material Class	Year	Max. T_c material	$T_{c(max)}$ (K)	ξ (Å)	λ_L (Å)	Category
Elements	1911	Nb	9.5	380	390	Conven.
Alloys and Simple compounds	1912	NbN	17	50	2000	Conven.
A15's	1954	Nb_3Ge	23.2	55	1000	Conv.
Doped semiconductors	1964	CB_x	10	950	720	Conv.
Insul. elements under pressure	1964	S	17			Conv.
Metallic elements under pressure	1968	Ca	25			Conv.
Hydrogen-rich materials	1970	PdD	10.7	400		Conv.
Magnetic superconductors	1972	$ErRh_4B_4$	8.7	180	830	Conv.
Magnesium diboride	2001	MgB_2	39	52	1400	poss. Unc.
Bismuthates	1975	$Ba_{1-x}K_xBiO_3$	34	50	5500	poss. Unc.
Fullerenes	1991	$RbCs_2C_{60}$	33	30	4500	poss. Unc.
Interface superconductivity	2007	$LaAlO_3/SrTiO_3$	.35	600		poss. Unc.
Plutonium compounds	2002	$PuCoGa_5$	18.5	16	2400	poss. Unc.
BiS_2-based materials	2012	$YbO_{0.5}F_{0.5}BiS_2$	5.4	53	5000	poss. Unc.
Cuprates hole-doped	1986	$HgBa_2Ca_2Cu_3O_9$	134	20	1200	Unconv.
Cuprates e-doped	1989	$Sr_{0.9}La_xCuO_2$	40	50	2500	Unconv.
Strontium ruthenate	1994	Sr_2RuO_4	1.5	660	1500	Unconv.
Layered nitrides	1996	Ca(THF)HfNCl	26	60	4700	Unconv.
Ferromagnetic sc	2000		0.8	100	$\sim 10^4$	Unconv.
Cobalt oxyde hydrate	2003	$Na_x(H_3O)_zCoO_2.yH_20$	4.7	100	7000	Unconv.
Non-centro-symmetric	2004	$SrPtSi_3$	2	60	8000	Unconv.
Iron pnictides	2008	$SmFeAsO_{0:85}$	55	10-50	2000	Unconv.
Iron chalcogenides	2008	$Na_xFe_2Se_2$	46	20	2000	Unconv.

Classes of superconducting materials. Con (conventional), Poss.Unc (possibly unconventional) and Uncov (unconventional). The 'Year' indicates which year the first material in the class was discovered. The 'Max T_c' refers to ambient pressure. Typical values of coherence length ξ, penetration depth λ_L and gap ratio are given. In the table.

1.5 History and background of MgB_2

MgB_2 is a binary intermetallic compound that has been studied in the field of material sciences since the early 1950s and is even available commercially. Reports about the development of the MgB_2 phase when Mg and amorphous B were reacting in hydrogen and/or argon atmospheres are made available in reported literatures [48] [49]. Due to the discovery of a novel class of borocarbides called RE-TM2B2C, where RE = Y, Lu, Dy, or other rare earths and TM = Ni or Pd, there has been a lot of interest in intermetallic superconductors that integrate light elements like boron since 1994. Boron atoms have the right size and electrical structure to form direct B-B bonds, which can result in a variety of boron networks. Increased boron concentration results in higher dimensionality of networks. More than 50 boride compounds with various structures have been identified as superconductors [50].

The most notable discovery, however, was the demonstration of superconductivity in B at high pressure and a critical temperature of 11.2 K [51]. Table 1.41 lists all of the AlB_2 type borides, as well as their critical temperatures. Some of these diboride compounds were discovered before and after the discovery of superconductivity in MgB_2. Professor J. Akimitsu (Aoyama-Gakuin University, Tokyo, Japan) announced the discovery of superconductivity in MgB_2 with a T_c of 39 K in January 2001 [52-53]. MgB_2 has the highest critical temperature of any non-cuprate superconductor at the time of its discovery. This discovery sparked a lot of interest in MgB_2 research and development, not only because of its intriguing fundamental features, but also because of its prospective uses.

Table 1.3: List of diborides with their respective critical temperatures [50]

Formula	T_C **(K)**
$\mathbf{MgB_2}$	39
$\mathbf{NbB_2}$	0.62
$\mathbf{NbB_{2.5}}$	6.4
$\mathbf{Nb_{0.76}B_2}$	9.2
$\mathbf{MoB_{2.5}}$	8.1
$\mathbf{BeB_2}$	0.79
$\mathbf{ZrB_2}$	5.5
$\mathbf{TaB_2}$	9.5

1.6 Special features of MgB_2 Superconductor

The following are some of the promising characteristics of MgB_2 that make it more suited than other binary superconductors:

a. Its relatively high T_c
b. Weak link free grain boundaries
c. It has lower anisotropy compare to HTS
d. Coherence length is large ($\xi \sim 5$ nm)
e. It has a remarkably low normal state resistivity ($\rho 42\ K = 0.38\ \mu\Omega cm$)
f. Transport current densities are high (J_c in the range 10^5-10^6 A/cm^2 at 4.2 K)
g. Possession of high upper critical magnetic field, H_{c2} in the temperature range from 4.2 to 30 K
h. It is suitable for low to mid-field applications with temperatures between 20 and 30 K, where a cryo-cooler can be utilized for cooling.
i. Promising for lightweight applications because of its light weight
j. Raw materials are abundant and cheap

Table 1.4: List of superconducting parameters of MgB_2[50]

Parameter	Values
Critical temperature	T_c = 39 K
Hexagonal lattice parameters	a = 0.3084 nm, c = 0.3524 nm
Theoretical density	2.63 g/cm^3
Pressure coefficient	-*1.1*- 2 K/Gpa
Carrier density	1.7 - 2.8 × 10^{23} holes/cm^3
Isotope effect	$\propto T = \propto B + \propto Mg$ = 0.3 + 0.02
Resistivity near T_C	ρ(40K) = 0.4 – 6 μΩcm
Resistivity ratio	ρ(40K)/ρ(300K) = 1 – 27
Upper critical field	$H_{C2}//ab$(0) = 14 - 39 T, $H_{C2}//c$(0) = 2 - 24 T
Lower critical field	H_{C1}(0) = 27 - 48 mT
Coherence lengths	ξab(0) = 3.7 - 12 nm; ξ c(0) = 1.6 - 3.6 nm
Penetration depths	λ(0) = 85 - 180 nm
Energy gap	Δ(0) =1.8 - 7.5 meV

MgB_2 superconducting properties are similar to those of conventional superconductors, not HTS. The isotope effect, a linear T - dependence of the upper critical field with a positive curvature around T_c, and a shift to lower temperatures of both T_c-onset and T_c-offset at rising magnetic fields, as seen in temperature dependent resistivity studies, are among these features. Table 1.4 lists some of the most essential superconducting properties of MgB_2.

1.7 Structural and superconducting properties of MgB_2

1.7.1 Crystal and electronic structure

MgB_2 has a hexagonal AlB_2 crystal structure with a p6/mmm space group, which is typical of diborides [52] [53]. Figure 1.7 depicts the crystal structure. The boron atoms create a graphite-like honeycomb network, with the Mg atoms occupying the hexagons' interstitial places. The B-B bonding is substantially anisotropic because each Mg atom at the center of the hexagon created by B donates its electron to the B planes. The atomic locations in the unit cell for Mg and B Wyckoff positions for atoms are (0, 0, 0) and (1/3, 2/3, 1/2) and (2/3, 1/3, 1/2) respectively [50, 51]. (Mg_8 B_{12}) for Mg and (Mg_6B_3) for B are the coordination polyhedral. The atomic distances are: B-B intralayer = 0.1780 nm, Mg-Mg intralayer = 0.3084 nm, Mg-Mg interlayer = 0.3524 nm, and Mg-B interlayer = 0.25 nm [42, 50]. The lattice parameters are a = 0.3084 nm and c = 0.3524 nm, and the lattice parameters are a = 0.3084 nm and In-plane B-B distance is nearly half of that of interplane B-B distance.

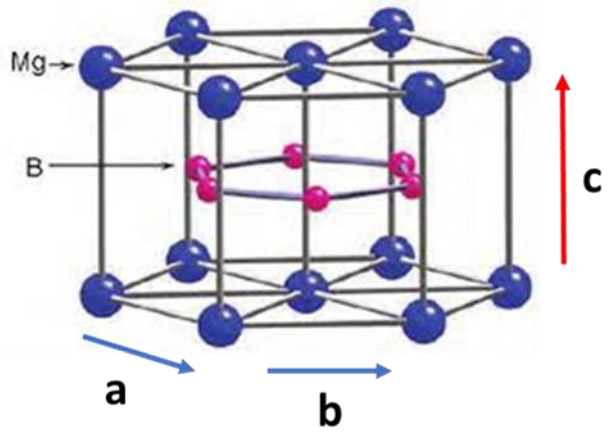

Figure 1.7: Crystal structure of MgB_2 [50]

Despite having a crystal structure that is comparable to that of a graphite intercalated compound, MgB_2 conducting states have a fundamentally different and unusual structure. Since the discovery of superconductivity, various investigations have calculated the band structure [51-55]. Three bands (bonding; in-plane sp_xp_y hybridization) and two bands make up MgB_2 band structure (bonding and antibonding; p_z hybridization). The valence electrons of the Mg atom are donated to the boron planes, producing an ionic interaction with the boron atoms. Strong two-dimensional (2D) covalent connections and three-dimensional (3D) metallic bonding exist between the layers, holding the in-plane boron atoms together. The sp2 hybrids of boron 2s and $p_{x,y}$ orbitals produce 2D covalent σ bands that are partially filled. These hole bands are localized on boron planes, whereas the 3D metallic π type band is delocalized and comes from the boron p_z orbital. As charge carriers, the π band comprises both electrons and holes [55-57].

1.8 Superconducting Mechanism

The formation of electron pairs is the basic mechanism for superconductivity, which is caused by the attraction of electrons via the exchange of atomic vibration excitations (phonons) [58][59]. The pairing of electrons takes place in momentum space rather than physical space. According to the BCS theory of superconductivity, the expression for critical temperature was derived as $T_c = \Theta^{(-1/\Lambda eff)}$, where $\Theta \sim \Theta_D$ represents the Debye temperature of the metal and $\Lambda_{eff} = \Lambda = N_{(EF)} \times V$ represents the coupling constant between the electrons and phonons. $N_{(EF)}$ denotes the electronic level density near the Fermi surface in the normal state and V represents the average matrix element of electron interaction which corresponds to the attraction. The electrons and phonons are believed to have a weak coupling in the original BCS theory, hence the $\Lambda \sim 1$ is expected to be modest [55-57]. According to BCS theory, the value of T_c is limited to $T_c \sim 30$ K. As per BCS theory, larger $N_{(EF)}$, V and Θ_D of a material corresponds to larger T_c values. As for MgB_2, the value of Θ_D is relatively larger when compared to that of other diborides and light materials. This implies that the $N_{(EF)}$ is relatively

low as there are no d electrons present. Researchers were compelled to investigate the underlying superconducting mechanism after discovering an extremely high T_c in MgB_2 when compared to typical LTS. The superconducting mechanism in MgB_2 has been studied extensively both theoretically and experimentally. MgB_2 superconductivity differs from that of other metallic superconductors in a number of ways. In its superconducting state, MgB_2 is the first superconductor to demonstrate two separate superconducting gaps [61]. Many people thought the material had an unusual exotic superconducting mechanism at first [58, 62]. Because holes are the major charge carriers in the normal state, some researchers speculated that MgB2 could have hole superconductivity similar to HTS [57]. MgB_2 is a phonon-mediated BCS type superconductor, according to the majority of theorists, with selective coupling between certain electronic states and specific phonons, which is the key factor for superconductivity. The considerable anharmonicity of the phonons involved was blamed for the very high T_c. MgB_2 T_c is influenced by $N_{(EF)}$, the average energy of the participating phonons, and the strength of the coupling between the charge carriers and the phonons because it is a BCS superconductor. The material's Tc drops as $N_{(EF)}$ lowers. MgB_2 seems to be the first system for which multiband superconductivity has been observed using polycrystalline samples or single crystals, according to numerous experimental methodologies. The existence of two superconducting energy gaps in this material is due to high electron coupling in the 2D bands and poor coupling in the 3D bands. Impurity scattering, in addition to being a two-band superconductor, should have a pair breaking effect, lowering the T_c [58]. Charge scattering results in a reduction in coherence length and an increase in H_{c2} values. Over the years, this rule has been applied to the design and manufacture of LTS materials. The intra-band scattering inside the and bands, as well as the inter-band scattering between the σ and π bands, all have different scattering rates in MgB_2. High H_{c2} values in MgB_2, well beyond the reach of NbTi and Nb_3Sn, can be achieved by tuning these inter and intra band scattering rates. H_{c2} values of 40-50 T have been observed for several MgB_2 polycrystals, with the maximum H_{c2} of ~74 T reported for a thin film [61].

On the other hand, some reports indicated unconventional superconductivity similar to cuprates, like quadratic *T*-dependence of the penetration depth and reversal of the hall coefficient near T_c. Moreover, the value of isotopic coefficient of MgB_2 (0.32) is much lower than the expected value (0.5) for BCS superconductor [58, 62]. Nevertheless, majority of the reports support the BCS mechanism, i.e., an electron-phonon driven *s* wave mechanism of superconductivity in MgB_2.

1.9 Flux Pinning in MgB_2

In the presence of a magnetic field, flux pinning is essential to the existence of the superconducting current in a Type II superconductor. As mentioned in Section 1.2, a Type-II

superconductor exposed to a magnetic field between B_{c1} and B_{c2} forms a mixed state with a hexagonal flux-line lattice. When transport current flows through a Type-II superconductor in the mixed state, an electromagnetic interaction – specifically the Lorentz force - between the current and the flux-line lattice (FLL) is generated, Figure 1.8. This force, however, would cause the flux-lines to move if there was no restraint. This movement causes a voltage drop in the opposite direction of the transport current, resulting in macroscopic resistive behavior. The flux-line lattice will not move, no resistive behavior will appear, and the material will stay superconducting if the Lorentz force is balanced by an opposing force. The following assumptions underpin flux pinning theory: the flux-line lattice is "pinned" by "pinning centers" that generate a flux pinning force that counteracts the Lorentz force, allowing the material to remain superconducting. The bulk pinning force density F_p is commonly defined by the pinning strength per volume and represents the averaged sum of all elemental pinning forces, resulting in $F_p = J_c \times B$. It suggests that the superconductor can carry a greater transport current if the pinning strength is raised [63].

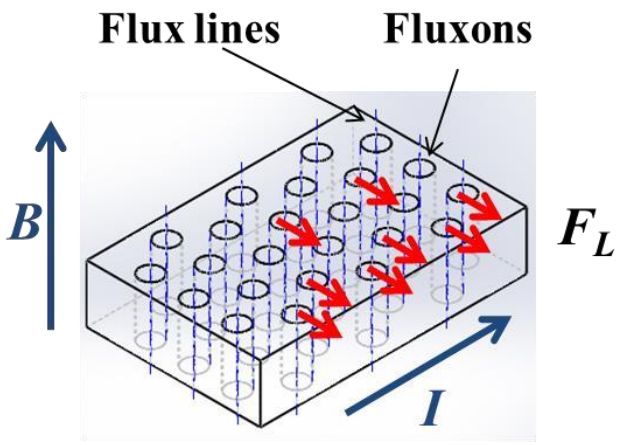

Figure 1.8 Schematic diagram of the relationship between the transport current, I, the applied field, B, and the Lorentz force, F_L, on the flux lines.

Consider the case where normal state spherical defects with an average diameter x (assume a simple case, $x > 2\xi$ where ξ is the coherence length) work as pinning centers in a mixed state type-II superconductor in an external field B. The increase of volumetric free energy in the defects, due to the present magnetic field, is $B_{c2}/2\mu_0$ with respect to the superconducting matrix which has no magnetic field inside. Also, as mentioned in Section 1.2, since the type-II superconductor is in a mixed state, the normal cores and superconducting matrix co-exist. There is also a magnetic field B inside these normal cores.

The scaling of the pinning force proposed by Kramer [64] and Dew–Hughes (DH) [65] is a useful tool for studying the pinning processes that a specific superconductor sample possesses. This method is applicable to High-T_c analogues [65–69], MgB_2 [69–83], and iron-based superconductors [82], in addition to typical metallic superconductors, where the pioneering work was done. The changes are visible when the irreversibility field, H_{irr}, is used for scaling instead of the upper critical field, H_{c2}, since H_{irr} determines the upper limit of flux pinning (= irreversible region in the H-T diagram). Several authors [66-67] have demonstrated that MgB_2 polycrystalline samples primarily follow the grain boundary pinning mechanism, which falls under the normal surface pinning category; however, other evidence suggests that the normal point pinning and normal volume pinning mechanisms may also be at work under certain conditions [70-71]. Figure 1.9 shows demonstrations of the usual flux pinning techniques. The scaling of the flux pinning data given by: $f_p = F_p/F_{p,max}$ vs. $h = H_a/H_{irr}$ by a fit to the functional dependence given by the following:

$$f_p = A \cdot (h)^p \cdot (1-h)^q \qquad \text{..... (1)}$$

The resulting parameters, p and q, determine the dimensionality and the type of the dominating flux pinning, whereas the numerical parameter A in (1) is obtained from the normalization condition $F_p/F_{p,max} = 1$.This describes the major bulk flux pinning force formulas according to the Dew-Hughes model in MgB_2.

The peak positions corresponding to different mechanisms, h_0, can be estimated as $h_0 = p/(p+q)$. Six pinning functions $f(h)$ were explained in the DH model which give details about the core pinning using (1): (1) p = 0, q = 2: normal, volume pinning; (2) p = 1, q = 1: Δκ-pinning, volume pins; (3) p = 1/2, q = 2: normal, surface pins; (4) p = 3/2, q = 1: Δκ-pinning, surface pins; (5) p = 1, q = 2: normal, point pins; and (6) p = 2, q = 1: Δκ-pinning, point pins. Kramer [64] predicts the function (3) for shear-breaking in the case of a set of flat pins. In addition, in this situation, a seventh function defining the magnetic interaction can be ignored.

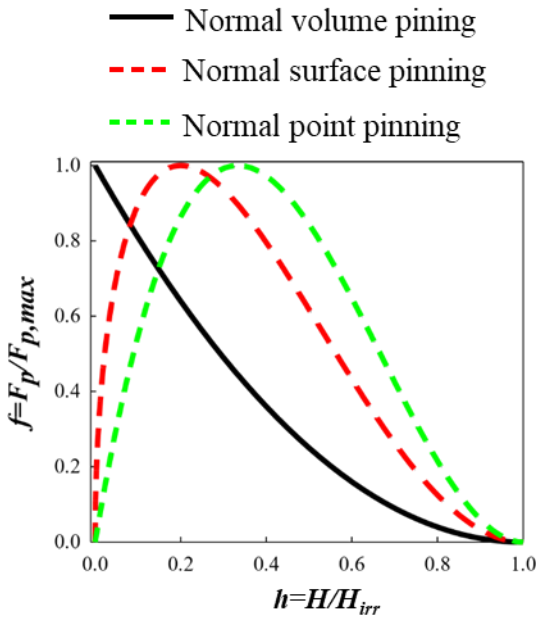

Figure 1.9 Three normalized bulk pinning function curves, Dew-Hughes [68].

As a result, the parameter p, which specifies the dimensionality of the pins, can take the values 0, 0.5, 1, 1.5, and 2, while the parameter q, which describes the kind of pinning, can only take the values 1 and 2. (i.e., normal conducting or superconducting). With this in mind, we can readily conclude that analyzing the pinning force scaling offers critical information about the flux pinning qualities of a particular sample, if the F_p measurements are properly scaled. In order to learn more about flux pinning in MgB_2 samples, we analyzed a variety of MgB_2 samples made using diverse procedures in this study. The sintered, polycrystalline MgB_2 samples used in this investigation were sintered at temperatures ranging from 775 to 1000 degrees Celsius (ºC). Some samples have well-developed scaling, whereas others do not. Within the scope of the DH pinning model, the acquired results are explained.

1.10 Statement of the Problem

The methods and techniques developed by researchers to improve the superconducting performance of the MgB_2 bulk material are numerous ranging from elemental doping, control of sintering regimes to enhance the microstructures, grain size control and connectivity etc. However, another major issue to ponder about is that of improving the bulk density and aspect ratio for the sake of practical applications as to tend towards industrial practices. In this thesis, several approaches were employed to have synthesized bulk MgB_2 via conventional solid state sintering and both in-situ and ex-situ routes by employing fabrication techniques such as hot isostatic pressure (HIP) methods, hot pressing (HP), and the so-called spark plasma sintering methods. However, the challenge has still been that of obtaining maximum density without compromising the structural and phase orientation

of the bulk. Decomposition of the phases is a lingering issue in ex-situ processing which also contributes to the degrading of the superconducting performance. In-situ processing like any other conventional technique is associated with MgO formation as impurity phase in the MgB_2 bulk sample structure. Careful control of these secondary phases was also studied. With respect to practical applications in the field of pulse field magnetization (PFM), poor heat dissipation due to the anisotropic nature of the bulk MgB_2 resorts to flux jumps during PFM measurements which results to a corresponding degradation of the trapped fields. There is a potential to suppress the occurrence of flux jumps and possibly measure high trapped fields in bulk MgB_2 superconductors.

1.8 Applications

Several superconductors have been discovered with only few of them hitting the application spectrum in reality. Magnesium diboride (MgB_2) having some promising features made it stand out among other conventional intermetallic and/or binary superconductors. Its critical temperature of 39 K places it among the intermediate temperature superconductors, sandwiched between low-temperature superconductors like niobium titanium (NbTi) and niobium tin (Nb_3Sn) and high-temperature superconductors like cuprates. A great advantage since its discovery has aroused great interest because it is cheap to make, simple to cool, easy to shape into wires, magnesium diboride could throw the field of superconducting applications wide open implying it could replace the niobium-titanium, a conventional low-temperature superconductor, in future MRI magnets. Also, MgB_2 magnet might function at a temperature of the order of 10 K in a magnetic field range of up to 4 T, based on its current superconducting capabilities. It will then be feasible to create cryogenics that do not require helium and rely only on cryocoolers as a cold supply. However, researchers have developed many techniques through R&D programs for generating design and technological tools for producing such magnets as a result of this promising features. For applications such as transformers for electric utility grids, magnesium diboride seems a good choice. In fact, they may be the entry application that the material needs to gain a foothold in the marketplace which leads to the estimation that magnesium diboride transformers will be more economically attractive not only than those based on high-temperature superconductors but even than those using copper wire. The wires may also be used to improve the performance of electric motors and generators, because superconducting coils can carry much more current than copper. Thin superconducting films could serve as electronic components and sensitive magnetic sensors. Other potential roles would be in superconducting magnets and wireless base stations. Superconducting magnetic energy storage (SMES) is more fast response, economical, and environment-friendly than uninterruptible power supply (UPS) using the battery. The SMES not only has the capacity to manage active and reactive power at the same time,

but it also has a long life span due to the superconducting magnet's lack of deterioration, which is a concern with batteries. As a result, the SMES might be used instead of the UPS's battery. Without exception, the SMES requires a cryogenic system. [84] [85]

1.12 Motivation and Objectives

Magnetization measurements of early pressed MgB_2 bulk samples suggested that high J_c was already present despite the several approaches discussed in our earlier introductions. MgB_2 have been introduced to include the problems and prospects of this unique bulk material. This work helps to understand that there is still work to be done to further promote the underlying advantages and provide more advance and ideal ways of material processing in order to further improve the performance of the superconducting bulk material. Higher J_c values have been recorded in other approaches, such as thin films, where some findings reach 10^6 to 10^7 A/cm^2 order in low field at 4.2 K, implying that bulk MgB_2 performance may still be improved significantly. Other processes, such as pulsed laser deposition, create very fine grains as small as 10 nm in size, according to electron microscopy and other investigations. Even while this work aims to stress this method for the bulks, the high number density of grain boundaries is compatible with such high J_c values, which were predicted to grow inversely with grain size [73] [75]. In this thesis, we retain some of our conventional techniques of synthesis and also focus more on the novel techniques that will further improve these significant features, most especially that of the additional pinning centers, suppressing voids in the bulks, grain refinement and connectivity which are key to improving the flux pinning performance and hence the superconducting J_c of bulk MgB_2 [65-74]. A part of this work is to further achieve these properties via improving the density of the bulk by employing the novel spark plasma sintering technique which is sequel to improving the grain size and connectivity and simultaneously contributing to improving the mechanical properties of the bulk. Another part of this work focuses on the applications of the bulk MgB_2 in magnetic applications such as the pulse field magnetization (PFM). However, the problem of heat generation during trapped field measurements without significant dissipation of the heat from the bulk causes the occurrence of flux jumps with degrades the value of the trapped fields most especially at high applied fields [75-77]. Our target is to successfully measure trapped fields without flux jumps which will be a significant breakthrough for high magnetic field applications.

The main objectives of this thesis is are summarized below:

a. To improve the superconducting performance of the bulk MgB_2 via elemental doping and introduction of new pinning centers.
b. To enhance both self-field and infield J_c to be achieved by temperature optimization via spark plasma sintering technique with resulting improved density and grain size refinement.

c. To realize a narrow processing window which could be achieved for well sintered MgB_2 bulk by SPS by virtue of simultaneous optimization of both temperature and dwell time.
d. To solve flux jumps problems at high applied fields during PFM process on MgB_2 bulk by improvement of the heat dissipation that could overcome the anisotropic thermal property of MgB_2 bulk superconductor.

1.13 Organization of the thesis:

This thesis is organized into five (5) chapters. The contents of the chapters are as follows;

Chapter I provides a brief introduction to high temperature, history and background of superconductors in general and reviews the literature on synthesis and properties of MgB_2 bulk superconductors. Structural and characteristics, superconducting and flux pinning characteristics which enhances the critical current densities are discussed. The current status of the research and the challenges yet to be resolved are narrated. This chapter also defines the objectives of the present work.

Chapter II discusses the experimental techniques used in the present work. Preparation of MgB_2 superconductors into which several techniques involved in the fabrication process are discussed. The samples are characterized with regard to their characteristic structures, microstructures, and composition of various phases present in their compositional matrix and the influence on their magnetic properties. Microstructures of metallographically polished samples are studied under a Field Emission Scanning Electron Microscopy (FE-SEM, JEOL make, JSM-7100 model) and compositional analysis was done through Energy Dispersive Spectroscopy attachment. The X-ray diffraction (XRD) study includes phase identification and lattice parameter calculation. In the present study XRD patterns of samples were taken using Rigaku/Smart Lab, using Cu Kα radiation with wavelength of 1.5405 Å. Further microstructural and elemental characterizations were carried out by transmission emission microscope (TEM Titan Themis G2 80-200 kV X-FEG). Field and temperature dependent characterizations were carried out. Magnetization hysteresis (*M-H*) loops were measured in field range from 0 to 5 T at 20 K and temperature dependence magnetization curves were recorded using a superconducting quantum interference device (SQUID) magnetometer (MPMS V model, Quantum Design)

The next part of the thesis is **Chapter III** which discusses the initial study to improve the superconducting performance of the critical current density and the flux pinning of polycrystalline bulk MgB_2 superconductor by chemical doping. The effect of the different additives on the structural and superconducting properties are also summarized in this chapter. The different techniques employed in this chapter showed the developmental stages of the work which gave the insight into

further studies on the advance techniques to further improve the quality and performance in terms of bulk strength and enhanced connectivity which contributed greatly to the superconducting performance of the MgB_2 bulk superconductor later discussed in chapter IV.

Chapter IV discusses high density MgB_2 bulk superconductors synthesized by spark plasma sintering (SPS) under pressure to improve the field dependence of critical current density (J_c-B) in MgB_2 bulk superconductors. Investigation was done on the relationship between sintering conditions (in this case, temperature and time) and J_c-B using two methods, *ex-situ* (sintering MgB_2 synthesized powder) and *in-situ* (reaction sintering of Mg and B powder), respectively. The *in-situ* method showed very minimal impurity with corresponding improvement in density and J_c-B characteristics for sample *in-situ* optimized sample. Microstructural characterization and flux pinning (f_P) analysis revealed the possibility of refined MgO inclusions and MgB_4 phase as new pinning centers which greatly contributed to the J_c-B properties in ex-situ SPS processing. The contributions of the sintering conditions on f_P for both synthesis methods were analyzed and discussed.

In **Chapter V**. It discussed the practical applications of bulk MgB_2 superconductor by subjecting the bulk sample to pulse field magnetization (PFM). This chapter also investigated how to solve the degrading of trapped fields B_T in bulk MgB_2 superconductor due to the occurrences of flux jumps. This work presents the method for characterizing the propagation of the magnetic flux in an artificially drilled MgB_2 bulk superconductor fabricated via SPS. The PFM was utilized by studying the effect of applied fields B_A on the bulk MgB_2 embedded with low melting alloy of Bi-In-Sn alloy and aluminum rods within the holes which improved the thermal property, suppressing the flux jumps caused by the generated heat within the bulk sample. The magnetic flux dissipation, the flux motion, and performance by evaluation of the capture field ratio B_T/B_P were analyzed and discussed with reference to the field trapping performance of the improvised bulk at high applied fields. This chapter explained how to solve the flux jump problem in the bulk superconductor resulting from poor heat dissipation. The available data shows that it is an experimental breakthrough that supports existing simulation studies and reports giving which gives way for more prospects for high field applications in the development of bulk MgB_2 superconductors.

Chapter VI is the summary and conclusion of the findings and breakthrough in this dissertation. This section also suggested possible advanced approaches for future developments and future prospects that resulted from this thesis.

References:

[1] C. P Canfield and G. W. Crabtree "Magnesium diboride: better late than never", Physics Today Ame. Inst. of Phys. (2003) 34-40

[2] H. Kamerlingh Onnes, research notebooks 56-57, Kamerlingh Onnes Archive, Boerhaave Museum, Leiden, the Netherlands, H Kamerlingh Onnes, Leiden Comm. 120b 122b, 124c, (1911).

[3] R. O. De Bruyn "Heike Kamerlingh Onnes's Discovery of Superconductivity" Scientific American, 276 **3** (1997), 98 – 103.

[4] M. E. Jones and R. E. Marsh, "The preparation and structure of magnesium diboride MgB_2" J. Amer. Chem. Soc. **76** (1954), 1434.

[5] W. Buckel, R. Kleiner, "Superconductivity - Fundamentals and Applications", WILEY-VCH Verlag, Weinheim (2004).

[6] T. H. Geballe, "The Never-Ending Search for High-Temperature Superconductivity" **19** (2006) 261–276

[7] E.A. Ekimov, V.A. Sidorov, E.D. Bauer, N.N. Mel'nik, N.J. Curro, J.D. Thompson and S.M. Stishov, "Superconductivity in diamond" Nature **428** 542, (2004)

[8] C. Buzea and T. Yamashita, "Review of the superconducting properties of MgB_2" Supercond. Sci. Techn. **14** (2001) R115.

[9] W. Meissner and R. Ochsenfeld, "A new effect when superconductivity occurs", Natural Science **21** (1933) 787.

[10] J. Bednorz and K.A. Muller, Z. "Possible high-T_c superconductivity in Ba-La-Cu-O system" Phys. B: Cond. Matter. **64** (1986) 189.

[11] M.K. Wu, J.R. Ashburn, C.J. Torng, P.H. Hor, R.L. Meng, L. Gao, Z.J. Huang, Y.Q. Wang and C. W. Chu, "Superconductivity at 93 K in a new mixed-phase Y-Ba-Cu-O compound system at ambient pressure" Phys Rev Lett **58** (1987) 908–910.

[12] H. Maeda, Y. Tanaka, M. Fukutomi and T. Asano, "A new High-T_c Oxide Superconductor without a Rare Earth Element" Jpn J Appl Phys **27** (1988) 209–210.

[13] Z.Z. Sheng and A.M. Hermann, "Superconductivity in the rare-earth-free Tl–Ba–Cu–O system above liquid-nitrogen temperature" Nature **332** (1988) 55–58.

[14] C.W. Chu, L. Gao, F. Chen, Z.J. Huang, R.L. Meng & Y.Y. Xue, "Superconductivity above 150 K in $HgBa_2Ca_2Cu_3O_{8+\delta}$ at high pressures" Nature **365** (1993) 323 – 325.

[15] M. Andrei, “Room-temperature superconductivity”. (Cambridge, UK: Cambridge International Science Pub., (2004) 5–7.

[16] E. Snider, N. Dasenbrock-Gammon, R. McBride, M. Debessai, H. Vindana, K. Vencatasamy, K. V. Lawler, Ashkan Salamat, Ranga P. Dias “Room-temperature superconductivity in a carbonaceous sulfur hydride” Nature **586** (2020) 373

[17] J.B. Ketterson and S.N. Song, “Superconductivity” Cambridge: Cambridge University Press, (1999)

[18] S. P. Thomas, Introduction to high-temperature superconductivity. (New York: Kluwer Academic, 2002.) p. 21–22. To Review on Superconducting Materials, Roland Hott, Reinhold Kleiner, Thomas Wolf & Gertrud Zwicknagl, to be published in “Handbook of Applied Superconductivity”, Wiley-VCH.

[19] E. H Brandt, “Vortices in superconductors” Physica C **369** (2002) 10-20.

[20] C. Buzea and T. Yamashita,” MgB_2-A Review of Superconducting and Normal Properties” Supercond. Sci. Technol. **14** (2001) R115–R146

[21] B. D. Josephson (1962). "Possible new effects in superconductive tunnelling". *Phys. Lett*. **1** (7): 251–253

[22] F. Tafuri, “Fundamentals and Frontiers of the Josephson Effect” (Springer Series in Materials Science Book 286) (English Edition) 1st ed. 2019 Edition, Kindle Edition

[23] B. Werner, and R. Kleiner. “Superconductivity: fundamentals and applications”. 2nd rev. and enl. ed. (Weinheim: Wiley-VCH 2004) 351–443.

[24] H. Hosono, K. Tanabe, E. Takayama-Muromachi, H. Kageyama, S. Yamanaka, H. Kumakura, M. Nohara, H. Hiramatsu and S. Fujitsu “Exploration of new superconductors and functional materials, and fabrication of superconducting tapes and wires of iron pnictides” Supercond. Sci. Technol. Adv. Mater. **16** (2015) 033503 87

[25] D.M. Smyth, PP.1-10 in ceramic superconductors II. Research Update 1988, M.F.Yan, Ed. The American Ceramic Society, (1988).

[26] A. Baranauskas, D. Jasaitis, A. Kareiva, R. Haberkorn and H.P. Beck, “Sol–gel preparation and characterization of manganese-substituted superconducting $YBa_2(Cu_{1-x}Mn_x)_4O_8$ compounds” J. Euro. Ceram. Soc. **21** (2001) 399.

[27] S. Gholipour, V. Daadmehr, A.T. Rezakhani, H. Khosroabadi, F. Shahbaz Tehrani and R. Hosseini Akbarnejad, “Structural Phase of Y-358 Superconductor Comparison with Y-123” J. Supercond. Nov. Magn. **25** (2012) 2253–2258.

[28] A. Aliabadi, Y. Akhavan-Farshchi and M. Akhavan, “Flux Dynamics in Y358 and Gd358 Superconductors” Physica C **27** (2014) 3.

[29] M. Murakami, “Processing of bulk YBaCuO” Supercond. Sci. Technol. **5** (1992) 185–203.

[30] D.C. Larbalestier, S.E. Babcock, X. Cai, M. Daeumling, D.P. Hampshire, T.F. Kelly, L.A. Lavanier, P.J. Lee and J. Seuntjens, “Weak links and the poor transport critical currents of the 123 compounds” Physica C **1580** (1988) 153-155

[31] F. Stucki, P. Brüesch, T. Baumann, “Grain boundary and impurity phase in YBCO” Physica C **200** (1988) 153-155

[32] S. Jin, T.H. Tiefel, R.C. Sherwood, R.B. van Dover, M.E. Davis, G.W. Kammlott and R.A. Fastnacht, “Melt-textured growth of polycrystalline YBa/sub 2/Cu/sub 3/O/sub 7/. sqrt. /sub delta/ with high transport J/sub c/ at 77 K” Phys. Rev. B **37** (1988) 13.

[33] M. Murakami, M. Morita, K. Doi, K. Mivamoto and H.L. Hamada, “Present status of bulk high temperature superconductors” Japan. J. Appl. Phys. **28** (1989) L399.

[34] K. Salama and S. Sathyamurthy, “Texturing of High-T_c superconductors” Supercond. Sci.Technol. **11** (1988) 954.

[35] M. K. Mironova, G. Du, I. A. Rusakocva and K. Salama, “Superconductivity and its applications” Physica C **271** (1996) 15.

[36] L. Zhou, P. Zhang, P. Ji, K. Wang, J. Wang and X. Wu, Supercond. Sci. Technol. **34** (1990) 90.

[37] D. Shi, S. Sengupta, J.S. Lou, C. Varanasi and P.J. Mc Ginn, “Extremely fine precipitates and flux pinning in melt-processed $YBa_2Cu_3O_x$” Physica C **213** (1993) 179.

[38] S. Hu, H. Hojiaji, A. Barkatt, M. Boroomand, M. Hung, A.C. Buechele, A.N. Thorpe and D. Davis, HTS Material, Bulk Processing and Bulk Applications ed C W Chuet al (Singapore: World Scientific) (1992) 313.

[39] G. Krabbes, G. Fuchs, W-R Canders, H May, and R. Palka, “High Temperature Superconductor Bulk Materials” WILEY-VCH Verlag GmbH & Co. KGaA, Weinheim (2006) ISBN: 3-527-40383-3

[40] M. Murakami, S. Gotoh, H. Fujinoto, K. Yamaguchi, N. Koshizuka and S. Tanaka, Flux pinning and critical currents in melt processed YBaCuO superconductors’ Supercond. Sci. Technol. **4** (1991) S49.

[41] M. Muralidhar, N. Sakai, M. Jirsa, M. Murakami and I. Hirabayashi, “Record flux pinning in melt-textured NEG-123 doped by Mo and Nb nanoparticle” App. Phys. Lett. **92** (2008) 162512.

[42] Y.L. Chen, H.M. Chan, M.P. Harmer, V.R. Todt, S. Sengupta and D. Shi “A new method for net-shape forming of large, single-domain $YBa_2Cu_3O_{6+x}$” Physica C **234** (1994) 232–6.

[43] E.S. Reddy and T. Rajasekharan, “Shape Forming Simultaneous with J_c Enhancement in $REBa_2Cu_3O_7$ Superconductors” J. Mater. Res. **130** (1998) 2472

[44] Hampshire and Jones, “Flux flow in high-temperature type II superconductors governed by the activation of Frank-Read sources and the resultant motion of core dislocations” J. Phys. C **21**, (1987) 419

[45] V.V. Flambaum, G.A. Stewart, G.J. Russell, J. Horvat, S.X. Dou “The effect of hydrogenation on the superconducting transition temperature of MgB_2” Physica C **382** (2002) 213–216.

[46] J.E. Hirsch, M. Brian Maple, F. Marsiglio, Superconducting Materials Classes: Introduction and Overview, Physica C **514** (2015) 1-8.

[47] A N. Kolmogorov, M. Calandra, and S. Curtarolo “Thermodynamic stabilities of ternary metal borides: An *ab initio* guide for synthesizing layered superconductors” Phys. Rev. B **78,** (2008) 094520

[48] D.C Johnston, “Superconductivity in a new ternary structure class of boride compounds” solid state comm. Vol 24, **10** (1977) 699-702.

[49] T. Yildirim, “The surprising Superconductor” Materials Today **5** (2002) 40-44

[50] J. Nagamatsu, N. Nakagawa, T. Muranaka, Y. Zenitani. J. Akimitsu, “Superconductivity at 39 K in magnesium diboride”. Nature **63** (2001) *410*

[51] T. Matsushita, “Flux Pinning in Superconductors,” Springer-Verlag Berlin Heidelberg, (2007) 38

[52] L. Zhou, S.K. Chen, K.G. Wang, X.Z. Wu, P.X. Zhang and Y. Feng, “Synthesis of ultrafine Y_2BaCuO_5 powder and its incorporation into YBCO bulk by powder melting process” Physica C **363** (2001) 99−106.

[53] L. Ivanovskii, “Band structure and properties of superconducting MgB_2 and related compounds (A review)” Physics of the Solid State **45** (2003) 1829–1859

[54] H.J. Choi, D. Roundy, H. Sun, M.L. Cohen, S.G. Louie, “The origin of the anomalous superconducting properties of MgB_2” Nature, **418** (2002) 758

[55] J. Nagamatsu, N. Nakagawa, T. Muranaka, Y. Zenitani, J. Akimitsu “Superconductivity at 39 K in magnesium diboride” Nature **410** (2001) 63

[56] S. V. Vonsovskii, Yu. A. Izyumov, and É. Z. Kurmaev, Superconductivity of Transition Metals, Their Alloys, and Compounds (Nauka, Moscow, 1977).

[57] F. Bouquet, Y. Wang, R.A. Fisher, D.G. Hinks, J.D. Jorgensen, A. Junod, N.E. Phillips, EuroPhys. Lett., **56** (2001) 856

[58] A. Carrington, P.J. Meeson, J.R. Cooper, N.E Hussey, P.J. Meeson, S. Lee, A. Yamamoto, S. Tajima, “Determination of the Fermi Surface of MgB_2 by the de Haas–van Alphen Effect” Phys. Rev. Lett., **91** (2003), 3-18

[59] N. B. Brandt, S. M. Chudinov, and Ya. G. Ponomarev, "Modern Problems in Condensed Matter Physics" (North-Holland, Amsterdam, 1988).

[60] H. Padamsee, J.E. Neighbor, C.A. Shiffman, "Quasiparticle phenomenology for thermodynamics of strong-coupling superconductors" J. Low Temp. Phys., **12** (1973) 1175

[61] K. D. Belashchenko, M. van Schilfgaarde, and V. P. Antropov "Coexistence of covalent and metallic bonding in the boron intercalation superconductor MgB_2" Phy. Rev B **64** (2001) 092503

[62] Superconductivity in Ternary Compounds, Vol. 1: Structural, Electronic, and Lattice Properties, Vol. 2: Superconductivity and Magnetism, Ed. by M. B. Maple and O. Fischer (Springer-Verlag, Berlin, 1982).

[63] R. J. Cava, H. Takagi, B. Batlogg, H.W. Zandbergen, R. B. van Dover, J.J. Krajewski, S. Uchida., "Superconductivity in the quaternary intermetallic compounds $LnNi_2B_2C$" Nature **367** (1994) 146.

[64] E. J. Kramer: "Scaling laws for flux pinning in hard superconductors". J. Appl. Phys. **44** (1973) 1360–1370

[65] D. Dew-Hughes: Flux pinning mechanisms in type-II superconductors. Philos. Mag. **30** (1974) 293–305

[66] M.R Koblischka, V. Dalen, A.J.J., Higuchi, T., Yoo, S.I., Murakami, M.: Analysis of pinning in NdBa2Cu3O7−δ superconductors. Phys. Rev. B **58** (1998) 2863

[67] M. R. Koblischka: Pinning forces and scaling in high-T_c superconductors. Phys. C **282** (1997) 2193–2194

[68] M.R. Koblischka: Pinning in bulk high- T_c superconductors. Inst. Phys. Conf. Ser. **58** (1997) 1141–1144

[69] M. Schneider, D. Lipp, A. Gladun, P. Zahn, A. Handstein, G. Fuchs, S-L Drechsler, M. Richter, K-H Muller, H. Rosner "Heat and charge transport properties of MgB_2" Physica C **363** (2001), 6–12

[70] V. Sandu, C.h.J Chee.: On the scaling law of the pinning force in MgB_2 superconducting composites with magnetic nanoinclusions. J. Supercond. Nov. Magn. **26** (2013) 125–131

[71] A. F. Salem, K. A., Ziq, A. A Bahgat, Scaling behavior in aluminium doped MgB_2 superconductor. J. Supercond. Nov. Magn. **26** (2013) 1517–1520

[72] M. R. Koblischka, A. Wiederhold, M. Muralidhar, K. Inoue, T. Hauet, B. Douine, K. Berger, M. Murakami, U. Hartmann: Development of MgB_2-based bulk supermagnets. IEEE Trans. Magn. **50** (2014) 9000504

[73] P. Badica, G. Aldica, A.M. Ionescu, M. Burdusel, D. Batalu, “The influence of different additives on MgB_2 superconductor obtained by ex situ spark plasma sintering: pinning force aspects. In: Nishikawa, H., Iwata, N., Endo, T., Takamura, Y., Lee, G.H., Mele, P. (eds.) Correlated functional oxides: nanocomposites and heterostructures, pp. 75–116. Springer, Berlin (2017)

[74] M. R. Koblischka, M. Muralidhar.: Pinning force scaling analysis of Fe-based High- T_c superconductors. Int. J. Mod. Phys. B **30** (2016) 1630017

[75] T. Matsushita, M. Kiuchi, A. Yamamoto, J. Shimoyama and K. Kishio “Essential factors for the critical current density in superconducting MgB_2: connectivity and flux pinning by grain boundaries” Supercond. Sci. Technol. 21 (2008) 015008

[76] S. X. Dou,a) S. Soltanian, J. Horvat, X. L. Wang, S. H. Zhou, M. Ionescu, and H. K. Liu “Enhancement of the critical current density and flux pinning of MgB_2 superconductor by nanoparticle SiC doping” Appl. Phys. Lett., **81** (2002) No. 18

[77] X.L. Wang, S. Soltanian, M. James, M.J. Qin, J. Horvat, Q.W. Yao, H.K. Liu, S.X. Dou,“Significant enhancement of critical current density and flux pinning in MgB_2 with nano-SiC, Si, and C doping” Physica C **408–410** (2004) 63–67

[78] Y. Zhao, M. Ionescu, A. V Pan, S. X. Dou, E W Collings “In situ annealing of superconducting MgB_2 films prepared by pulsed laser deposition*”* Supercond. Sci. Technol. **16** (2003) 1847.

[79] Y. Zhao, M. Ionescu, J. Horvat and S. X. Dou, “Comparative study of *in situ* and *ex situ* MgB_2 films prepared by pulsed laser deposition” Supercond. Sci. *Technol.* **17** (2004) S482

[80] N. Sakai, T. Oka, K. Yamanaka, L Dadiel, H Oki, J Ogawa, S Fukui, J Scheiter , W Häßler, K Yokoyama , J Noudem, M Miryala and M Murakami ” Occurrence Of Flux Jumps in MgB_2 Bulk Magnets During Pulse-Field Magnetization” J. Phys.: Conf. Ser. **1559** (202) 012024

[81] T. Hirano, Y. Takahashi, S. Namba, T. Naito and H. Fujishiro, “A record-high trapped field of 1.61 T in MgB_2 bulk comprised of copper plates and soft iron yoke cylinder using pulsed-field magnetization” Supercond. Sci. Technol. **33** (2020) 8.

[82] G Fuchs, W Häßler, K Nenkov, J Scheiter, O Perner, A Handstein, T Kanai, L Schultz and B Holzapfel, “High trapped field in bulk MgB_2 prepared by hot-pressing of ball-milled precursor powder” Supercond. Sci. Technol. **26** (2013)122002

[83] J. Bardeen, L.N Cooper, and J. R. Schrieffer, “Theory of superconductivity” Phys. Rev. **108** (1957) 5.

[84] C. Gilhotra and Sanjay, “Theoretical aspects of superconducting materials as its characteristics and applications in physics” AIP Conference Proceedings **2220** (2020) 110027

[85] J. R. Tobin, Superconductivity “Research and Development”, 2008- NOVA Science Publishers Inc.

Chapter II

Experimental methods and Sample Fabrication

In this work, one of the objectives is to enhance density, connectivity, flux pinning and improve the performance of MgB_2 bulk superconductor by chemical doping and advanced fabrication by SPS technique to further improve the connectivity and density, hence improving the superconducting performance. This work also aims at demonstrating practical applications of bulk MgB_2 by measurement of the trapped field by PFM. The various methods for making MgB_2 bulk superconductor will be described. Among these techniques, a high-pressure and temperature-method earlier mentioned as the SPS process has been developed for the synthesis of MgB_2 bulk samples. The experimental techniques used for sample characterization include X-ray diffraction (XRD), scanning electron microscopy (SEM), transmission electron microscopy (TEM), magnetic property measurements systems (MPMS) are also described. These various experimental methods are used to synthesize the samples chosen for study and investigate their structural, microstructural and magnetic properties. Among them, structural characterization was carried out for all synthesized samples by measuring X-ray Diffraction (XRD) patterns. Microstructural and compositional investigations were carried out employing the Field Emission Scanning Electron Microscopy (FE-SEM) and Energy Dispersive Spectroscopy (EDS). Magnetic Property Measurement System (MPMS) with Superconducting Quantum Interference Device (SQUID), magnetometer. SQUID facility is employed for measuring the magnetic moment as a function of magnetic field for the determination of critical current density of superconducting samples at various constant temperatures. The superconducting-to-normal transition temperature and its width are often obtained from magnetic susceptibility measurements which are carried out using the MPMS system. All of the techniques are briefly introduced in this chapter.

In this project, some bulk MgB_2 samples were made by the conventional in-situ methods. In addition, an in-situ and ex-situ spark plasma sintering (SPS) method was used to make dense and homogenous MgB_2 bulk. Pulse field magnetization (PFM) was also carried out to measure the trapped field on bulk sample produced by SPS process.

2.1 Fabrication of MgB_2 Samples

In the present work, MgB_2 superconducting samples were prepared in bulk forms. In-situ solid state preparation method was used for MgB_2 bulk [1-3]. Mg powder (-325 mesh, < 99.8 %, Furuuchi) and nano-boron powder (98.5 %, ~250 nm Furuuchi chemicals) were used for all type of preparative methods. Synthesis of bulk samples was done using single-step solid-state method. Powders of Mg

and B are mixed in a stochiometric ratio of 1:2, The first series was based on nanoscopic diamond powder addition (Sigma-Aldrich 98.5 % purity, ~10 nm). Compositions of 0, 0.4, 0.8, and 1.2 wt% of nanoscopic diamond powder was added to improve flux pinning performance of the bulk MgB_2 material. The second series was based on the synthesis of the Ag added bulk MgB_2 material to the best sample obtained in the nanoscopic diamond added bulk MgB_2 material in the first series, Ag powder (<1 μm submicron size) was added in amounts of 3.5, 4.0, 4.5 wt% based on the background literatures [18]. The third and final series was based on the utilization of the nano-boron, along with charcoal. The low cost homemade charcoal was added to further reduce the production cost of bulk MgB_2 without compromising the performance and to develop reliable manufacturing process for large scale bulk production. Equipment used for the fabrication. The doping of charcoal was varied at 0.0, 0.2, 0.4, and 0.6 wt%. Bulk MgB_2 samples were produced maintaining the same processing conditions from our previous projects. The mixing of the precursors were done in a glove-box in argon atmosphere to prevent reaction of Mg with Oxygen. 10 mm diameter and 7 mm pellets were obtained from uniaxial pressing of the precursors, sealed in Ti foils and then sintered in a furnace at 775 ^oC for 3 h in Ar atmosphere. Sintered samples then collected from furnace prior cooling to room temperature and then move to the characterization stage. This technique was effective and maintained for the entire series of samples produced at the course of this project. We shall discuss the different techniques utilized for fabrication of our bulk samples.

2.1.1 Solid State Bulk Processing of MgB_2

The in-situ solid state reaction technique was employed to fabricate the bulk disks of MgB_2. The synthesis was achieved from precursor powder materials of Mg powder (99.9% purity, 325 meshes) and nano-B powder (98.5% purity, ~250 nm). The raw materials were weighed 1.5 g in a glove box and thoroughly mixed under argon atmosphere. The powders were mixed and ground thoroughly in a ratio of 2:1 (2B + 1Mg) in a glove box for about 0.5 hrs to get homogeneous fine powder using an agate mortar and pestle while varying the compositions of the additives (silver Ag, nano-diamond and charcoal) which were added in separate experiments in their right proportions and varied. A uniaxial pressing machine was employed using a force of ~15 kN to press the precursors into pellets of 10 mm in diameter and 7 mm thickness. The resulting samples were then wrapped in titanium foils and subjected to heat treatment in a furnace, sintered at 775 ^oC for 3 h in flowing Ar atmosphere and finally cooled down to room temperature at a cooling rate of 100 $^oC\ h^{-1}$. The bulk polycrystalline samples of MgB_2 prepared using an *in situ* solid state synthesis method, namely the solid state single step process [4, 5] were characterized, analyzed and reported systematically which gives an insight to the subsequent developments by advanced processing techniques employed in one

of the chapters. Since the same applied force was used for the uniaxial pressing, the relative densities were all around 66%. Thus, the relative densities of the final products produced by this method were calculated by quotient of the bulk densities and the theoretical densities expressed as a percentage, the bulk densities were estimated by simple arithmetic division of the bulk mass in grams by its volume in grams per cubic centimeter, hence the equation;

$$\textit{Relative density [\%]} = \frac{\textit{Bulk density}}{\textit{Theoretical density}} \times 100$$

Here, the theoretical density of MgB_2 was used as 2.62 g/cm^3 for all samples produced by the tubular sintering method of bulk processing explained in this chapter.

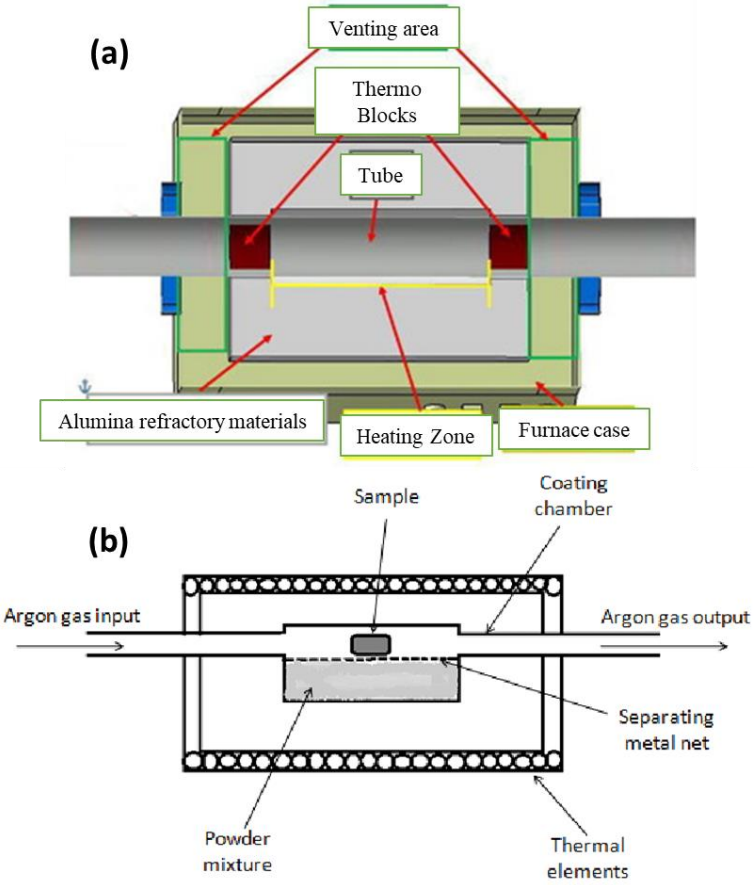

Figure 2.0 Schematics of tubular furnace showing (a) different parts and (b) mechanism of operation and sample position during MgB_2 synthesis

A schematic diagram of the furnace and preparation procedure for the method is shown in figure 2.0. The powder mixture is then densely packed and subjected to uniaxial pressing to get a disk-shaped bulk material. The temperature profile for the sintering program is shown in figure 2.2. Heat treatment of all the samples was done in a programmable tubular furnace having stability and accuracy.

Disk-shaped MgB_2 superconductor was taken out of the furnace after sintering as shown by the procedures in figure 2.1. This is followed by grinding the edges of the samples and then mechanically peeling off the titanium wraps for structural and superconducting characterizations. An example of a tubular sintered sample obtained from this technique is later shown in figure 2.4.

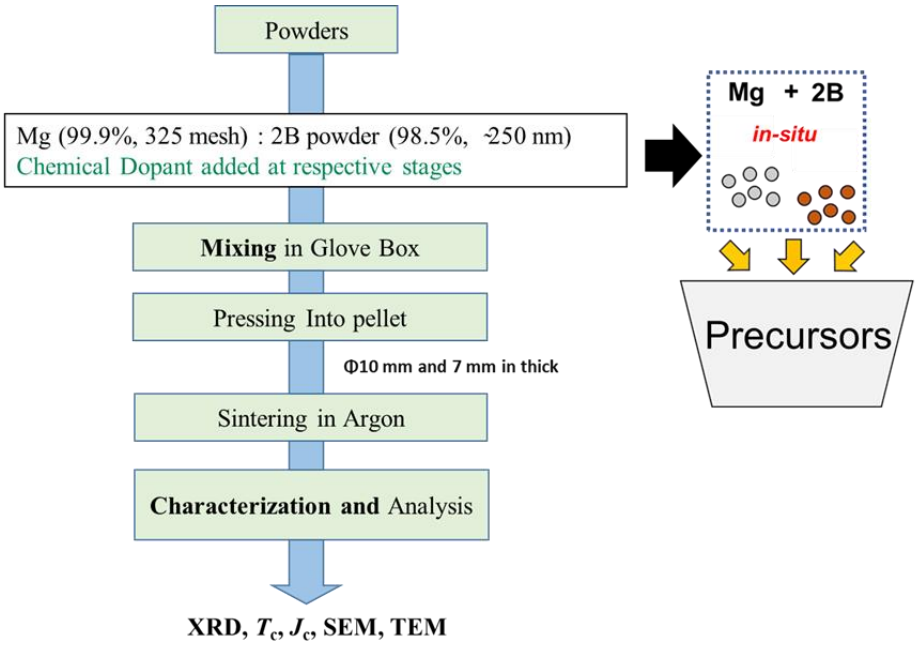

Figure 2.1 Steps involved MgB_2 fabrication by tubular furnace

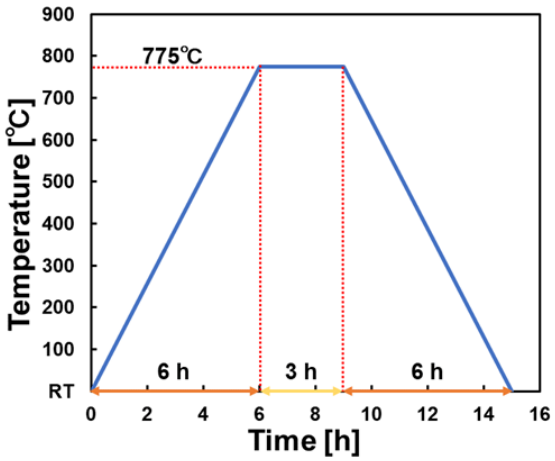

Figure 2.2 Temperature Profile for sintering program of MgB_2 samples at 775 ºC for 3 hrs.

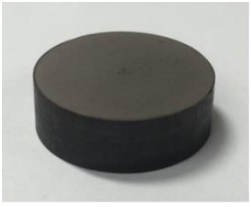

Figure 2.3 Sintered MgB_2 bulk sample

2.1.2 Spark Plasma Sintering

The working principle of the spark plasma sintering (SPS) technique is that it involves the contemporaneous use of uniaxial pressure and high-intensity, low-voltage, pulsed current [19]. In general terms, SPS can be considered a modification of hot pressing, where the furnace is replaced by the mold containing the sample, that is heated by a current flowing directly through it and eventually through the sample. SPS is a typical field assisted sintering technique, which can achieve fully dense compacts by using low processing temperature and short sintering time [6]. One of the considerable advantage of this technique is that we can produce highly dense and homogenous bulks within a short time. Generally, the SPS process involves four stages as illustrated in figure 2.4. The variable parameters could be temperature, pressure and/or current which increases gradually with respect to the time taken for the sintering process.

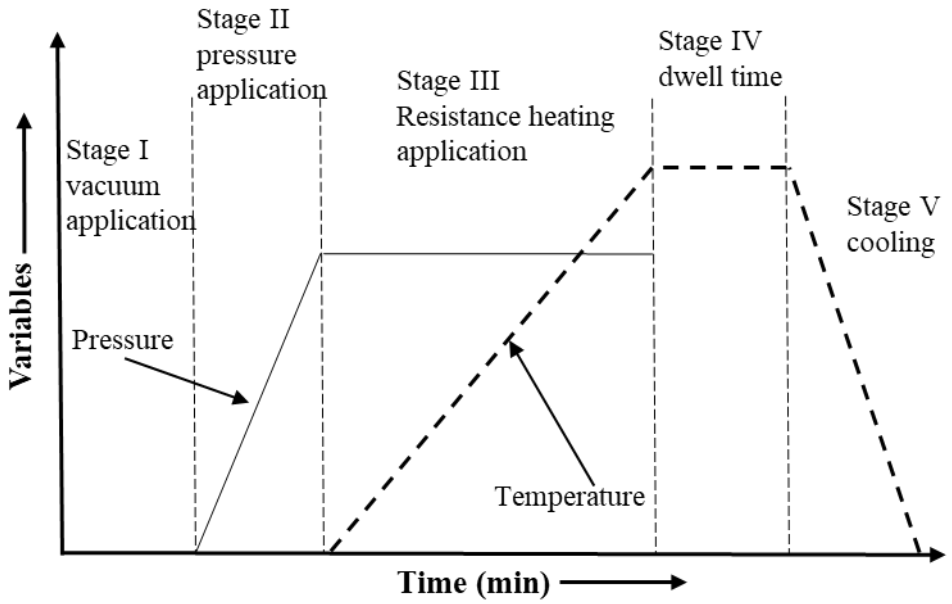

Figure 2.4: Stages involved in the SPS MgB_2 bulk processing

A schematic of the SPS chamber is further explained and shown in figure 2.5, in this project we employed the SS Alloy Co., Ltd SPS machine. In this study, two sets of samples were synthesized by SPS ex-situ and *in situ* and considered for this study. The first series of samples were fabricated by SPS with a commercially available (MgB_2, purity >97%, 100 meshes) powder obtained commercially from Kojundo chemicals. In the ex-situ process, the admixed MgB_2 powder was inserted into the graphite die under ambient atmosphere and then charged into the SPS sample chamber similar to *in situ* synthesis. The graphite die was heated within the ranges of 800 °C - 1000 °C with same rate of 50 °C min^{-1} by simultaneous application of current pulses for 15 min of dwell time. Further, the dwell

time was optimized by varying for 1 - 10 min. for the sample fabricated at optimal sintering temperature of 850 °C. At the end of each process, all samples were then furnace cooled to room temperature (RT). Final SPS ex-situ products were referred as *ex-situ-W-Z* where *W* and *Z* represents the sintering temperatures and the dwell times respectively). In the overall process, after removing the bulk sample from the SPS chamber, the graphite layer and the carbon-contaminated surfaces were removed polishing by SiC papers. The relative bulk densities of all the samples were estimated using the theoretical density of MgB_2. The second series of samples investigated in this work were prepared by the *in-situ* SPS technique. For the *in-situ* SPS process, 0.6g of the Mg (99.9%, 325 mesh) and B (98.5%, 250 nm) powder obtained from Kojundo chemicals were mixed in the ratio of 1:2 and was loaded into a φ10 mm graphite die in a glovebox filled with high pure Ar The schematic of the SPS sample chamber is shown in Figure 2.5(a) and (b). The graphite die has an inner diameter of 10 mm lined with boron nitrite (BN) and placed in the SPS apparatus (SS Alloy Co., Ltd). The schematic diagram in figure 2.5 (b) also shows the cross section of the graphite die and its components. The sample chamber was evacuated and then, filled with argon gas to a pressure of 0.5 atm. A pressure of 50 MPa was applied to the filled powder through the graphite die. The heating on the graphite commenced with the sintering temperatures being recorded for 720 °C - 775 °C ranges at the rate of 50 °C min^{-1} and these set of samples were named as *in-situ-X-Y* where *X* and *Y* are the sintering temperatures and dwell times respectively.

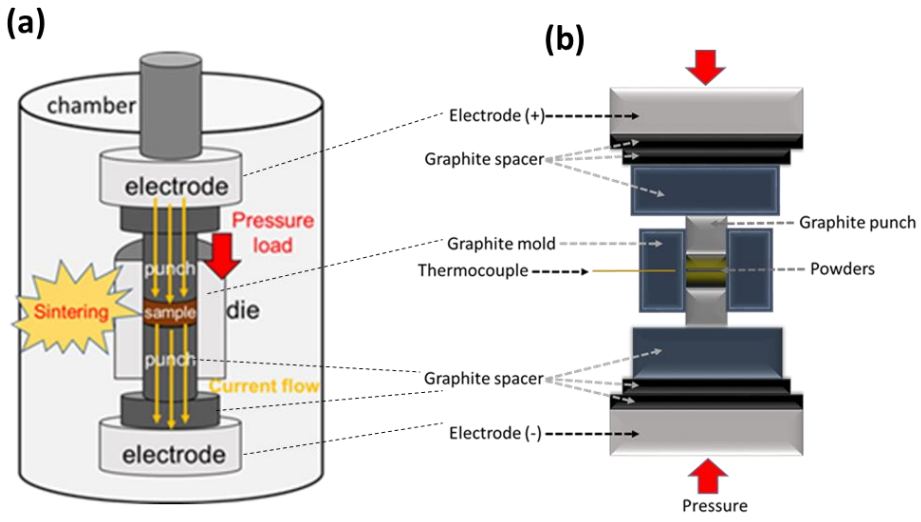

Figure 2.5: Schematic diagram of an SPS furnace

The experimental procedure of the SPS process is described systematically in figure 2.6. This implies that both in situ and ex-situ bulk processing follow the same steps in SPS processing. The differences are noted in controlling the parameters involved since the sintering conditions are not the same for the two distinct SPS synthesis.

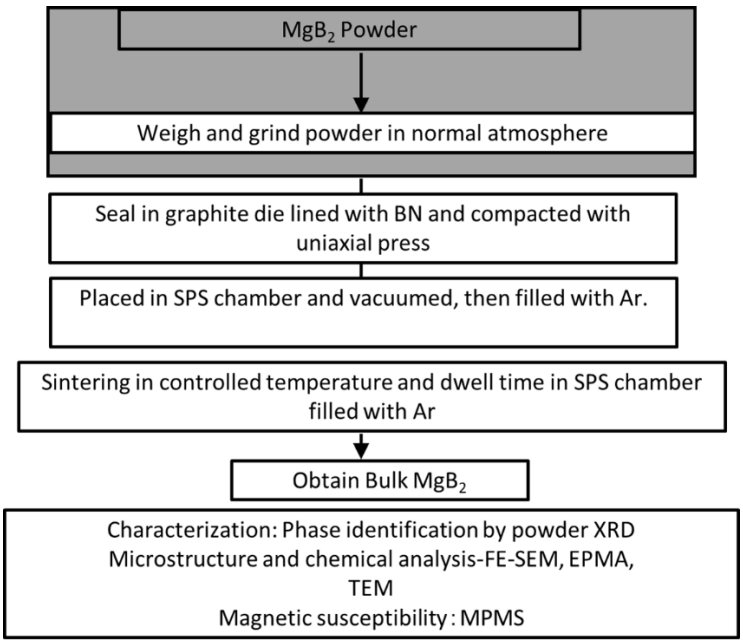

Figure 2.6: Experimental procedure for SPS bulk processing

2.2 Characterization Techniques

2.2.1 X-ray diffraction (XRD) analysis

The X-ray powder diffraction technique was employed in this study for the phase identification of the samples. This technique has been further explained in this chapter. In 1913, English physicists *Sir W. H. Bragg* and his son *Sir W.L. Bragg* [10-11] developed the relationship, $n\lambda = 2d \sin\theta$ to explain why the cleavage faces of crystals appear to reflect X-ray beams at certain angles of incidence (θ). The variable "*d* " represents the distance between atomic layers in a crystal, the parameter is the incident X-ray beam's wavelength, and n is a number indicating the order of reflection. This was the direct proof for the periodic atomic structure of crystals, and it was an example of X-ray wave interference, also known as X-ray diffraction (XRD). "A. W. Hull discovered in 1919 that "every crystalline component forms a separate pattern that is independent of the other compounds." As a result, a pure material's X-ray diffraction pattern serves as a fingerprint. [11]. As a result, powder diffraction is a useful tool for finding and characterizing polycrystalline phases. A random distribution of all conceivable (h, k, and l) planes should be present in the sample. Only crystallites with parallel reflecting planes (h, k, 1) contribute to reflected intensities, and any conceivable reflection from a given set of h, k, l planes has an identical number of crystallites. The X-ray is swept across the sample at a glancing angle to produce all possible reflections. Figure 2.7 depicts a schematic representation of Bragg's law. In the present study, the crystal structures and constituent phases were investigated using a high resolution X-ray powder diffractometer (Rigaku/Smart Lab), using Cu K_α radiation with wavelength of 1.5405 Å. The samples were scanned with a step size of 0.020 from 20 to 90 (2 values).

A regular scan should take no more than 10 minutes. After being totally crushed, the bulk materials were finely powdered. The powder samples were then put in standard sample containers, and XRD data was collected at room temperature. The JCPDS-PDF II database was used to determine the phases of the samples based on the XRD data.

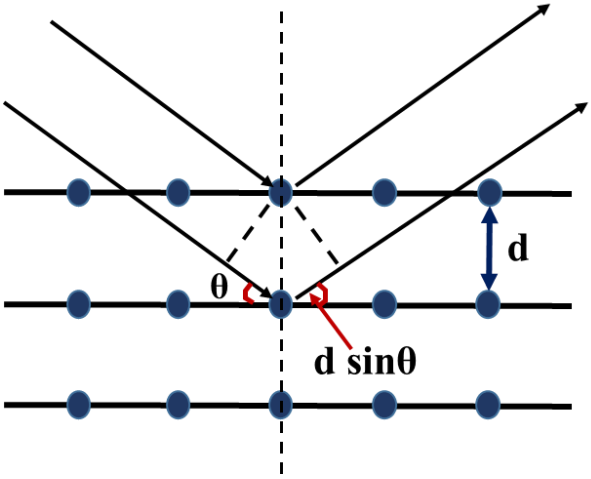

Figure 2.7: A schematic diagram of the Bragg's law condition where the incident beam and diffracted beam follow $n\lambda = 2d\sin\theta$

An XRD peak's full width at half maximum (FWHM) is determined by crystalline size, lattice strain, instrumental parameters, and other variables. The FWHM of selected MgB_2 peaks is commonly used to measure the lattice strain and grain size qualitatively. The Williamson-Hall plot (FWHM×cosθ versus sinθ) is often used to determine lattice strain and crystallite size from the slope and y-intercept, respectively [7], however we only looked at the phase analysis in this study. Other criteria such as the size of the grains were evaluated in order to gather grain size information, which is explained in the microscopy sections of the results sections.

2.2.2 Microstructural Characterizations:

Microstructural properties provide information on the key parameters responsible for enhancement of J_c in superconductors. Microstructural analysis of complex non-stoichiometric material has a lot of challenges. In order to prepare specimens for microstructural characterization, the samples were either fractured or sliced into thin sections using a low speed diamond cutter. The specimens were further polished on polishing cloth on the rotating wheel of a Buehler polishing machine, using different grades (6, 3, 1, 0.25 μm) of diamond paste as grinding media. ethanol was used as a lubricant during polishing. The surface was cleaned after every stage of polishing. Polishing time at each stage ranged from 2 to 30 minutes with silicon carbide paper and 0.5-2 hours with diamond paste. The polished surface of the sample was then cleaned with methanol and dried in

hot air. In the present study, no etching was done to the polished surface of the samples. The micrographs thus obtained were characterized for various microstructural parameters using quantitative metallographic methods as explained below. The Field Emission Scanning Electron Microscope (FE-SEM) and Energy Dispersive X-ray Spectrometer (EDS) are the tools used to perform microanalysis on these materials such as observe the grain size, presence of secondary phases and their distribution, defects and voids, twinning, etc.

2.2.3 Scanning Electron Microscope (SEM)

SEM is one of the most versatile and well known analytical techniques for microstructural studies. Compared to conventional optical microscope, an electron microscope offers advantages including high magnification, large depth of focus, great resolution and ease of sample preparation and observation. The JSM-7001F Schottky field emission scanning electron microscope is a general-purpose high-resolution scanning electron microscope that can handle a wide range of samples, from semiconductors to magnetic materials. The JSM-7610F is a semi-in-lens Schottky Field Emission Scanning Electron Microscope with ultra-high resolution. High performance analysis are possible with high-power optics. It's also appropriate for high-resolution analysis. Electrons generated from an electron gun enter a surface of a sample and generate many low energy secondary electrons. The intensity of these secondary electrons is governed by the surface topography of the sample. An image of the sample surface is therefore constructed by measuring secondary electron intensity as a function of the position of the scanning primary electron beam.

The SEM employs a high-energy electron beam (in keV) and helps in imaging the topography of the sample surface by operating in a raster scan mode. In the case of a FE-SEM, a field-emission cathode in the electron gun of a FE-SEM provides narrower probing beams at low as well as high electron energy, resulting in both improved spatial resolution and minimized sample charging and damage. The electrons, when they interact with the atoms of the sample, produce secondary electrons, back-scattered electrons, transmitted electrons, characteristic X-rays etc. A typical schematic sketch representing the above mentioned processes are shown in figure 2.8. Separate detectors are present to pick up the information from each of these processes. The secondary electron imaging can produce very high-resolution images of a sample surface, revealing details even in the size range 10 - 100 nm. Due to the very narrow electron beam, FE-SEM micrographs have a large depth of field yielding a characteristic three-dimensional appearance useful for understanding the surface structure of a sample.

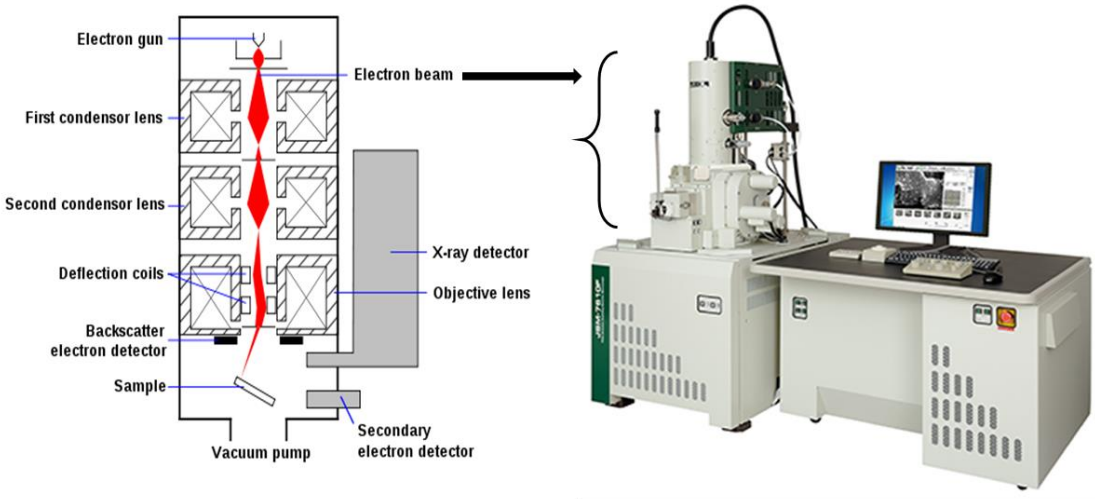

Figure 2.8: A schematic picture showing emission of electron beam and presence of various detectors in the SEM.

Electron beam of very high energies are employed in order to visualize the sub-surface structures while low energy BSE detection is quite useful for high resolution investigation of specimen that accumulate surface charge, in spite of thin gold coating. A new in-lens detecting mechanism helps to achieve this. The electron optical column is fitted with a positively biased booster that adjusts the energy of the main electrons in order to decrease aberrations and susceptibility to interfering stray-fields. The incident beam is focused using a grounded pole piece cap and a magnetic lens with an axial gap to prevent field leaking to the specimen. The electrons are decelerated to the required primary energy shortly before hitting the material. A suitable explanation for the reduction of spherical and chromatic aberrations is that the electron beam is focused by the objective lens at higher energies and smaller electron beam diameters. Another advantageous effect of this arrangement is the collection of secondary electrons emerging from the sample surface attracted and accelerated by the positively biased electrode of the beam booster and finally projected onto the In-lens detector. Characteristic X-rays are emitted when the electron beam removes an inner shell electron from the sample, causing a higher energy electron to fill the shell and release energy. These characteristic X-rays are used to identify the composition and measure the abundance of elements in the sample. The instrument used in this study can magnify images to about 200 nm. Freshly fractured surfaces of the samples were mounted on aluminum studs using adhesive carbon tapes. Polished surfaces were also used for some samples. Since the superconducting MgB_2 is electrically conducting, gold coating was not required. Finally, the aluminum studs with the mounted samples were loaded on the sample holder of the microscope.

2.2.4 Energy Dispersive X-ray Spectroscopy:

To get the composition of different phases observed through microstructural studies in the samples, they were individually selected and investigated through EDS. Through different techniques like point scan, area scan, line scan and mapping on the sample, relative amounts of different elements present in each of the phases is estimated. Energy Dispersive X-Ray Spectroscopy (EDS) is an analytical technique that qualitatively and quantitatively identifies the elemental composition of materials analyzed in SEM. EDS analyzes the top two microns of the sample with a spatial resolution of one micron. Beryllium windowed EDS detect all elements with atomic numbers greater than oxygen at concentrations greater than 0.1%. "Windowless" EDS detectors can also detect carbon, nitrogen and oxygen at concentrations greater than 1.0%. EDS displays the distribution of elements as either dot maps or line profiles with a spatial resolution of one micron. When the electron beam of the FE-SEM is scanned across the sample, it generates X-rays from the atoms. X-rays are produced as a result of the ionization of an atom by high-energy radiation wherein an inner shell electron is removed. To return the ionized atom to its ground state, an electron from a higher energy outer shell fills the vacant inner shell and, in the process, releases an amount of energy equal to the potential energy difference between the two shells. This excess energy, which is unique for every atomic transition, will be emitted by the atom either as an X-ray photon or will be self-absorbed and emitted as an Auger electron. The energy of each X-ray is characteristic of the atom from which it escapes. The EDS system collects the X-rays, sorts them by energy and displays the number of X-rays versus their energy. This qualitative EDS spectrum can be either photographed or plotted. This data can then be further analyzed to produce either an area elemental analysis (displayed as a dot map) or a linear elemental analysis (displayed as a line scan) showing the distribution of a particular element on the surface of the sample. The EDS data can be compared to either known standard materials or computer-generated theoretical standards to produce either a full "quantitative" or a "semi-quantitative" analysis. The location of the peaks on the energy scale identifies the elements. The peak heights vary because each transition has different probability of occurring and the detector's efficiency is a function of energy. The EDS spectrum has a peak width because the energy dispersion is a statistical event, i.e. every photon does not produce the same number of electron - hole pairs and there is thermal noise caused by the amplification process.

2.2.5 Transmission electron microscopy (TEM)

Fine microstructure may be observed and characterized directly using TEM. TEM has a better resolution (0.2 nm) than SEM, allowing for a more detailed examination of microstructures. In addition to grain morphology, electron diffraction patterns may be utilized to gain detailed

information on crystal structure, flaws, and lattice structure. In this study, TEM was also used to get intra and intergrain features of polycrystalline MgB_2 and to determine the grain morphology, grain size and information of the nano-sized inclusions. The TEM (Titan Themis G2 80-200kV X-FEG) equipped with an X-ray energy dispersive spectrometer (EDS) was used in this work. Finely polished thin samples were mounted on carbon-coated copper grids before being inserted into the device. Energy dispersive X-ray (EDX) analysis was also performed in this study utilizing an automated EDS system connected with the TEM. Depending on the demand, the analysis was done at an area of frame.

Physical Property Measurement System

The superconducting quantum interference device (SQUID) was employed to detect the magnetic fields based on the response of the superconducting samples to applied fields. Hence, the main data obtained from this technique are the critical temperature and critical current densities.

1. **Critical Temperature/Transition Temperature (T_c):** A superconducting material's critical temperature is the temperature at which it transitions from a normal conducting to a superconducting state. The change from a normal conducting to a superconducting state (phase) is abrupt and complete. The magnetic susceptibility measurement acquired from the SQUID device is used to determine this property.

2. **Critical current densities (J_c):** A magnetic field is created when a current is conducted via a superconducting conductor. The magnetic field rose up to a critical threshold when the current exceeded a particular amount, at which point the conductor returned to its normal condition. The critical current is the value of current. It's derived from the hysteresis loop's magnetic moment changes, which are discussed later in the next section.

2.4 Superconducting Performance

The magnetic characteristics of MgB_2 have been measured in self and applied magnetic fields to examine their superconducting capabilities. The superconducting parameters T_c, J_c, and the irreversibility field H_{irr}, as defined in 2.4.1, were measured. The T_c is calculated from the DC magnetic susceptibility, whilst the J_c and H_{irr} are calculated from the magnetic hysteresis loop (M-H data) when studying the electromagnetic characteristics of MgB_2 samples created under various circumstances. MPMS (Magnetic Property Measurement System) was used to measure DC magnetization up to 5 T. For self-field transport experiments, an indigenously developed cryostat with helium-based cryocooler was employed, and a 5 T LHe cooled solenoid magnet was used for field transport measurements. The magnetization measurements were performed on smaller specimens taken from the bulk materials.

2.4.1 Magnetization measurements

The SQUID (Superconducting Quantum Interference Devices) Magnetometer was used to detect high field magnetization for this investigation. For the measurements, bulk samples with typical dimensions of 2.0 × 2.0 x 1.0 mm were employed. The samples were measured with a magnetic field applied along their longest dimension. *M-T* (magnetization vs. temperature) experiments were carried out at temperatures ranging from 0 to 5000 Oe, mostly in a zero field cooling (ZFC) environment. At 10 K-20 K and up to 5 T, *M-H* (magnetization vs. field) hysteresis loops were measured. The temperature at which the *M-T* plot shows the commencement of diamagnetic property is estimated and the difference between the temperatures corresponding to 90% and 10% of the greatest shielding signal is defined as T_c.

2.4.2 M-H hysteresis loops and critical current density measurements:

The critical current density (J_c) in type-II superconductors can be estimated by analyzing the magnetization using the Extended Critical State model proposed by C.P. Bean [7]. The model assumes that the penetrated super-currents flow with a density equal to J_c independent of the local internal field. If this magnitude of the current flows everywhere in the specimen, it means that it is in the critical state.

The process of magnetization of a slab of thickness 2a in a field parallel to its surface is shown in figure 2.9, when the current density is independent of the external field.

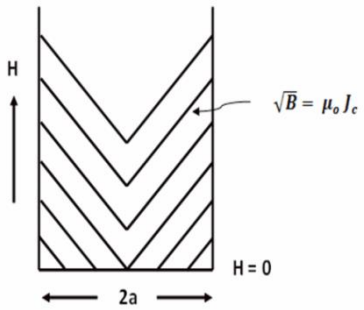

Figure 2.9**:** Magnetization process of thin slab of thickness 2a in a field parallel to the surface [13].

The field within the specimen decreases linearly with distance, if the material is in critical state. The Maxwell's equation is

$$\sqrt{\boldsymbol{B}} = \boldsymbol{\mu_0 J_c} \quad \text{..... (2)}$$

Where J_c is the critical current density in Am^{-2}, B is the magnetic induction in Tesla and μ_o is the absolute permeability.

The local internal field H_i is given as

$$\boldsymbol{H_i = \frac{B}{\mu_o}} \text{..... (3)}$$

Where B is the macroscopic local flux density.

The local magnetization M_i becomes, $M_i = H_i$ - H, where H is the applied field. The total magnetization M is the average of M_i, over the sample cross-section.

If we consider the magnetization for two stages namely

(i) $0 < H < H^*$ and (ii) $H^* < H$

Where H^* is the applied magnetic field at which the internal field reaches the centre of the specimen.

For an infinite slab, the initial magnetization curve M(H) becomes

$$\boldsymbol{M\ (H) = -H + \frac{H^2}{2J_c a}\ , for\ 0 < H < H^*} \quad \text{..... (4)}$$

$$\boldsymbol{M(H) = -\frac{J_c a}{2}\ , for\ H^* < H} \quad \text{..... (5)}$$

The reverse curve for high $-H_m$ ($H^* < H_m$) case is given by

$$\boldsymbol{M(H) = -\frac{J_c a}{2} + H_m - H - \frac{(H_m - H)^2}{4J_c a}, for\ H_m - 2H^* < H < H_m} \quad \text{.....2.11}$$

$$\boldsymbol{M(H) = \frac{J_c a}{2}, for - H_m - H < H_m - 2H^*} \quad \text{..... (6)}$$

Where H is the applied magnetic field, H_m is the maximum applied field and 2a is the thickness of the slab.

When $H_m > 2H^*$, J_c is related to the magnetization M for slab of thickness 2a as

$$\boldsymbol{M(H^+) - M(H^-) = J_c a} \quad \text{..... (7)}$$

Therefore, J_c can be determined by measuring the width of an M-H hysteresis loop at a given field. The discussion made above is applicable only if the sample is considered as an infinite slab.

For the orthorhombic geometry

$$M(H)^{+} - M(H)^{-} = J_c b\left(1 - \frac{b}{3a}\right) \quad \ldots\ldots\ldots (8)$$

2.4.3 Calculation of J_c from *M-H* loops:

Magnetization hysteresis loops representing magnetization (M) as a function of applied magnetic field (H) were recorded on the samples at various cryogenic temperatures using the superconducting quantum interference device (SQUID) magnetization measuring system utilize for magnetic property measurement system (MPMS-5), Quantum design.

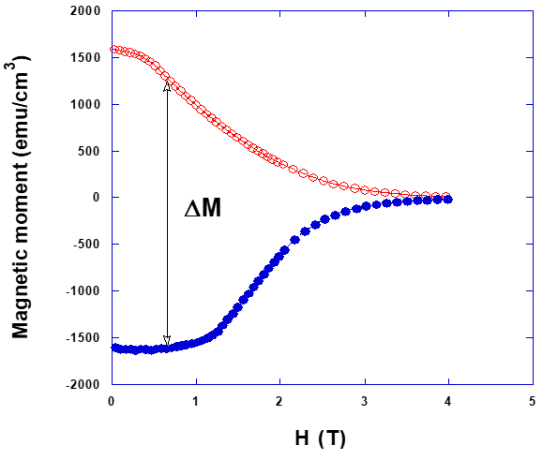

Figure 2.10: A typical magnetic hysteresis (*M-H*) loop for MgB_2 superconductor.

The specimens used for the measurements were of size approximately 2 mm x 2 mm x 1 mm, which were cut such that their long dimension was normal to the pressed surface of samples. The samples were exposed to magnetic fields of up to 5 Tesla generated by superconducting magnet in order to record the field dependences of magnetization. A typical *M-H* loop obtained for a superconductor is shown in figure 2.10. Critical current densities (J_c) of the samples were determined following extended Bean's critical State model using the relation [8-9]:

$$J_c = \frac{20\ \Delta M}{d} \quad \ldots\ldots\ldots (9)$$

where $\Delta M = M^{+} - M^{-}$ (in emu/cc), $d = b\left(1 - \frac{b}{3a}\right)$; a > b and a, b are broad and narrow dimensions of the sample (in cm). H_{irr} values of selected samples were estimated as the field at which J_c falls below 100 A/cm^2 at 20 K.

2.4.4 Flux Pinning Mechanism:

Here, we further explain the concept of flux pinning mechanisms which was employed for all samples estimated from available J_c data. The superconductor usually must be a Type-II superconductor because Type-I superconductors cannot be penetrated by magnetic fields. This pinning is what holds the superconductor in place thereby allowing it to levitate [14]. The expressions for flux-pinning in most type II superconductors are derived from considerations of the nature of the interaction between individual flux-lines and pinning-centers, which includes the geometry of the pinning-centers. In most cases, it could also be demonstrated experimentally that the observed scaling laws explained in chapter 1 which can be obtained without the necessity of introducing the concept of flux-lattice elasticity. Predicted pinning functions are found to provide adequate explanation of measured Lorentz force curves in a wide range of high magnetic fields, strong-pinning materials [14,15,16].

2.5 Pulse Field Magnetization

Pulsed field magnetization (PFM) is a method for magnetizing a superconductor that involves utilizing a strong electromagnet that is powered by a rapid pulse of electric current rather than a continuous current, resulting in a brief but intense magnetic field pulse. Pulsed field magnets, which can produce greater magnetic fields than continuous magnets, are used in research in subjects such as materials science to explore the effects of intense magnetic fields. The tremendous waste heat generated in the windings by the large currents required limits the maximum field strength that continuously-powered high-field electromagnets can achieve. Stronger currents can be employed and thus stronger magnetic fields can be generated by applying brief bursts of current with time between pulses to allow the heat to dissipate. Pulsed field magnets produce a magnetic field that can range from 50 to 100 T and lasts several tens of milliseconds [20]. For PFM, numerical modeling employing electromagnetic and thermal fields can qualitatively reproduce the experimental results. Because of the great thermal conductivity, small specific heat, and limited temperature margin against the transition temperature T_c, the flux dynamics and heat generation/propagation in the MgB_2 bulk during PFM were in stark contrast to those in REBaCuO superconducting bulks [21]. Some common related terms with this subject include applied field, trapped field, penetrated field, field capture ratio, flux jumps, shielding effects, flux flow which will be briefly explained.

2.5.1 Applied Magnetic Fields:

Bulk MgB_2 superconductors were characterized by applying magnetic fields using PFM technique in order to measure the trapped magnetic fields. Magnetic fields are formed by moving electric charges and the intrinsic magnetic moments of basic particles associated with a fundamental

quantum characteristic, their spin. The electromagnetic force, which is one of nature's four basic forces, is made up of magnetic and electric fields, which are interconnected. Rotating magnetic fields are required by both electric motors and generators. Magnetic circuits are used to mimic and investigate how magnetic fields interact in electric devices like transformers [22] [23]. Magnetic forces are used in the Hall effect to expose information about charge carriers in a material. The Hall effect uses magnetic forces to reveal information about charge carriers in a substance. The so called Hall effect can be simply described as the generation of a voltage difference (the Hall voltage) across an electrical conductor that is transverse to the current and perpendicular to the applied magnetic field. Edwin Hall first discovered it in 1879 [24].

2.5.2 Trapped Fields, Penetrated Fields, Field Capture Ratio:

This simply denotes the magnetic field that is trapped or stored temporarily in a superconductor after it undergoes magnetization. Throughout this work we will represent it by B_T. During the PFM process, magnetic measurements were obtained 1 hour after raising the external field to its highest value of 2.0 T and then lowering it to zero. Before running the measurements, each temperature was stabilized for 30 minutes. Generally, the highest B_T values grew dramatically as the temperature is decreased from 40 to 14 K. The B_T value is generally proportional to both values of $J_c(B)$ and the diameter of the bulk, based on the Bean's critical state model [25], suggesting that the larger bulk provides a higher B_T under the same $J_c(B)$ properties. Therefore, the temperature, which strongly affects the $J_c(B)$ properties, becomes another key factor in determining the B_T value. The small bulks were 'homogeneously' cooled by a cryo-cooler aided with liquid nitrogen (N_2). The heat transfer is by conduction cooling from the bottom of the cold stage to the top surface of the bulk where the hall and temperature sensors are attached. Due to the anisotropic thermal property of MgB_2, this consequently degrades the value of B_T; this phenomenon was also confirmed by numerical simulations [26]. Therefore, the bulk magnets should be cooled homogeneously to fulfil their potential in practical applications. A better way to explain all the parameters is shown in figure 2.11.

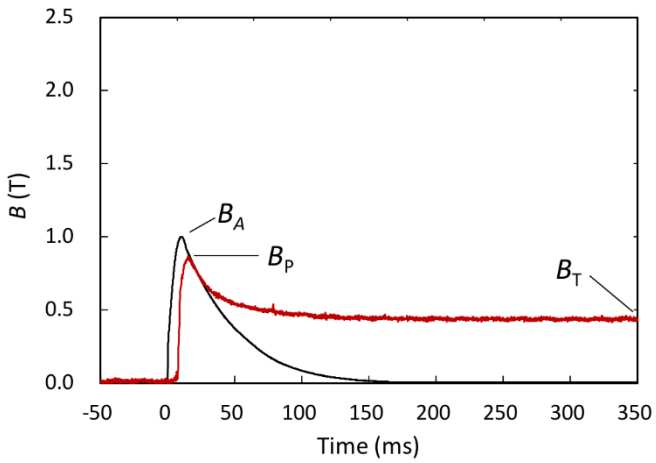

Figure 2.11; Illustration of time dependence during PFM of B_A, B_P and B_T

Black line: Behavior of applied field

Red line: Flux penetration behavior in bulk

In a more concise description to define the parameters:

The maximum peak of black line represents the applied field B_A, the maximum peak of red line represents the penetrated field B_P, the value that took enough time is the trapped field B_T.

The indicator for the heat generation is given by the field capture rate (F.C.R) expressed as percentage, thus;

$$\text{F.C.R } [\%] = B_T/B_P*100 \ldots\ldots\ldots \textbf{(10)}$$

This equation is our determinant. This implies that when this value is large, it can be said that the heat generation is small and vice versa.

We defined B_P/B_A and B_T/B_P as the respective parameters indicating field penetration ratio and field trapping ratio. These parameters reflect “shielding effects” and “heat generation/transfer

2.5.3 Flux Jumps:

In an attempt to find an easy way to explain flux jumps, the magnetic flux entering or leaving a solid cylindrical specimen of a type-II superconductor in an external, time-varying, axial magnetic field can do so via "flux bundles" made up of numerous distinct fluxoids. [27]. The flux jumps appeared as a set of irregularly shaped voltage pulses induced by flux motions [28], the resulting effects due to the heating produces flux jump which plays significant role in the degrading of the measured trapped fields also enhanced by the uneven distribution of heat in the MgB_2 superconducting bulk sample.

References

[1] Muralidhar Miryala, Sai Srikanth Arvapalli, Pavel Diko, Milos Jirsa, and Masato Murakami**,** **"**Flux Pinning and Superconducting Properties of Bulk MgB_2 with MgB_4 Addition**"** Adv. Eng. Mater. **22 (**2020**)** 1900750

[2] S. Soltanian, J. Horvat, X.L. Wang, P. Munroe, S.X. Dou "Effect of nano-carbon particle doping on the flux pinning properties of MgB_2 superconductor" Physica C **390** (2003) 185–190

[3] R. G. Abhilash Kumar, K. Vinod, R. P. Aloysius and U. Syamaprasad, Mater. Lett. **60** (2006) 3328

[4] N. Varghese, K. Vinod, S. Rahul, P. Anees, K. M. Devadas, Syju Thomas, Shipra, A. Sundaresan, S. B. Roy and U. Syamaprasad, J. Am. Ceram. Soc**. 94**, 1133 (2011)

[5] J.G Noudem, Y. Xing, P. Bernstein, R. Retoux, M. Higuchi, S.S. Arvapalli, M. Muralidhar & M. Murakami "Improvement of critical current density of MgB_2 bulk superconductor processed by Spark Plasma Sintering" J. of the Amer. Cer. Soc, **103** (2020), 6169-6175

[6] W.L. Bragg, "The refelction of X-rays by crystals" Proc. R. Soc. A **89** (1913) 248-277.

[7] C.P. Bean, "Magnetization of hard superconductors" Phys. Rev. Lett. **8** (1962) 250.

[8] D. X. Chen and R. B. Goldfarb, "Kim model for magnetization of type-II asuperconductors" J. Appl. Phys. **66** (1989) 2489.

[9] W.L. Bragg, "The structure of some crystals as indicated by their diffraction of x-rays" Proc. Camb. Philos. Soc. **17** (1913) 43-57.

[10] J. Humphreys, "The significance of Bragg's law in electron diffraction and microscopy, and Bragg's second law" Acta Cryst. **69** (2013) 45–50.

[11] M. Couach and A. F. Khoder, Magnetic Susceptibility of Superconductors and other Spin Systems edited by Hein R A, Francavilla T L and Liebenberg D H 1992 (Plenum, Neyork)

[12] S.D. Murphy, K. Renouard, R. Crittenden and S. M. Bhagat, "AC susceptibility of sintered high T_c superconductors — Bean's model and shielding current" Solid State Commun. **69** (1989) 367.

[13] M. Murakami, M. Morita, K. Doi and K. Miyamoto, Jpn. J. Appl. Phys. **28** (1989) 1189.

[14] D. Dew-Hughes "Flux pinning mechanisms in type II superconductors", Philosophical Magazine, **30** (1974) 293-305

[15] A. Yamamoto, J. Shimoyama, S. Ueda, Y. Katsura, I. Iwayama, S. Horii, K. Kishio, Crystallinity and flux pinning properties of MgB_2 bulks, Physica C **445–448** (2006) 806–810

[16] S. Soltanian, J. Horvat, X.L. Wang, P. Munroe, S.X. Dou, Effect of nano-carbon particle doping on the flux pinning properties of MgB_2 superconductor, Physica C **390** (2003) 185–190

[17] M. Muralidhar, K. Inoue, M. R. Koblischka, A. Murakami and M. Murakami, Effects of Silver Addition on Critical Current Densities and Mechanical Properties in Bulk MgB_2 Advanced Engineering Materials **17** (2015) 6

[18] W. Yucheng, F. Zhengyi, Study of temperature field in spark plasma sintering, Materials Science and Engineering B **90** (2002) 34–37

[19] A. G. Webb, "Radiofrequency microcoils for magnetic resonance imaging and spectroscopy". Journal of Magnetic Resonance. **229** (2013) 55–66.

[20] H. Fujishiro, T. Tamura, T. Arayashiki, M. Oyama, T. Sasaki, T. Naito, G. Giovanni and A.F Alessandro, Jpn. J. Appl. Phys. **51** (2012) 103005

[21] F.P Richard, L.B Robert, M.S Matthew, "The Feynman Lectures on Physics" California Institute of Technology, **2** (1963) ISBN 978-0465040858

[22] J. C, David., Introduction to magnetism and magnetic materials (2^{nd} edition), CRC. ISBN 978-0412798603 (1998) 3

[23] E. Hall, "On a new action of the magnet on electric currents" American Journal of Mathematics, **2-3** (1879), 287-92

[24] C. P. Bean, "Magnetization of Hard Superconductors" Phys. Rev. Lett. **8** (1962) 250

[25] T. Naito, Y. Takahashi, and S. Awaji, "A record-high trapped field of 5.6 T in the stacking of MgB_2/TiB_2 composite bulks prepared by an in-situ hot isostatic pressing method", Supercond. Sci. Technol. **33** (2020)125004

[26] C. Heiden and G. I. Rochlin, "flux jump size distribution in low-k type-II superconductors", physical review letters, **21** (1968) 691

[27] S.L. Wipf, "Review of stability in high temperature superconductors with emphasis on flux jumping" Cryogenics **11** (1991) 936-948

Chapter III

Study to Improve the Critical Current Density and Flux Pinning of Bulk MgB_2 Superconductor by Optimized Doping

In this chapter we have discussed the initial work done to improve the flux pinning mechanism and the superconducting properties and also understand the consequent effect on the physical properties (structural, microstructural, and magnetic) of the optimized doped bulk MgB_2 superconductor samples. The objective of the present work is to:

a) Introduce flux pinning centers into the matrix bulk MgB_2 via additions of different additives which corresponds to increment in the superconducting J_c.
b) The presence of nano meter-sized secondary particles which may result to high flux pinning and improved mechanical performance.
c) To be able to reduce the production cost of MgB_2 superconductor without compromising the performance and to develop a reliable manufacturing process for large scale production.
d) Comparative study and examination of the results and draw correlations, if any, between microstructural and magnetic properties measured.

3.1. Introduction:

MgB_2 superconducting bulk superconducting materials and are relatively simple to make and are available at a reasonable cost. The performance specifications also make them of interest for a number of applications as mentioned in general introductions of this work. Numerous successful efforts in MgB_2 bulk development have been studied [1-5, 6-7, 8-9]. In order to further improve the field performance of bulk MgB_2, we tried to apply chemical doping on bulk MgB_2.

In this chapter we focus on studying the influence of carbon (C) doping (Nano-diamond and charcoal) and also silver (Ag) addition on superconducting performance in bulk MgB_2 samples and use the finding to improve the efficiency of the various dopants or additives. The superconducting $J_{c,s}$ with various C and Ag concentrations were studied and compared. The property optimization of the MgB_2 bulk samples consisted of variation of doping concentration, even though the heat treatment parameters were maintained for the entire samples produced in this chapter as discussed in the sample preparation section in previous chapter of this work (section 2.1.1). The flux pinning performance in the undoped, C-doped and Ag doped bulk MgB_2 was studied for the three different approaches and the superconducting $J_{c,s}$ of these samples were calculated from their respective *M-H* loops and compared. Finally, the overall doping by additives in the whole set of bulk MgB_2

samples was investigated in terms of the superconducting properties, doping techniques, microstructure and changes in lattice parameters.

3.2 Nano-diamond Doping:

Earlier studies indicated that an inclusion of nano-dopants enables control of MgB_2 microstructure by introducing nano-pinning centers into the superconducting matrix. Nanoscale diamond powder makes it possible to form a high density of nano-inclusions in MgB_2 matrix. To improve pinning performance of bulk MgB_2 materials, we tried to utilize a nanoscopic diamond powder in combination with optimum sintering temperature set in earlier studies [6]. In this section, we study the effect a nanoscopic diamond powder on bulk MgB_2 material by means of X-ray diffraction (XRD), superconducting transition temperature, microstructural analysis and critical current density at 20 K.

3.2.1 Structural Characterization

The XRD diffraction patterns shown in Figure 3.1 give information on the crystallographic phases at different doping levels. All three bulk MgB_2-nD samples consisted mainly of MgB_2 phase and a small quantity of MgO phase. From previous research, we know that the nanoscale diamond should be reflected as an impurity phase in the MgB_2 material, with intensity depending on the initially added weight percentage of the nanoscale diamond. However, the main reflection of the nano-diamond (111) could not be seen in the XRD patterns due to an overlap with the MgB_2 (101) peak. Therefore, we were able to observe only MgO impurity by XRD, similar to our earlier reports [7-8]. In the present work we could not see any new impurity phase formation.

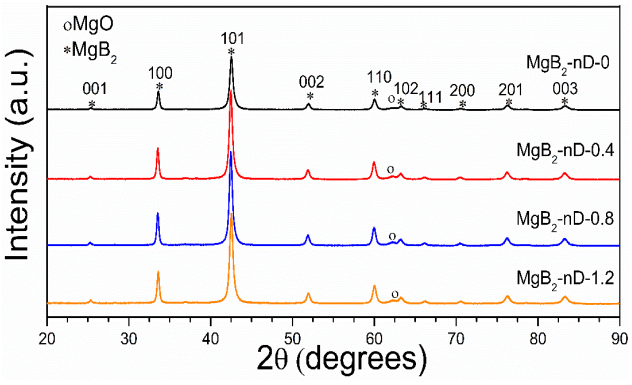

Figure 3.1: X-ray diffraction patterns of bulk MgB_2-diamond nanocomposites produced using the mixture of the amorphous boron powders in sintering process. All samples are sintered at 775 °C for 3h in argon atmosphere.

3.2.2 Superconducting Performance

3.2.2.1 Temperature dependence of DC susceptibility

Temperature dependence of magnetization curves was measured on the MgB_2 samples with a varying content of nano-diamond powder in a magnetic field of 1 mT. The critical temperature ($T_{c,onset}$) decreased with increasing nanoscale diamond content as shown in Figure 3.2. Note that a high T_c (onset) of 37.8 K was observed for a sample produced without nano-diamond. Here we obtained T_c (onset) around 37.3 K for 1.2 wt% of nano-diamond. This clearly indicates that there's need to find an optimum between T_c degradation and pinning enhancement.

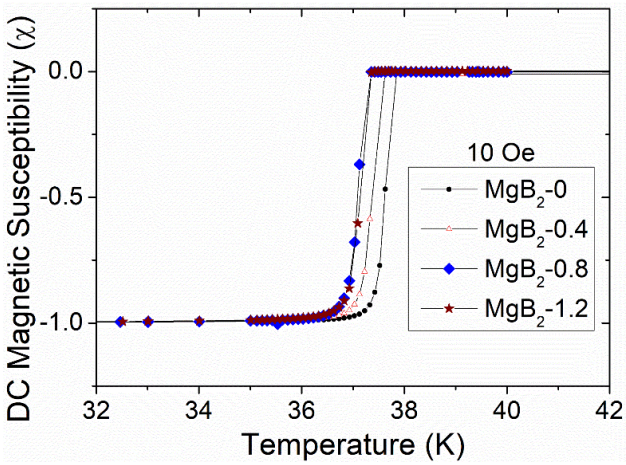

Figure 3.2 Superconducting transition in the bulk MgB_2-diamond nanocomposites produced using the mixture of the amorphous boron powders in sintering process.

3.3.2.2 Field dependence of critical current densities

To see the effect of nano-diamond addition on critical current density, J_c was determined from magnetization hysteresis loops (*M-H* loops) by utilizing the Bean critical state model [20]. The magnetic property measurement is detected by a SQUID magnetometer in applied magnetic fields from –1 to +5 T at 20 K. Figure 3.4 shows J_c values at 20 K as a function of applied magnetic field for the bulk MgB_2 material with varying content of nano-diamond. The MgB_2 sample with 0.8 wt% of nano-diamond powder exhibited higher critical current density than a pure MgB_2 material as well as the 0.4 wt% and 1.2 wt% samples. J_c increment at higher field has improved for the doped samples as shown on the graph [see Figure 3.3] which also supports the fact that the flux pinning mechanism has been enhanced through controlled nanodiamond doping. The self-field critical current density around 300 kA/cm^2 was observed at 20K for the best sample as compared to the J_c of 278 kA/cm^2 for the pure sample. We can say that optimization was effective for the 0.8wt% nanodiamond added sample. The critical current density in high magnetic fields also improved. In the MgB_2 sample with 1.2 wt% and 0.4 wt% of nano-diamond powder, the critical current density decreased by a small value when compared with the pure sample. Thus, performance of the bulk MgB_2 material can be improved

by optimizing the amount of nano-diamond powder in bulk MgB_2 material. The present study supports the suggestion that the nanoscale diamond can serve as a strong pinning medium to improve flux pinning of MgB_2 bulks at high magnetic fields.

The elementary pinning force of grain boundaries in MgB_2 is dependent on its nanostructural control. J_c at low field is simply determined by the connectivity, grain size, and elementary pinning force of the grain boundaries. The effects of grain connectivity and grain size on critical current density and flux pinning are analysed. There is qualitative agreement between grain-boundary pinning mechanism and the experimentally observed grain-size dependence of flux pinning in bulk MgB_2 [9].

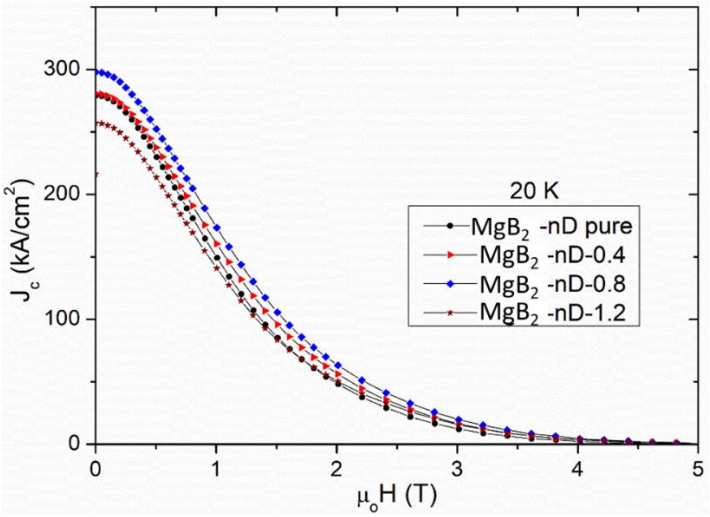

Figure 3.3: The field dependence of the critical current densities for the same material at $T = 20$ K. All samples are sintered at 775 °C for 3h in argon atmosphere.

3.2.3 Analysis of Microstructure

The results of the microstructural analysis in figure 3.4 shows the refined grains and mapping analysis of the optimized diamond added sample and we emphasize that these grains help in enhancing J_c. Although the percentage of the dopant added is low, this grain refinement behavior is in agreement with previous literature [10] [11]. Therefore, the diamond nanoparticles may provide nucleation centers for MgB_2 and tightly bound to them [12]. These intergrain nano sized inclusions created by nanodiamond acts as strong pinning centres and are responsible for the improved flux pinning which are optimally distributed in the 0.8wt%-nD sample.

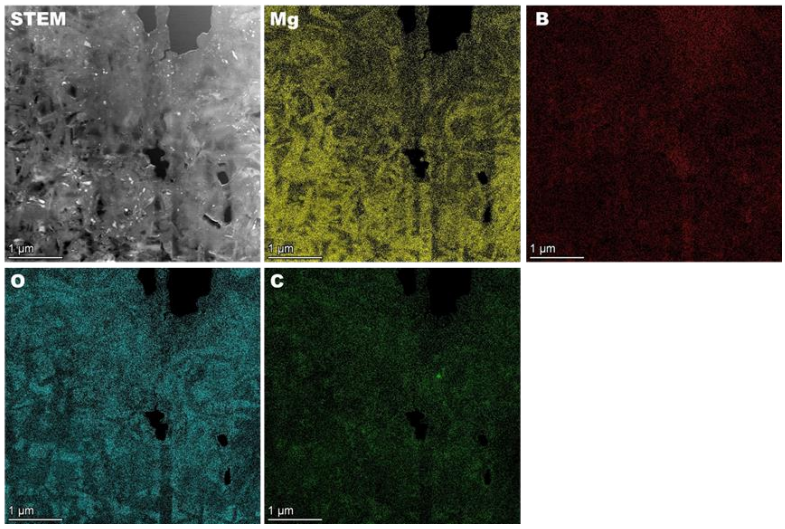

Figure 3.4: TEM Micrograph of optimized diamond-added MgB_2 sample showing mapping analysis of selected elements and uniform distribution of nanodiamond dopant.

3.3 Ag-added MgB_2

In this section, the Ag addition is to improve the mechanical properties in our fabricated MgB_2 samples. This is also supported by claims in literatures to improve properties of superconducting materials such as the fracture toughness and the strength of the bulk which could be due to the ductility of the Ag [12]. We have successfully improved the pinning performance of bulk MgB_2 materials in our previous work by utilizing a nanoscopic diamond powder in combination with optimum sintering temperature [13]. In this section of the chapter, work is done in order to further improve the grain connectivity and improve the flux pinning, we focused on the effect Ag addition on the bulk MgB_2 material. The fabricated bulk was analyzed by means of X-ray diffraction (XRD) technique, superconducting transition temperature and critical current density at 20 K were also determined. There was improvement in the J_c values as compared to our reference samples. The best sample indicated a high critical current density of 389.2 $kAcm^{-2}$ at 20 K and the superconducting transition temperature around 37.5 K.

3.3.1 X-ray Diffraction Analysis

Figure 3.5 shows the XRD patterns of the prepared samples (0 wt%, 3.5 wt%, 4.0 wt% and 4.5 wt% of Ag). The major peaks of all MgB_2 samples are exhibiting hexagonal structure consisting mainly of MgB_2 phase and a small quantity of MgO phase.

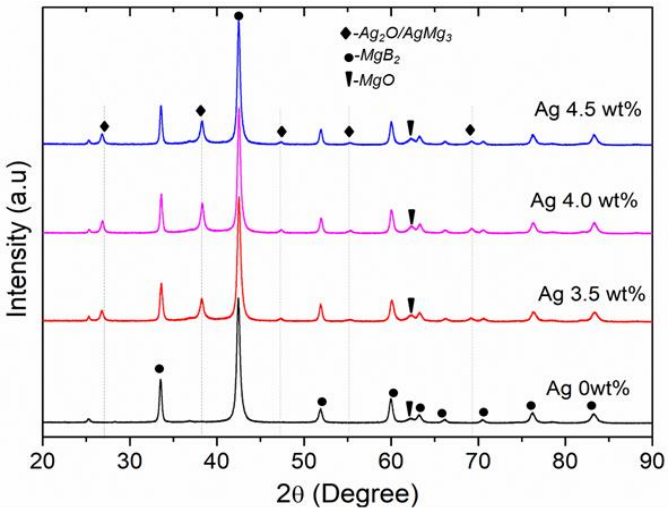

Figure 3.5: X-ray diffraction patterns of bulk MgB_2-nD-Ag produced using the mixture of the amorphous boron powders in sintering process. All samples are sintered at 775 ^oC for 3h in argon atmosphere.

The figure clearly shows additional peaks at the Braggs angles corresponding to 26.27^o, 38.20^o, 42.28^o, 54.90^o, and 68.75^o. The additional peaks at the 2θ corresponding to these Bragg angles were confirmed on the basis of the JSPDF to be close to the $Ag_2O/AgMg_3$ secondary phases. In our previous study, we observed that the peaks are much closer to those of the Ag_2O phase than the $AgMg_3$ phase. The intensity of the Bragg peaks for the secondary phases of $Ag_2O/AgMg_3$ was observed to have increased systematically with corresponding increase in the Ag content in the samples.

We already reported how nanoscale diamond should've reflected as an impurity phase in the MgB_2 material, with intensity depending on the initially added weight percentage of the nanoscale diamond. However, the main reflection of the nano-diamond (111) could not be seen in the XRD patterns due to an overlap with the MgB_2 (101) peak. Therefore, we were able to observe only MgO impurity by XRD, similar to our earlier reports [13].

3.3.2 Superconducting Performance

3.3.2.1 Temperature dependence of DC susceptibility

The DC temperature dependence of magnetization curves was measured on the MgB_2 samples with varying content of Ag powder in a magnetic field of 1 mT. The onset of the critical temperature ($T_{c,onset}$) didn't show much effect with increasing Ag content (see Figure 3.6). Note that a high T_c (onset) of 38.2 K was observed for a sample produced without Ag and ~37.5 K for 4.0 wt% of Ag sample which indicates that we have to find an optimum between superconductivity degradation and pinning enhancement. The superconducting transition width (ΔT_c) of all produced samples exhibiting ≤ 1 K indicating sharp superconducting transitions of the sintered MgB_2 samples and of superior quality and good crystallinity. This data is supported by the literature [14] which showed that the Ag

addition does not deteriorate the superconducting properties of the bulk MgB_2 materials.

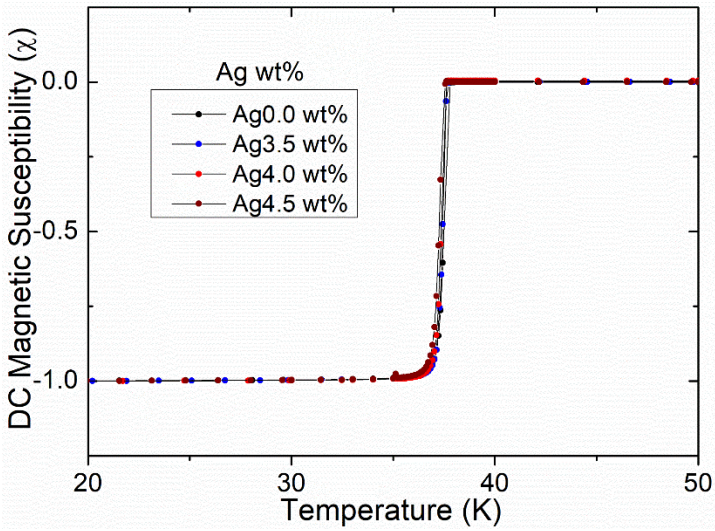

Figure 3.6 Superconducting transition in the bulk Ag added MgB_2-nD

3.3.2.2 Field dependence of critical current densities

The effect of Ag addition on critical current density, J_c was determined from magnetization hysteresis loops (*M-H* loops) detected by a SQUID magnetometer in applied magnetic fields from 0 to 5 T at 20 K. Figure. 3.7 shows J_c values at 20 K as a function of applied magnetic field for the bulk MgB_2 material with varying content of Ag powder. The self-field J_c of Ag 0 wt.%, Ag 3.5 wt.%, Ag 4 wt.%, and Ag 4.5 wt.% samples are determined to be 298 kA/cm^2, 347 kA/cm^2, 389 kA/cm^2 and 364.7 kA/cm^2 respectively. The MgB_2 sample with 4.0 wt% of Ag exhibited higher critical current density than a pure MgB_2 material as well as the 3.5 wt% and 4.5 wt% samples. J_c increment at higher field has improved for the doped samples as shown on the graph (see Fig. 3.7), which also supports the fact that the flux pinning mechanism has been enhanced through controlled Ag doping. The self-field critical current density around 389 kA/cm^2 was observed at 20 K for the best sample as compared to the J_c of 298 kA/cm^2 for the Ag-free sample. We can say that optimization was effective for the 4.0 wt.% Ag added sample. Thus, performance of the bulk MgB_2 material can be improved by optimizing the amount of Ag powder in bulk MgB_2 material. The present study supports the suggestion that the Ag can serve as a strong pinning medium to improve flux pinning of MgB_2 bulks.

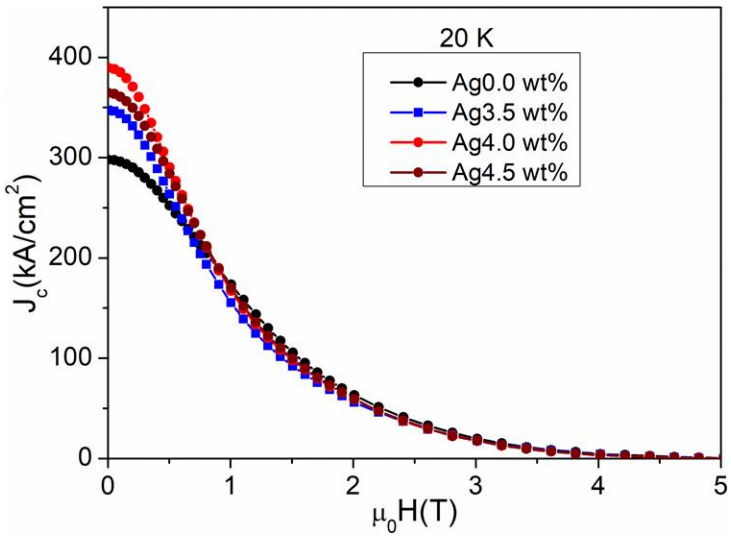

Figure 3.7: The Critical current densities as function of the applied fields for Ag added MgB_2 at T = 20 K.

3.3.3 Flux Pinning Analysis

With reference to the high connectivity mechanism in the single vortex region which are known to be caused by mostly defects, distortions of the lattice and grain boundaries are thought to be strong centers of pinning. The J_c remains high in the small bundle region with a strong flux pinning force ($F_p = J_c*B$). The F_p field dependence is proportional to $h^n(1-h)^m$, with $h=H/H_{irr}$, and the n and m values depend on the different flux pinning mechanisms [15][17][20]. Figure 3.8 shows the h dependency on the normalized flux pinning force with its maximum "$F_p/F_{p,max}$". The $F_p/F_{p,max}$ for the 4.0 wt% sample is most effective in the vortex region and in the small bundle area. The obtained magnetization data were calculated and modeled into a pinning force analysis as indicated on Figure 3.8. According to Dew-Hughes [20], the peak position of the $f_p(h)$ dependence indicates the type of pinning in the superconducting material. As per the model, peak position in f_p vs. h at 0.2 implies grain boundary pinning, meanwhile 0.33 implies core, δT_c pinning, and so on. This flux pinning behavior was also supported by the works of Koblischka et al. [21]. Here, the effect of the Ag addition as regards the flux pinning behavior of the bulk samples around 0.18 could be mostly attributed to the grain boundary kind of pinning mechanism.

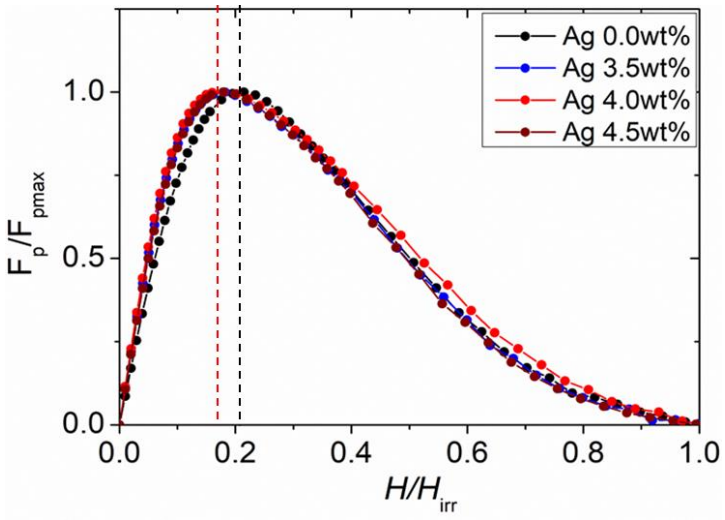

Figure 3.8: Scaling of the volume pinning force ($F_p/F_{p,max}$) versus $h=H/H_{irr}$ for Ag-doped

3.3.4 Analysis of Microstructure

The pinning force of the grain boundaries in MgB_2 is dependent on its nanostructural control [13]. The J_c at low field is known to be determined by the grain connectivity, grain size, and elementary pinning force of the grain boundaries. The effects of grain connectivity and grain size on critical current density and flux pinning are analyzed.

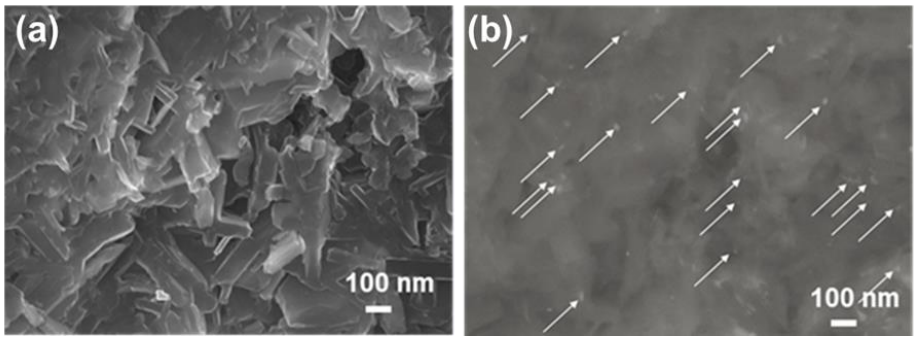

Figure 3.9: (a) High magnification SEM images of fractured cross section for the bulk Ag4.0 wt% MgB_2 sample (b) Compound image indicating some bright particles of $AgMg_3$ embedded in the matrix.

There is qualitative agreement between grain-boundary pinning mechanism and the experimentally observed grain-size dependence of flux pinning in bulk MgB_2 [16]. The normalized pinning force obtained from the resulting J_c's revealed a good scaling as introduced by Dew-Hughes (DH) [20]. The range of the peak positions is between 0.183 and 0.242, which reveals that all samples showed the δl pinning [15].

In order to understand more about the enhanced J_c performance of the improved sample, the results of the microstructural analysis show the reflection of the silver particles trapped in the voids

of the MgB_2 grains. This was also observed in the 3.5 wt% and 4.5 wt% samples, however, the uniformity of the dispersed particles in the 4.0 wt% doped sample and also the inclusions in form of silver-based nanometer –sized secondary phase particles in these grains help in enhancing J_c, this analysis is partly supported by our previous work on nanodiamond doping [13]. The $AgMg_3$ secondary phase particles in the Ag doped sample microstructure is pointed by the arrows as shown in Fig. 3.9(b). This further implies that the Ag addition is effective in enhancing the flux pinning properties for MgB_2. These intergrain nano sized inclusions created by Ag addition acts as strong pinning centres and are responsible for the improved flux pinning which are optimally distributed in the Ag-4.0 wt% sample.

3.4 Charcoal Addition on MgB_2

In to reduce the cost of production one must look for the naturally available forms of carbon sources. To improve the flux pinning performance of bulk MgB_2 materials, we tried to utilize other forms of carbon sources such as activated charcoal in combination with optimum sintering temperature set in earlier studies [6]. Due to its low cost, we have selected charcoal as a carbon source for synthesizing bulk MgB_2. the charcoal powder was sieved and ball milled for 2 hours down to from less than 40 to 60 nm particle size as analyzed using particle size analyzer (BECKMAN COULTER/DelsaMax PRO). In figure 3.10, the obtained size distribution shows particles are distributed mainly in the range of 45 to 65 nm. The charcoal powder of different sizes was prepared to understand the size effect of charcoal on the doping properties, the variation of T_c, triggering of different phases and J_c. The best sample indicated a high critical current density around 467 $kAcm^{-2}$ at 20 K and the superconducting transition temperature around 37.5 K.

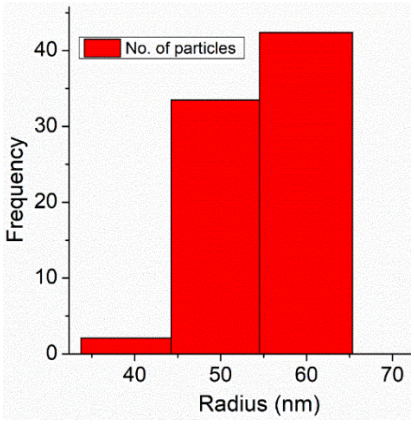

Figure 3.10: Charcoal particles size histograms as obtained from particle size analyzer after sieving and ball milling

3.4.1 XRD Analysis

Figure 3.11 shows the XRD patterns of all synthesized MgB_2 samples, which gives the information on the crystallographic phases at different levels of doping. All the major Bragg peaks of MgB_2 hexagonal structure can be identified, indicating that samples mainly consist of the MgB_2 phase with small amount of MgO. The formation of MgO could not be completely prevented due to high reactivity of magnesium with oxygen, we were able to observe only MgO impurity by XRD, similar to our earlier reports [13].

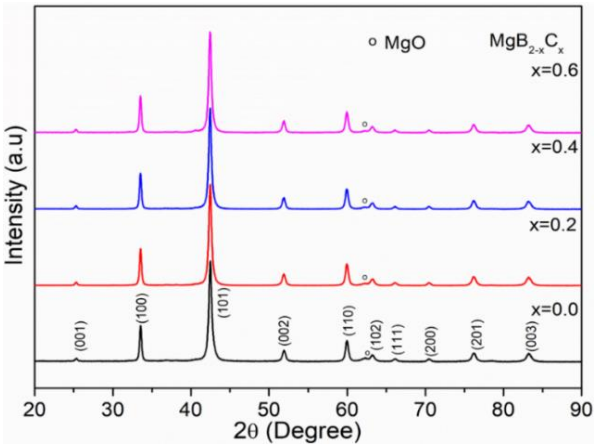

Figure 3.11: X-ray diffraction patterns of charcoal added MgB_2 bulk samples produced using the mixture of the nano boron powders and different charcoal contents in sintering process.

3.4.2 Superconducting Performance

3.4.2.1 Temperature dependence of DC susceptibility

The magnetic susceptibility curves were measured on the MgB_2 samples with a varying content of the charcoal powder in a magnetic field of 1 mT. There was a small decrease in the critical temperature ($T_{c,onset}$) with increasing charcoal content (see Figure 3.12). A high ($T_{c,onset}$) of 38.45 K was observed for the charcoal-free sample and obtained the ($T_{c,onset}$) around 37.8 K, 37.6 K and 37.4 K for 0.2 wt% 0.4 wt% and 0.6wt% of charcoal respectively.

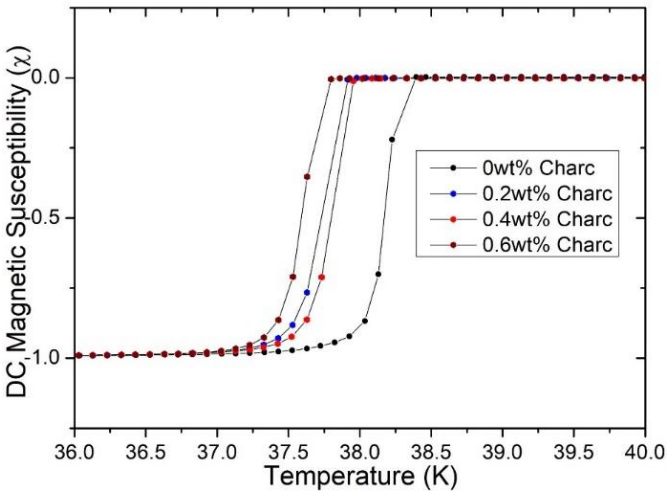

Figure. 3.12: Superconducting transition in the bulk MgB_2-diamond nanocomposites produced in sintering temperature at 775 °C for 3h in argon atmosphere.

The temperature dependence of magnetization curves indicated that the onset of T_c for the doped samples are around 1 K lower than that of the undoped bulk MgB_2. In a typical carbon doped MgB_2, the T_c is known to be dependent on the amount of carbon substitution into the boron sites which means that the more carbon substitution corresponds to a lower T_c [14] [15] [16]. We can emphasize that a substantial amount of carbon diffuses more effectively into the MgB_2 lattice to substitute into the boron when a smaller size charcoal powder was used.

3.4.2.2 Field dependence of critical current densities

The variation of the critical current density (J_c) at 20 K as the function of the applied magnetic field was analyzed to investigate the effect of charcoal addition. Figure 5.4 shows the J_c curves at 20 K as a function of applied magnetic field for the bulk MgB_2 material with varying content of charcoal powder. The self-field J_c values of 0, 0.2, 0.4 and 0.6 wt.% charcoal added MgB_2 samples are 280, 366, 467 and 341 kA/cm^2 respectively. The self-field critical current density around 467 kA/cm^2 was observed at 20K for the bulk MgB_2 with 0.4wt% of charcoal as compared to the J_c of 280 kA/cm^2 for the undoped material. MgB_2 sample with 0.4 wt% of charcoal powder showed higher critical current density than the charcoal-free MgB_2 as well as the other variables indicating the optimal composition among the present series. If the J_c values are compared at 1 T applied field for 0, 0.2, 0.4 and 0.6 wt.% charcoal added MgB_2 samples are 164, 201, 280 and 183 kA/cm^2 respectively. We can say that optimization was effective for the 0.4wt% charcoal added sample. The present result indicate that the nanoscale charcoal can serve as a strong pinning medium to improve flux pinning of MgB_2 bulks at high magnetic fields.

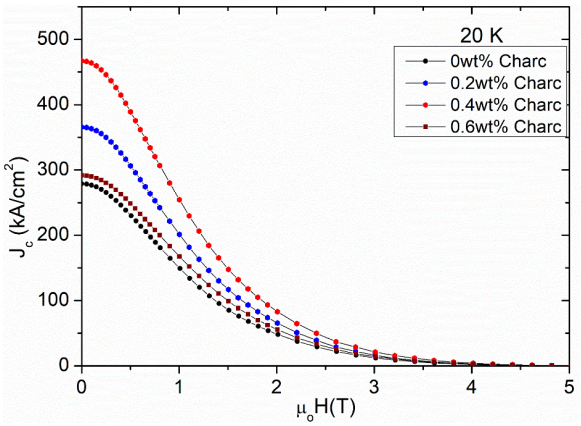

Figure 3.13: The field dependence of the critical current densities for the charcoal added MgB_2 material at T = 20 K. All samples are sintered at 775 ^oC for 3h in argon atmosphere.

3.5 Uniformity and Flux Pinning of Optimized Doped Bulk MgB_2

From our discussions in the previous sections of this chapter, we may agree that optimization was obtained for the different doping techniques. We also try to show the level of homogeneity obtained for the respective doping processes in this session. To confirm that, we further analyzed the superconducting $J_{c,s}$ at different positions of all the optimized samples by cutting through the smaller cross-sections at different regions of the respective doped bulks discussed. Figure 3.14 shows the schematic diagram to demonstrate how we take out our representative samples for SQUID measurements from all the optimally doped samples.

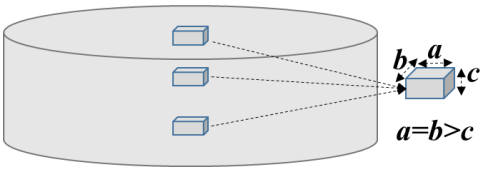

Figure 3.14: Schematic diagram of the MgB_2 bulk showing representative sample cut-off from top, middle and bottom of the bulk.

In order to demonstrate uniformity across the doped bulk samples obtained from each doping process. All cut sections of the samples conform to the illustration shown in figure 3.14. SQUID measurements were taken and the corresponding $J_{c,s}$ of each doping process were obtained and shown in figure 3.15. here we can be able to ascertain the degree of uniformity in each process.

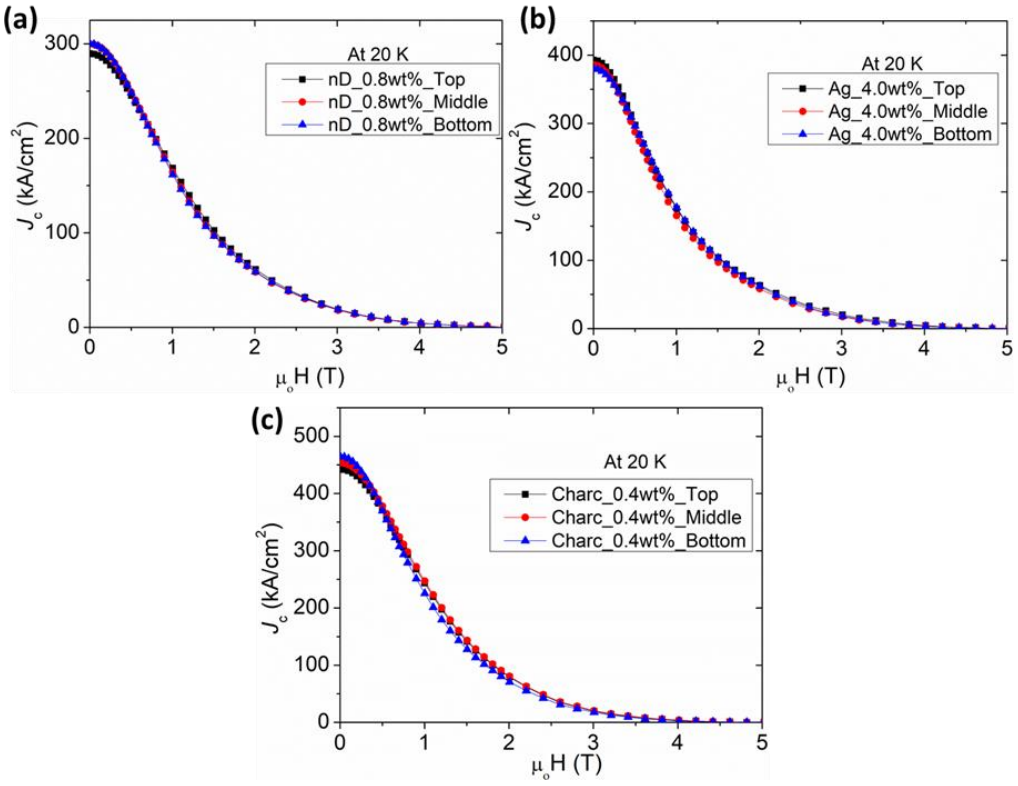

Figure 3.15: Uniformity of $J_{c,s}$ in optimized bulk samples (a)Nanodiamond doped (b)Ag doped (c)Charc doped

The fabrication technique involved in all three different doping is the same, hence could also be more reason to obtain homogeneity in a likely manner. In all three cases, we realized the differences in the $J_{c,s}$ in each samples are within 5 to 10 kA/cm^2 range which is negligibly reasonable to claim that our bulk samples are uniform. A lot researches and development going on to be able to utilize the MgB_2 bulk materials for practical applications [19] which opens up more ways to several approaches to enhance the performance of the bulk superconductor.

In a likely manner to the analysis of flux pinning for Ag-doped samples, the flux pinning of the optimized doped samples from different sources of carbon utilized in this chapter, nano-diamond and charcoal. Figure. 3.16 shows the h dependency on the normalized flux pinning force with the peak positions at "$F_p/F_{p,max}$". The $F_p/F_{p,max}$ for the charcoal doped wt% sample shows a slight shift to the right. These results correspond to the behavior of J_c obtained for respective samples in figures 3.3 and 3.13. The obtained magnetization data were calculated and modeled into a pinning force analysis as indicated on Fig. 3.16. peak positions for nano-diamond doped and charcoal doped samples were around 0.20 and 0.24 respectively.

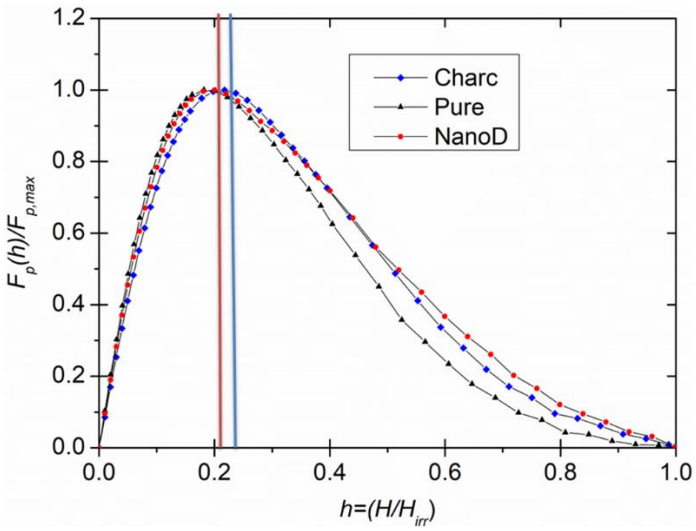

Figure 3.16: Scaling of the volume pinning force for nano-diamond and charcoal doped samples

As earlier explained according to Dew-Hughes, the peak position of the $f_p(h)$ dependence indicates the type of pinning in the superconducting material. 0.2 implies grain boundary pinning, meanwhile 0.33 implies core, δT_c pinning, and so on. The resulting peak positions, h_o, for the optimized doped samples show a slight shift to the right towards higher field ~ 0.24 for the charcoal doped which could also be the indication for other possible particle pinning.

References:

[1] K. Vinod, R G Abhilash Kumar, U. Syamaprasad, "Prospects for MgB_2 superconductors for magnet application" *Supercond. Sci. Technol.* **20** (2007) R1

[2] M. Muralidhar, K. Nozaki, H. Kobayashi, X.L. Zeng, A. Koblischka-Veneva, M.R. Koblischka, K. Inoue, M. Murakami, "Optimization of sintering conditions in bulk MgB_2 material for improvement of critical current density" J. of Alloys and Compounds **649** (2015) 833-842

[3] S.X. Dou, S. Soltanian, J. Horvat, X.L. Wang, S.H. Zhou, M. Ionescu, H.K. Liu, P. Munroe, M. Tomsic, "Enhancement of the critical current density and flux pinning of MgB_2 superconductor by nanoparticle SiC doping" Appl. Phys. Lett., **81** (2002) 3419-3421

[4] J.H. Kim, S. Zhou, M.S.A. Hossain, A.V. Pan, S.X. Dou, "Carbohydrate doping to enhance electromagnetic properties of MgB_2 superconductors" Appl. Phys. Lett., **89** (2006) 142505-142507

[5] J.G. Noudem, M. Aburras, P. Bernstein, X. Chaud, M. Muralidhar, M. Murakami, "Development in processing of MgB_2 cryo-magnet superconductors" J. Appl. Phys., **116** (2014) 4

[6] A. Vajpayee, R. Jha, A.K. Srivastava, H. Kishan, M. Tropeano, C. Ferdeghini, V.P.S. Awana, "The effect of synthesis temperature on the superconducting properties of n-SiC added bulk MgB_2 superconductor" Supercond. Sci. Technol., **24** (2011) 11

[7] T. Naito, T. Sasaki, H. Fujishiro, "Trapped magnetic field and vortex pinning properties of MgB_2 superconducting bulk fabricated by a capsule method" Supercond. Sci. Technol., **25** (2012) 6

[8] M. Muralidhar, N. Kenta, M.R Koblischka, M. Murakami, "High Critical Current Density in MgB_2 Fabricated Using Amorphous Boron" Physica Status Solidi A **212**, (2015) 2141.

[9] E. Martínez, P. Mikheenko, M. Martínez-López, A. Millán, A. Bevan, and J. S. Abell, "Flux pinning force in bulk MgB_2 with variable grain size" Phys. Rev. B 75, (2007) 134515

[10] C H Cheng, Y Yang, P Munroe, and Y Zhao, "Comparison between nano-diamond and carbon nanotube doping effects on critical current density and flux pinning in MgB_2" Supercond. Sci. Technol. **20 (**2006) 296-301

[11] A. Gupta and A V Narlikar, "Pinning and irreversibility in superconducting bulk MgB_2 with added nanodiamonds" Supercond. Sci. Technol. **22 (**2009) 125029

[12] W. Alex, K. Michael, I. Kazuo, M. Muralidhar, B. Kevin, D. Bruno, H. Thomas, M. Murakami, and H Uwe, [Superconductivity: Applications Today and Tomorrow], Nova Science Publishers, Inc, (2016) 269-277.

[13] J.D Longji., M. Muralidhar, M. Murakami, "Flux pinning and superconducting properties of MgB_2-diamond nanocomposite" J. Phys. Conf. Ser. **1054** (2018) 012052.

[14] Y. Zhao, X.F. Rui, C.H. Cheng, H. Zhang, P. Munroe, H.M. Zeng, N. Koshizuka, M. Murakami, "Doping effect of nano-diamond on superconductivity and flux pinning in MgB_2" *Supercond. Sci. Technol*. **16 (**2003) 10

[15] C H Cheng, Y Yang, P Munroe, and Y Zhao, "Comparison between nano-diamond and carbon nanotube doping effects on critical current density and flux pinning in MgB_2" *Supercond. Sci. Technol*. **20** (2006) 296

[16] A. Gupta and A V Narlikar, "Anurag Gupta and A V Narlikar 2009 *Supercond. Sci. Technol*. **22** 125029" *Supercond. Sci. Technol*. **22 (**2009**)** 125029

[17] D Kumar, S J Pennycook, J Narayan, H Wang and A Tiwari, "Role of silver addition in the synthesis of high critical current density MgB_2 bulk superconductors" *Supercond. Sci. Technol*. **16** (2003) 455–458

[18] M. Muralidhar, M. R. Koblischka, M. Tomiata, "Critical current densities in Ag-added bulk MgB_2" *(A. Medez-Vilas, Ed)*,5, (2012) 1468-1479

[19] M. Tomsic, M. Rindfleisch, J. Yue, K. McFadden, and J. Phillips, "Overview of MgB_2 superconductor applications" *Int. J. Appl. Ceram. Technol.,* **4** (2007) 250–259

[20] D. Dew Hughes, "Flux Pinning Mechanisms in Type-II Superconductors" Phil. Mag. **30 (**1974**)** 293

[21] M.R Koblischka, and M. Muralidhar**,** "Pinning force scaling analysis of Fe-based high-T_c superconductors" Inter. J. Mod. Phys. B**, 30**, (2016) 1630017

Chapter IV

Optimization of Sintering Conditions for Synthesizing Dense Bulk MgB_2 Superconductor via In-situ and Ex-situ Spark Plasma Sintering Method

In this chapter, high density MgB_2 bulk superconductors were synthesized by SPS under pressure to improve the field dependence of critical current density (J_c-B). This chapter investigated the relationship between sintering conditions (temperature and time) and J_c-B using two methods, *ex-situ* and *in-situ* respectively. Our aim in this chapter is to:

a) achieve higher density with suppressed particle growth and suppression of the formation of coarse particles of MgB_4 and MgO which is key to being effective in improving the J_c-B characteristics.
b) Control the degradation of MgB_2 due to pyrolysis at severe temperatures by controlling the heat rate and dwell times. This is also aim at achieving higher density and less impurity phase in the bulk samples, which will improve the J_c-B properties.
c) In addition, structural characterization and flux pinning (f_P) analysis should reveal the microstructural control of refined MgO inclusions and MgB_4 phase as new pinning centres which greatly contributed to the J_c-B properties. The contributions of the sintering conditions on f_P for both synthesis methods will be analyzed.

4.1 Introduction:

In accordance with the previous chapters, it has become a common knowledge that intermetallic MgB_2 with a hexagonal structure has been studied several decades ago since 1953 [1] and still under study due to its promising prospects. We've also discussed in previous chapter, its superconducting critical temperature (T_c) up to 39 K which was observed in 2001 due to the presence of two distinct superconducting gaps. [2] The inexpensive cost, strong mechanical properties [3,4] and long coherence length of this material make it ideal for a variety of applications. [5] It has a greater upper critical field than standard NbTi and Nb_3Sn superconductors. This section also emphasizes on the fewer anisotropic effects and no weak links as compared to superconducting cuprates. The grain boundaries do not act as weak links that inhibits superconducting current, therefore this makes it possible to fabricate superconducting bulk and wires in crystalline forms [5,6]. In the literature [6,7], we can find reports of research on this topic of the effects of the SPS temperature on the mechanical properties of the MgB_2 bulk superconductor was investigated through bending tests of specimens cut from the bulk samples. Both Young's modulus and bending strength were improved by the increase in the SPS temperature [8]. For better practical application, together with the superconducting

properties of MgB_2, the critical current density (J_c) is important, improving their mechanical properties [9]. However, since MgB_2 is polycrystalline in nature, most techniques for producing this material involve low relative densities that have poor material performance [10]. There is a solid relationship between the super-current conduction region and the material density, the resulting effect of which is constantly reflected in J_c [11,12]. Three different advances are used for the production of MgB_2 wires and bulk samples, hence: the *ex-situ* technique [9,13,14], in-situ [9,14-17] and the Mg Internal Diffusion (IMD) technique [18]. Gajda et al. [8,9] studied the fabrication of MgB_2 wire by hot isostatic pressure (HIP) and the influence of various physicochemical parameters on their superconducting properties. By applying SPS to fabricate sintered polycrystalline MgB_2 bulks in our research, the bulk superconducting performance have been studied in relation to our starting powders and techniques. The approach to target the J_c of the samples by enhancing it as a result of the controlled microstructure and improved density and flux pinning achieved by optimizing the sintering temperature conditions by both *in-situ* and *ex-situ* SPS processing with reduced deterioration of the MgB_2 phase. The SPS process, can be used to obtain full density without grain growth at a high heating rate (up to 600 °C/min or more) and a short holding time, usually a few minutes. SPS process obtain fully dense samples at relatively low sintering temperatures, usually several hundred degrees lower than in the case of normal hot pressing [19]. However, there are difficulties with this method. Several authors have reported about the problem of MgB_2 decomposition during the densification at high temperatures while sintering via *ex-situ* methods [20-22]. The MgB_2 bulk samples produced via SPS method contains nano sized MgO and higher borides (of compositions near MgB_4, MgB_7, MgB_{12}, MgB_{17}, MgB_{20}), as inclusions which can be pinning centers. The quantity of secondary phase inclusions is intensified at temperatures above 900 °C, especially when ground powder (*ex-situ*) is used. Guo et al. [23] conducted thermo-analytical studies, in which they found the onset of oxidation at 600 °C and decomposition to higher borides at 930 °C. An additional positive aspect of the SPS is its flexibility in controlling current and temperature, which is an advantage in the successive heating and cooling rates. In the first place, it was expected that this would provide good control of grain growth and, to some extent, evaporation of Mg. For MgB_2, a higher density of grain boundaries associated with a nano-structured material is desired for improved interfacial defect density and hence the superior flux pinning [24].

The research conducted so far has focused on the effect of the addition of nanoscopic diamond particles [25], silver [26] and rare earth particles [27] for improving the J_c of polycrystalline MgB_2. The optimal amount of nano-scale addition of diamond and Ag to MgB_2 enables the formation of high-density nano-inclusions in the MgB_2 matrix and dramatically improves J_c. In the current chapter, we investigated the properties of high-density MgB_2 superconductors prepared using the in-situ and

ex-situ SPS technique. The phase and microstructure of the samples were determined by X-ray diffraction (XRD) and field-emission scanning electron microscopy (FE-SEM). Recent reports have shown the role of sintering kinetics and precursor powders on improving flux pinning and $J_{c,s}$ [28]. Besides the advantage of the T_c which is around 39 K as discussed earlier, the most important property to improve is the J_c and the upper critical fields H_{c2}. In order to achieve this, it is important to improve the pinning force and the connectivity between particles by improving the density of the MgB_2 bulk material. The explanation for our results also resides in the reduction of the cost of the application and processing time, we tried to synthesize the bulk MgB_2 samples via both *ex-situ* and *in-situ* SPS method by using MgB_2 powder and mixing the stoichiometry ratios of Mg and B respectively. This also aimed at fabrication of the bulk with abundant amounts of the grain-connectivity along with high mass density due to the respective reactions which could support even larger J_{cs} in the MgB_2 bulk samples in both cases. The purpose of our study is to clarify the necessary conditions for high J_c using the SPS process. Here, we investigated the effects of the fabrication conditions on the crystal phase, microstructure, J_c and flux pinning of the high density bulk in both SPS *in-situ* and *ex-situ* processes, clarified the differences in the SPS processes, and investigated the method for optimizing each fabrication condition to achieve high J_c.

In this chapter, we have focused on the production of MgB_2 by spark plasma synthesis (SPS) and physico-chemical, magnetic and superconducting properties analysis. We emphasize that the SPS is a promising way to produce dense samples with improved grain bonding and better MgB_2 superconductor bulk densities, which could be an important variant in magnetic applications, therefore we have dealt with this method in our work. The optimization of several parameters such as dwell time, applied pressure, controlled heat and current application rates can effectively improve the immobilization of the stream and hence the efficiency of J_c, as discussed in this manuscript. A comparative study would enable us understand more on the effectiveness of our approach on both the *ex-situ* and *in-situ* processing techniques.

4.2 Synthesis and Characterization via Ex-Situ Process

We have explained the SPS process in chapter II, common features are attributed to its high flexibility allowing high heating and cooling rates and it provides an excellent control of the processing parameters. Despite this, the synthesis of MgB_2 bulks by this method has some constraints which were observed on the process of fabrication of the MgB_2 superconductor. The most common reasons are related to the decomposition of the MgB_2 into secondary phases of higher borides at higher sintering temperatures, the temperature behavior and the saturation point of the MgB_2 bulks during SPS process, grain growth becomes prominent after saturation, the samples produced are

obviously brittle and hard which makes it a bit challenging to fracture for the purpose of characterization, and the complexity of controlling the entire processes taking place during sintering which also depends on the specifics of the technology.

In the process of trying to stabilize the phase of our MgB_2 bulk in the process of fabrication, several trials were attempted which includes variation of the current application. This was difficult to control owing to the reason that the current may highly be dependent on the SPS machine property. However, occurrence of MgO impurity phases and decompositions to higher borides of MgB_4, and/or MgB_7 are common and proved difficult to control. Figure 4.1 shows the nature of the phases obtained by current application at the rate of ~70A/min for 4~5mins dwell time. Since we tend to observe a little bit of more stable phase of MgB_2 at around 300A, this led to more trials of the synthesis meanwhile maintaining a longer dwell time around 20min, all in an attempt to stabilize the MgB_2 phase formation without decomposition. The analysis of the phases obtained for top, bottom and mid sections of the obtained bulk in different trials of 300A and 325A respectively is shown in figure 4.2 (a) and (b).

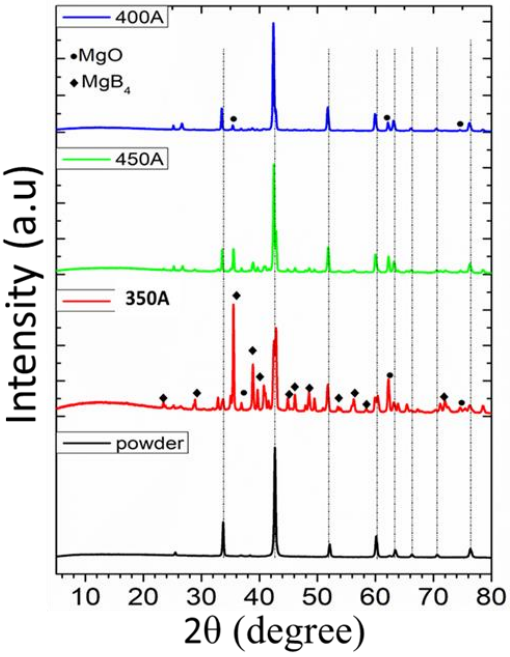

Figure 4.1. X-ray diffraction pattern showing prominent occurrence of secondary phase (MgB_2 powder is used for reference)

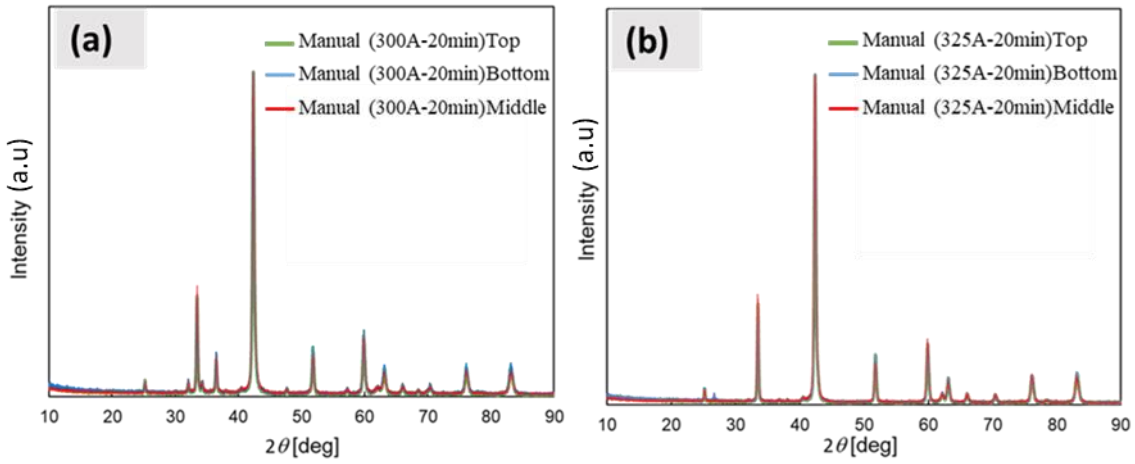

Figure 4.2. XRD analysis of synthesized MgB_2 sample (a) SPS 300A (b) SPS 325A at 20min dwell time

The microstructure observation in figure 4.2 shows the grain growth which is also common to the process. Figure 4.3 (a) is a micrograph of sample obtained by our conventional solid state sintering technique, figures 4.3 (b) and (c) however shows the void elimination but occurrence of grain growth could not be stopped, so with the initial presence of voids being eliminated, it means that there is a need to strike an optimal point between the void elimination and avoidance of grain growth in the process of sintering by SPS. The irregularity in the phase changes with respect to the current application rather made it difficult to systematically obtain data, reason is because we also observed that the decomposition is not uniform with the changes in applied current which also render this initial process unreliable by SPS ex-situ.

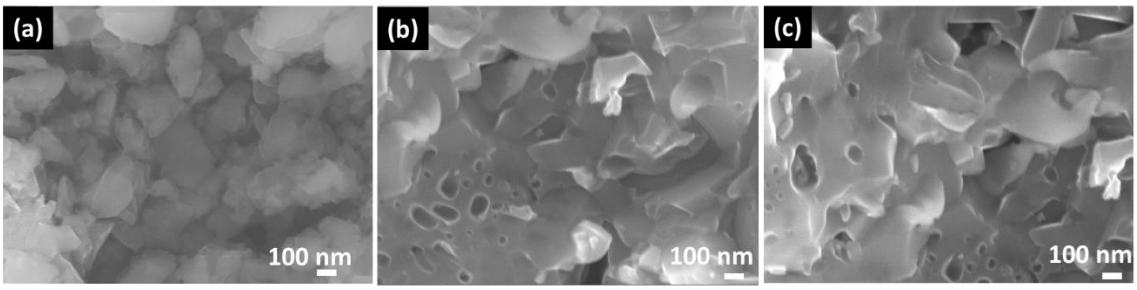

Figure 4.3 SEM micrographs of fractured bulk samples synthesized by (a) solid state sintering at 775 ºC (b) SPS 300A (c) SPS 325A

In order to further control the decomposition and stabilize the MgB_2 phase, the temperature control was adopted at a slighter lesser dwell time of 15min and at a slower applied current of 50A/min. The applied pressure force of 15kN was maintained throughout the fabrication processes. A simple illustration of the sintering regime is shown in figure 4.4. The detailed explanation of the experimental procedure involved in this chapter was explained earlier in the review of literatures and

methodology section. A systematic approach to the temperature and dwell time variation on SPS synthesis of bulk MgB_2 was later discussed in this chapter.

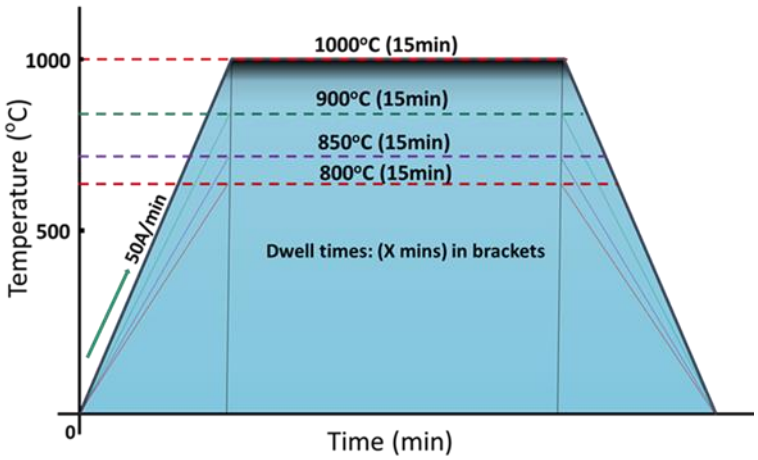

Figure 4.4 Illustration of thermal profile for synthesis by ex-situ

4.3 Phase Analysis for MgB_2 Ex-Situ Process

Considering the systematic approach earlier illustrated in figure 4.4, the XRD patterns for the MgB_2 bulks produced by *ex-situ* sintering at various sintering temperatures from 800 °C - 1000 °C for 15 min are shown in Figure 4.5. The XRD also show little amount of MgO in the starting powder which was included for comparison. The X-ray diffraction patterns of all the samples shows that the highest intensity Bragg peaks representing the MgB_2 phase as major. However, as the sintering temperature increased, the decomposition increased mainly to MgB_4 and MgO as impurity phases. The presence of MgO and MgB_4 impurity phases is not uncommon in MgB_2 processing, and the relatively high contents of the observed impurity phases in these samples are related to the high processing temperatures used [23,24]. Sequel to the updated phase diagram of Mg–B system at high temperature, the Mg vapor is present in equilibrium with MgB_2 or MgB_4 [30]. The observed increase in the contents of MgB_4 and MgO is expected if MgO forms from reaction of the Mg vapor [20]. However, there is the tendency of resolving this issue by improving the quality of the starting powder, hence carrying out powder processing in an inert dry atmosphere, or by possible reduction in the processing temperature [20,21]. The decomposition was observed to intensify when the sintering temperature was increased above 850 °C. But compared to reported literatures [31], the effect of the low-proportions of the formed secondary phase was seen in the improvement of the flux pinning characteristics due to the refinement of the grains which was articulated later in the sample microstructure.

The polycrystalline MgB_2 sample density was determined to be 1.73 g/cm^3 corresponding relative densification value is 66%. The density of the *ex-situ* - 800 °C - 15 min ÷ *ex-situ* - 1000 °C - 15 min

samples was found to be 2.41 g/cm^3 - 2.59 g/cm^3, which corresponds to 92 - 99 % of theoretical density of the same compound. The densification values are given in Table 1. It was observed that as the sintering temperature increased, the relative density values were increased gradually which indicates the decrease of grain-boundary in the bulk samples. SPS bulk samples density is improved about 30%, which imply that the grain connectivity is improved tremendously in the case of SPS MgB_2 bulk samples. The achieved density in the MgB_2 bulk samples is comparable with those reported by literature on the same compound fabricated by SPS and even hot-press [32]. With the present results, we successfully fabricated highly dense MgB_2 bulk samples using SPS technique.

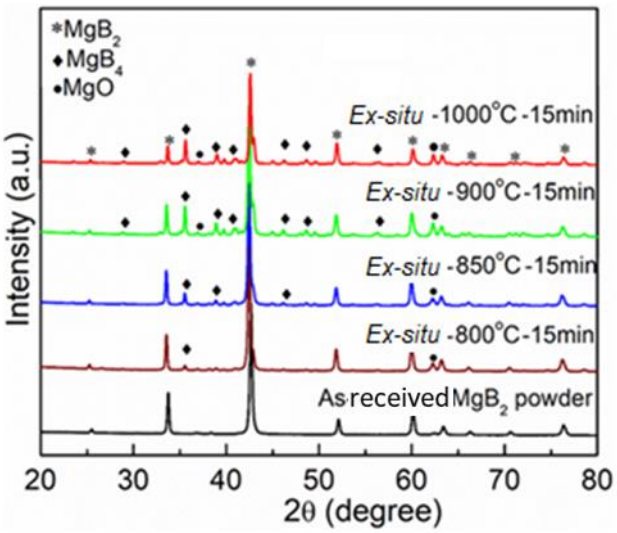

Figure 4.5. X-ray diffraction patterns for sintering temperature optimization of spark plasma sintered MgB_2 bulk via *ex-situ* method.

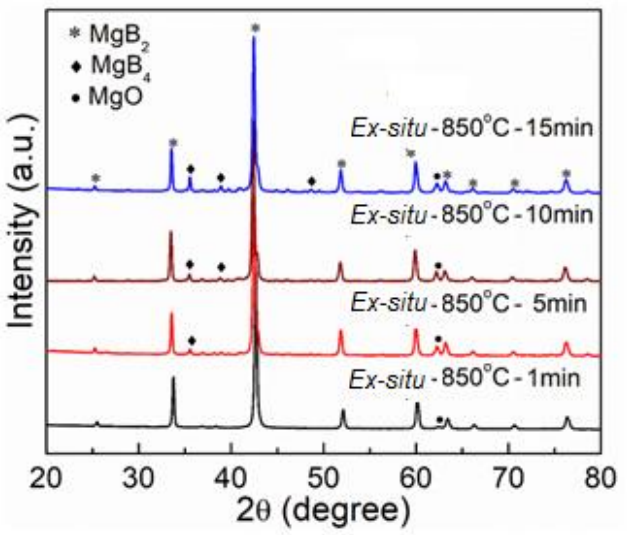

Figure 4.6**.** The X-ray diffraction patterns for MgB_2 *ex-situ* further optimization at 850 °C

To further control the decomposition occurred at 850 °C in SPS MgB_2 bulk sample, dwell time was varied and observed XRD patterns are shown in Figure 3. It was observed that as the dwell time decreased from 15 min to 1 min, the decomposition was effectively decreased. The densification values are shown in Table 1. These are the calculated values of the relative bulk densities. As the dwell time is controlled for each stage of synthesis from 15 min to 1 min, the densification was decreased from 97% to 86%, indicating that the dwell time is also important parameter. With the resent results, it can be observed that the sintering temperature of 850 °C and 10 min dwell is the best condition, which show minimal decomposition with relatively high densification values.

Table 4.1. The polycrystalline MgB_2 sample density was determined to be 1.73 g/cm^3 corresponding relative densification value is 66%. The density of the *ex-situ* - 800 °C - 15 min - *ex-situ* - 1000 °C - 15 min samples was found to be 2.41 g/cm^3 - 2.59 g/cm^3, which corresponds to 92 - 99 % of theoretical density. The densification values for dwell time, relative density, and superconducting transition ($T_{c(onset)}$, $T_{(offset)}$, ΔT_c) for samples prepared by *ex-situ* and *in-situ* methods are given in Table. The Standard Deviations(s) for $T_{c,S}$ and $\Delta T_{c,S}$: $\sigma < 0.21$.

Sample	Dwell Time (min)	Relative Density (%)	Superconducting transition (K)			Phase Decomposition
			$T_{c(onset)}$	$T_{(offset)}$	ΔT_c	
				Ex-situ		
Ex-situ_1000 °C	15	99	38.3	37.7	0.6	Present
Ex-situ_900 °C	15	99	38.2	37.7	0.5	Present
Ex-situ_850 °C	15	97	38.2	37.7	0.4	Reduced
Ex-situ_800 °C	15	92	38.5	37.7	0.8	Little
Ex-situ_850 °C	10	97	38.3	38.0	0.3	Improved/ little MgO
Ex-situ_850 °C	5	89	38.1	37.8	0.3	Improved/little MgO
Ex-situ_850 °C	1	86	38.5	37.9	0.6	Little MgO
				In-situ		
In-situ_775 °C	Tubular / 3 h	66	38.5	38.1	0.3	Little MgO
In-situ_775 °C	SPS / 20	90	38.3	38.0	0.3	MgO/MgB_4
In-situ_775 °C	SPS / 15	90	38.4	38.2	0.2	Little MgO
In-situ_750 °C	SPS / 15	88	38.3	38.1	0.3	Little MgO
In-situ_720 °C	SPS / 15	83	38.5	38.3	0.2	Little MgO

4.4 Superconducting Performance of MgB_2 Synthesized by ex-situ Process

The DC magnetic susceptibility curves that are normalized by the maximum superconducting values for *ex-situ* - 800 °C - 15 min measured to *ex-situ* - 1000 °C - 15 min samples are shown on the Figure 4(a) and the dwell time varied *ex-situ* - 850 °C - 1 min ÷ *ex-situ* - 850 °C - 15 min samples are shown on the Figure 4(b). Polycrystalline MgB_2 sample superconducting transition curve is also

included as reference. The onset of T_c for Polycrystalline MgB_2 is determined to be 38.5 K with transition width (ΔT_c) of 0.43 K. All samples show sharp superconducting transitions at onset value of > 38 K with ΔT_c of < 1 K except for 15 minutes sintered), indicating high quality nature of the fabricated MgB_2 bulks. The sample sintered at 15 mins dwell time showed a more degradation in T_c. However, since there is improvement J_c performance, there is need to optimize at temperature near the best sample J_c. The subsequent results showed no much degradation in the T_c which gives the impression about optimal T_c for the 850 ^oC series. The explanations about onset, offset and ΔT_c of the superconducting $T_{c,s}$ are illustrated in figure 4.7. The T_c (onset) for the SPS processed samples were measured at around T_c(10%) while the T_c(offset) was noted at about T_c(90%).

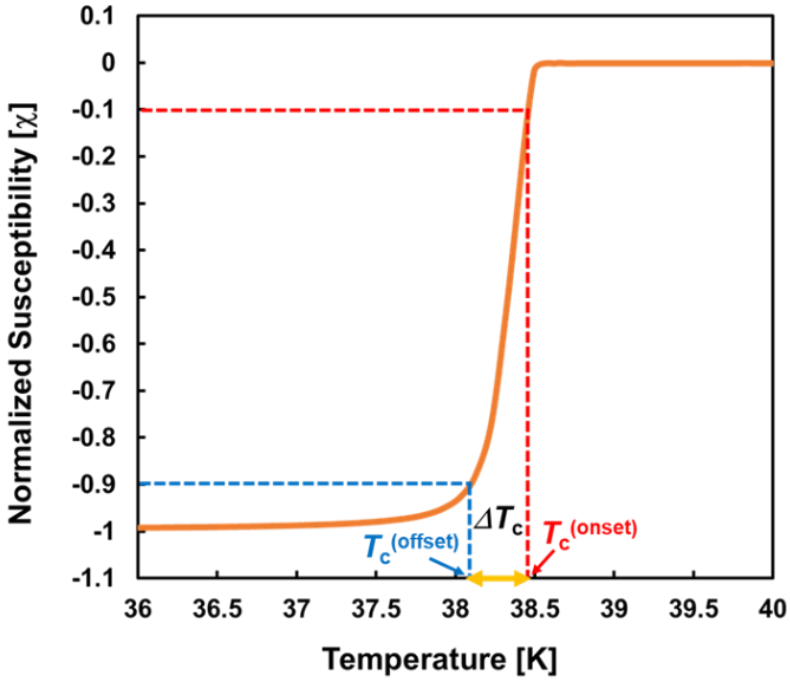

Figure 4.7 Definition of T_c (onset), (offset) and ΔT

Presently, our T_c results showed negligible reduction in the onset value of bulk samples compared to the polycrystalline sample. The width of the superconducting transitions ΔT_c of all the samples was observed to slightly decrease in both ex-situ and in-situ process as the processing temperature decreases at a controlled dwell time. The gradual degradation of the T_c may have resulted from the impurity phases which was more obvious in the ex-situ samples. This was also supported by M. E Yakinci et al. [33].

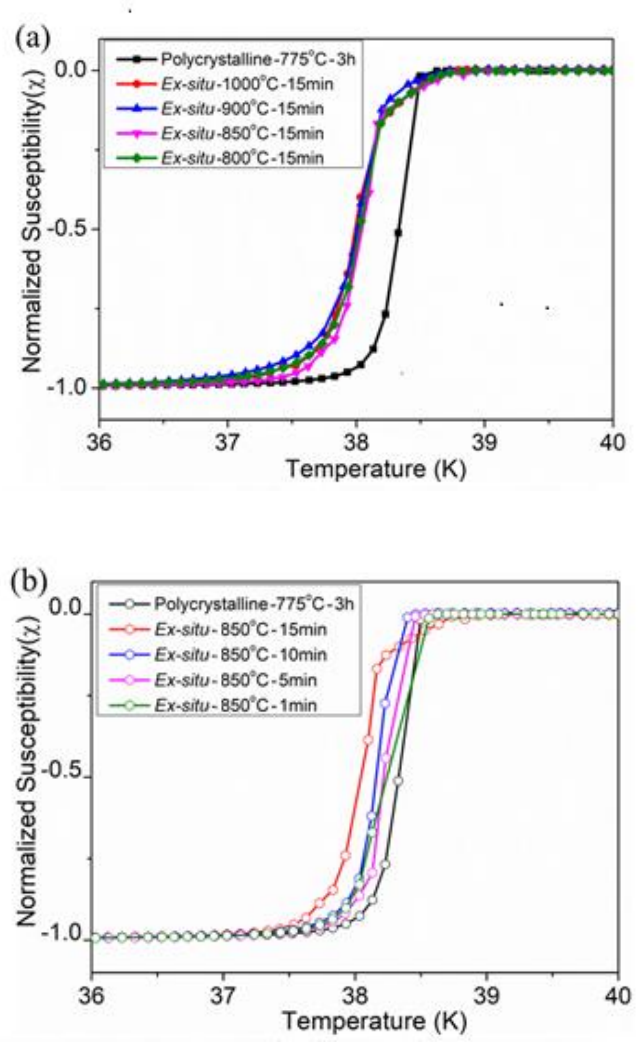

Figure 4.8. Superconducting transition in the bulk MgB_2 processed by SPS via *ex-situ* **(a)** variation of the sintering temperature, and **(b)** dwell time variation

The field dependance of $J_c(B)$ of the MgB_2 samples at 20 K was estimated utilizing extended Bean's critical state model [29]. Figure 5(a) shows the variation of J_c curves of MgB_2 bulk *ex-situ* samples synthesized at different sintered temperatures of 800 ℃, 850 ℃, 900 ℃, and 1000 ℃. Self-field J_c [$J_c(0)$] values for the samples are determined to be 401, 493 and 413 and 333 kA/cm^2 respectively. The $J_c(0)$ value for the Polycrystalline MgB_2 sample is 298 kA/cm^2, which clearly shows that the MgB_2 bulk samples supporting carrying large J_c compared to the sample produced by the conventional sintering method. Among, SPS processed MgB_2 samples, *ex-situ* - 850 ℃ - 15 min superconductor was observed to be superior in the J_c performance which could be attributable to the high density along with the relatively lower fraction of the secondary phase formation as indicated on the sample XRD. Also, even though the densification values are higher in the case of 900 ℃ and

1000 ℃ sintered samples, J_c performance is inferior and worsen as the sintering temperature increased. This is mainly due to the MgB_2 phase degradation into non-superconducting phases into large fraction. To further control this effect, we tried to control the regime of the sintering process. The $J_c(H)$ curves determined at 20 K for the *ex-situ* - 850 ℃ - 1 min to *ex-situ* - 850 ℃ - 15 min superconductors are shown in Figure 5(b). The self-field J_c of the *ex-situ*- 850 ℃ - 1 min, *ex-situ* - 850 ℃ - 5 min, *ex-situ* - 850 ℃ - 10 min, *ex-situ* - 850 ℃ - 15 min superconductors are determined to be 420 kA/cm^2, 495 kA/cm^2, 517 kA/cm^2, 493 kA/cm^2 respectively. The MgB_2 *ex-situ* bulk synthesized at 850 ℃ for 10 min' exhibited superior field dependence J_c performance. Present our results are superior to the reports available in literature on the MgB_2 bulks produced by SPS and HP [28,32]. The superior field dependence properties of *ex-situ* - 850 ℃ - 15 min superconductor could be attributable to the optimal sintering temperature and controlled dwell time at which the phase degradation was minimal with a corresponding improvement in the density. With this we successfully fabricated highly dense MgB_2 bulk samples via *ex-situ* SPS method and mainly such high densification values are achieved at lower sintering temperatures.

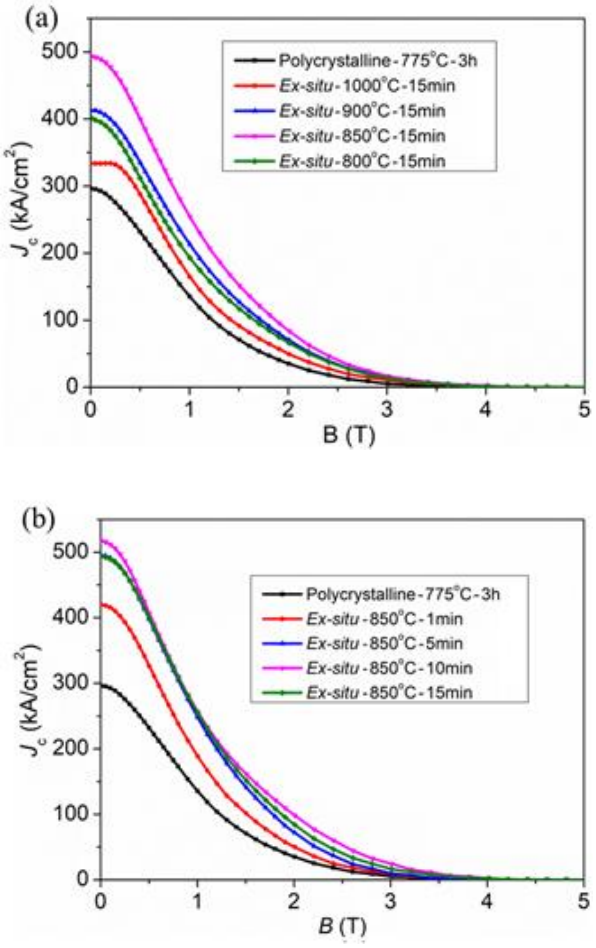

Figure 4.9. The magnetic field dependence of J_c curves determined at 20 K for MgB_2 bulk superconductors fabricated by SPS *ex-situ* method for (a) Sintering temperature variation, and (b) dwell time variation

The J_c-B distributions within the ex-situ sample was further investigated to examine the homogeneity. The results displayed in figure 4.10 showed the average distribution of the critical current densities to be around 10 to 15 kA/cm2 difference. This value is negligibly insignificant when considering the average values. The regions X1, X2, X3, X4, X5 corresponds to the respective $J_{c,s}$ 510, 508, 502, 513, 515 kA/cm^2. The refinement of grains and uniform composition of the MgB_2 phase was supported by several literatures [28] [32] [34] of which this work shows more proof to support these claims. The SPS is therefore regarded as one of the best ways of synthesizing homogeneous bulk MgB_2.

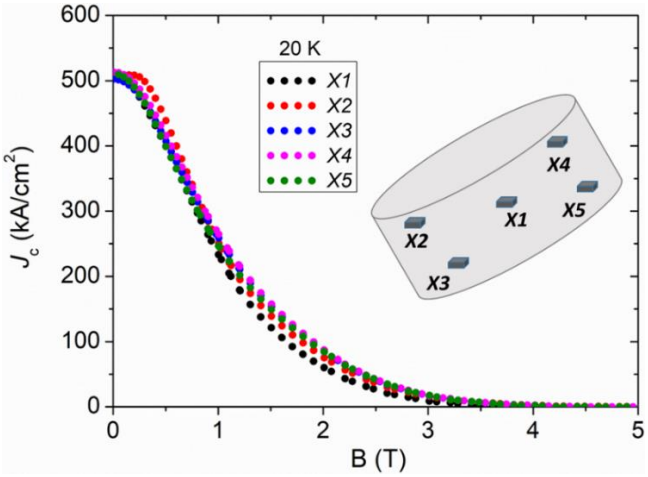

Figure 4.10. The magnetic field dependence of J_c curves determined at 20 K for the optimized MgB_2 bulk fabricated by SPS *ex-situ* method. It shows uniform J_c-B distribution in the sample. (Inset shows schematics of the analyzed regions)

4.5 Synthesis and Characterization via In-situ Process

In above sections, we produced MgB_2 bulk superconductors with high mass density supporting large critical currents via *ex-situ* SPS method. However, in order to reduce the cost of the application and time, we attempted to synthesize the MgB_2 bulk samples via in-situ SPS method by mixing the stoichiometry ratios of Mg and B. In a similar way to the ex-situ process, in this section also tried to study the effect of rate of change of current application and dwell time on the synthesis of bulk MgB_2 superconductor. With the concept derived from our previous trials during the ex-situ process, we can suggest that this will later give us an idea of the temperature and dwell time to be employed during the in-situ processing. Thermodynamically, an intimate mixture of boron and magnesium powder will react when elevated to a sufficiently high temperature. The reaction, once initiated, has a large positive heat of reaction, and tends to spread in an orderly manner throughout the mass of the reaction mixtures. This reaction route is demonstrated in figure 4.11 (a)-(d). In conventional in-situ solid state

sintering, the formation of MgB_2 is usually accompanied with the formation of MgO and voids, this has a drawback effect on the connectivity and mechanical property of the bulk MgB_2 superconductor. The SPS process has a greater advantage in solving these problems.

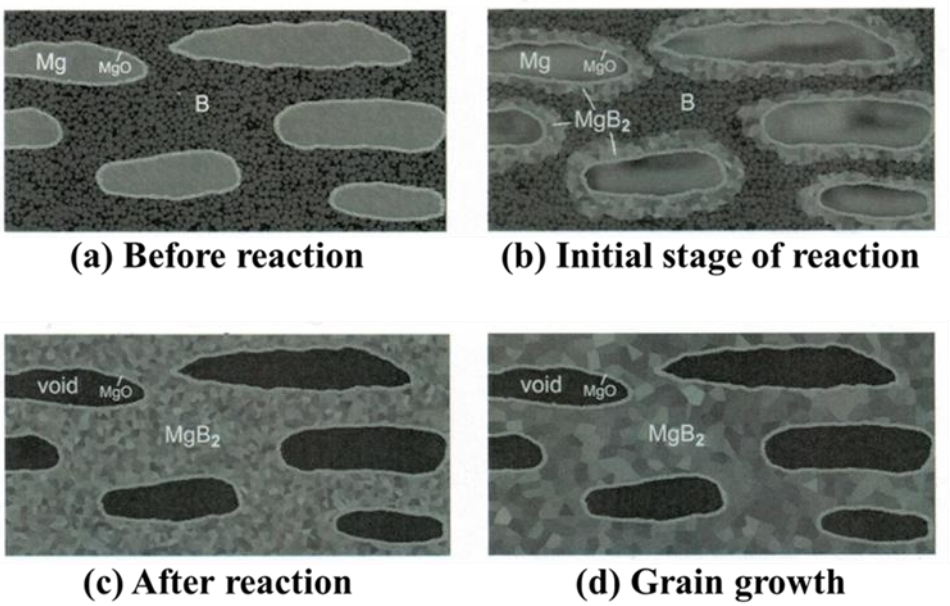

Figure 4.11 Reaction stages in situ reaction process

A common issue associated with in-situ processing is the loss of Mg during sintering process. To be able to control that, we tried a manual application of the current in two separate stages 300A and 325A slowly while regulating the temperature at a rate of 50 ^{o}C/min, an initial dwell time of 20min was considered during the trial process. Prominent loss of Mg was observed during this stage as shown in figure 4.12, this process was repeated by running the sintering process on automatic mode, however, the phase examination in figure 4.13 shows almost no difference with the manual mode. Here we examine the top and bottom side of the sintered bulk MgB_2 which showed no clear distinction in the phase compositions. We may also draw from this analogy that SPS process is most reliable when it comes to the matter of homogeneity or uniformity. A more precise and systematic approach was adopted for the subsequent in-situ process which is further discussed in subsequent sections which was also considered for comparative studies. The in-situ approach is aimed at fabrication of the bulk with abundant amounts of the grain-connectivity along with high mass density due to *in-situ* reaction which could support even larger $J_{c,s}$ in the MgB_2 bulk samples.

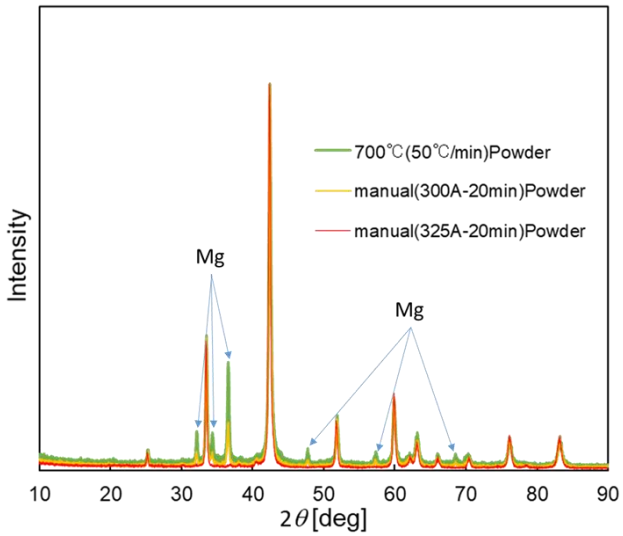

Figure 4.12. XRD analysis of manually controlled current application showing prominent Mg peaks

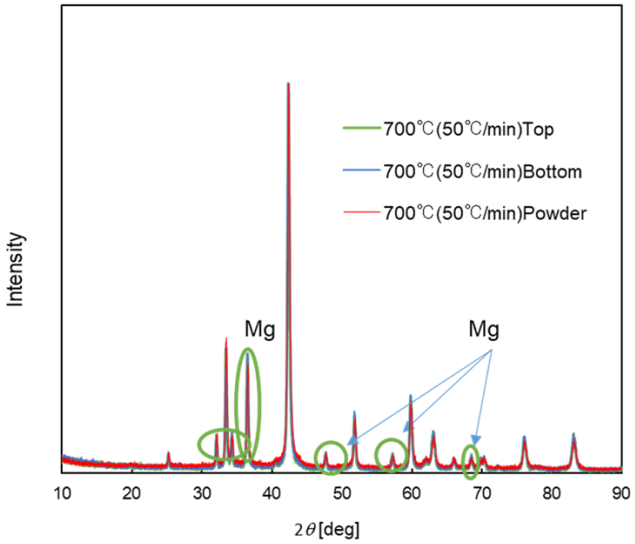

Figure 4.13. XRD analysis of manually controlled current application showing prominent Mg peaks

4.6 Phase Analysis for MgB_2 In-Situ Process

A systematic approach to fabricate and analyze the bulk MgB_2 produced via the in-situ SPS process is discussed in this section. The *in-situ* process for the phase analysis is shown in Figure 4.14, the observed XRD was compared to our previously fabricated bulk sample in chapter I using the *in-situ* solid state sintering technique by the tubular furnace at 775 °C for 3 h condition.

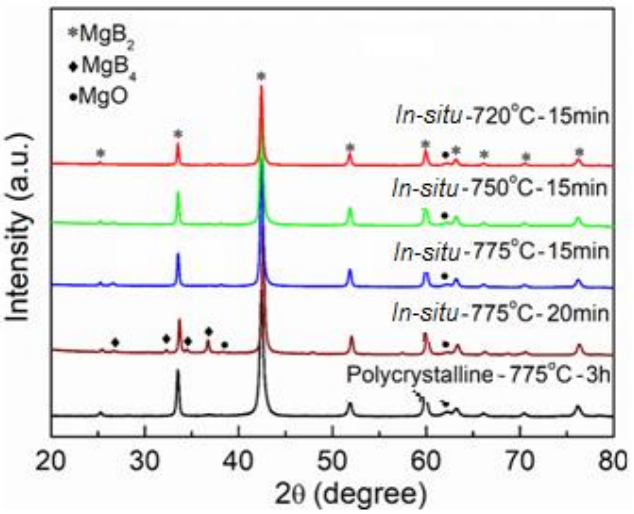

Figure 4.14**.** The X-ray diffraction patterns for spark plasma sintered MgB_2 bulk via *in-situ* method

In this section, we already tried to synthesize *in-situ* MgB_2 bulk by SPS using the same temperature condition but with an idea from our previous trials of a long dwell time of 20 min for starters. With the occurrence of decomposition at this condition, we proceeded by slightly decreasing the dwell time and controlling the sintering temperatures which was found to be effective for decreasing the deterioration of the MgB_2 phase, however, it was necessary to find the optimum temperature for high-density conditions which we could also attain an equilibrium for the superconducting performance of our bulk *in-situ* samples.

4.7 Superconducting Performance of MgB_2 Synthesized by in-situ Process

The superconducting transitions in the MgB_2 bulk synthesize by *in-situ* process is shown in the Figure 4.15. The Figure 4.16 shows the superconducting field performances of the J_c of the *in-situ* process. Besides the contributions of secondary particles, one of the important observation we made was the significant increase in the SPS insitu sample density by sole temperature control and grain size refinement while keeping the initial pressure of 50 MPa, we could achieve ~90% density. This could be a breakthrough when further optimization by pressure increase is employed, this could exceed the findings of Prikhna et al. [31] for the highest density by SPS insitu process and hence the superconducting performance and mechanical properties.

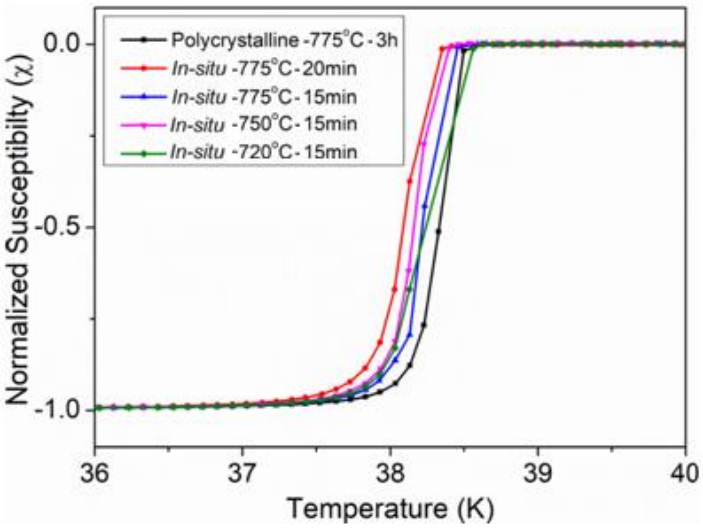

Figure 4.15. The superconducting transitions in the MgB_2 bulk synthesize by *in-situ* process

More crystallinity was observed for *in-situ* samples than the *ex-situ* which is evident in the degree of sharpness for the superconducting transitions. The observed suppression in the *ex-situ* samples T_c could be due to the effect of the impurity phases which occurred in the XRD analysis. This observation on the slight suppression in the T_c was supported by Dancer et al. [34]. This suggest that the lower processing temperatures could've attained a degree of sufficiency in recovering the disorder that may have existed in the initial as-received powders.

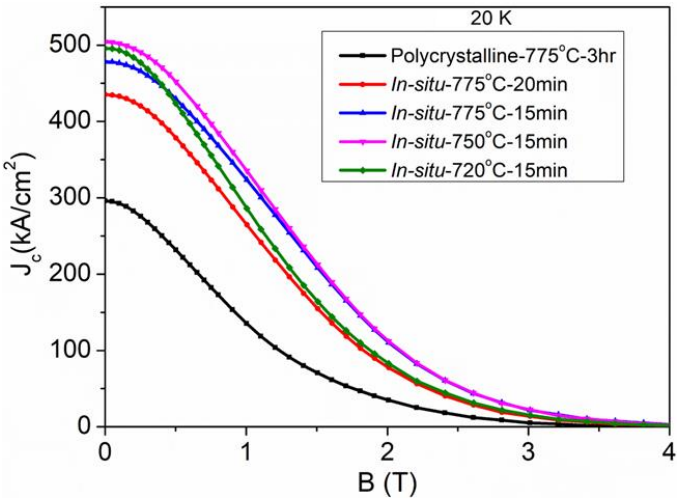

Figure 4.16. Shows the superconducting field performances of the J_c of the *in-situ* process.

All the samples tend to show improvement in the field performance, when compared to the bulk synthesized via tubular furnace, however, the *in-situ* processed bulk sample at 750 °C was optimal at 504 kA/cm^2 at 88% packing density for these set of samples. This is so promising when compared to the recent reports of Noudem et al. [28] for *in-situ* processing at 500 kA/cm^2 and 84% packing density. We suggest that the field dependence of the respective J_c varies with temperature optimization as a

function of the grain size refinement and hence the densities. The additional pinning centers in this case may also have resulted from the nano-sized particles which also maximizes the flux pinning performance exhibited by our best sample bulks meanwhile we also proposed that the relevance of the J_c improvement is also attributed to the contribution of the refinement of the grains which improved the flux pinning performance and consequently the J_c.

In a similar way to the *ex-situ* process, the J_c-B distribution of the optimal *in-situ* bulk MgB_2 sample was analyzed with the sole aim of determining and confirming the homogeneity of the bulk sample. The realization of the conformity with an averagely optimized $J_{c,s}$ with minimal difference across different regions noted within the sample is an additional knowledge to the reliability of the SPS process in the synthesis of bulk materials. Figure 4.17 shows the characteristic J_c- B of the different regions *Y1, Y2, Y3, Y4, Y5* and their respective $J_{c,s}$. The average J_c is around 500 kA/cm^2 which barely differs from the optimal value.

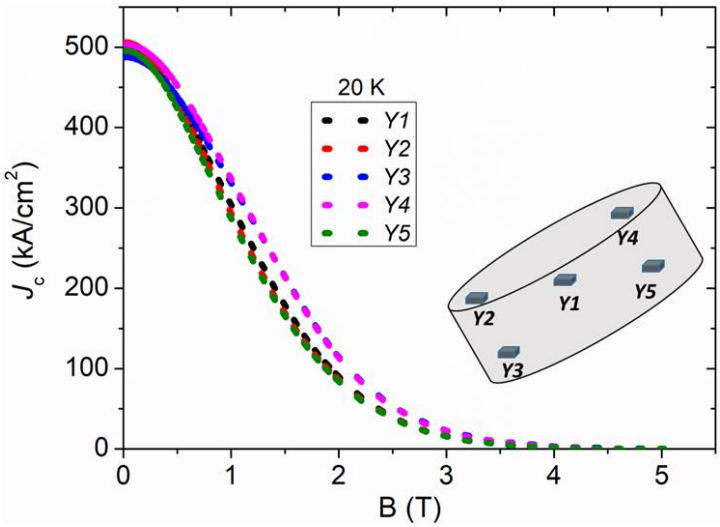

Figure 4.17. The magnetic field dependence of J_c curves determined at 20 K for the optimized MgB_2 bulk fabricated by SPS *in-situ* method. It shows uniform J_c-B distribution in the sample. (Inset shows schematics of the analyzed regions)

4.8. Microstructural Analysis

The grain size and grain connectivity are crucial for determination of the J_c in polycrystalline superconductors. Microstructural characterization carried out via FE-SEM on the *ex-situ* - 850 ℃ - 10 min and *in-situ* - 750 ℃ - 15min samples are compared with Polycrystalline MgB_2 sample in Figure 4.18(a)-(c) respectively. The statistical analysis of the grain size is done using imageJ program and the corresponding size histograms are shown in Figure 4.18(d)-(f) respectively. The mean size of the MgB_2 grains for polycrystalline MgB_2, *ex-situ* - 850 ℃ - 10 min and *in-situ* - 750 ℃ - 15 min samples are determined to be 112 nm, 119 nm and 132 nm respectively. These results vindicate that

the MgB_2 bulk samples produced via SPS contain slightly fine sized MgB_2 superconducting grains than the polycrystalline MgB_2 sample. It is interesting to note here that the, even though both the *ex-situ* - 850 ℃ - 10 min and *in-situ* - 750 ℃ - 15 min samples are fabricated by the SPS method, fine sized grains frequency is larger in the case of former sample. This could be as a result of the further and careful optimization of the dwell time during the *ex-situ* processing which could have further controlled the grain sizes.

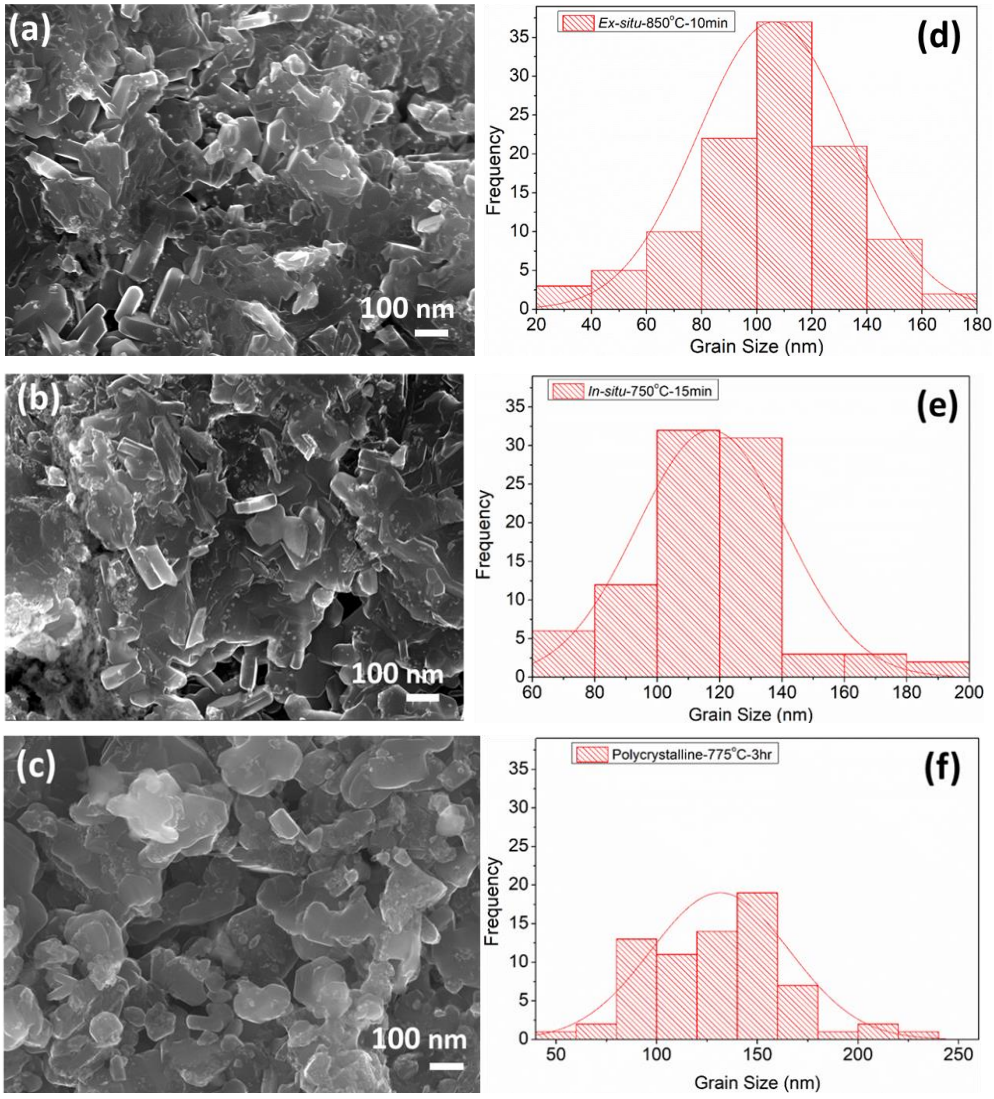

Figure 4.18. High magnification (X30,000) SEM images for optimized fractured bulk samples produced by **(a)** SPS *ex-**situ***, **(b)** SPS *in-situ*, and **(c)** polycrystalline MgB_2. Statistical analysis of the grain and the corresponding size histograms are shown in Figure (d)-(f) respectively.

In order to complement our FE-SEM observations, we further conducted microstructural analyses via TEM investigations as shown in Figure 4.18 on *ex-situ* - 850 °C - 10 min and *in-situ* - 750 °C - 15 min samples. We could suggest the occurrence of the nano size MgO particles which may have

enhanced the flux pinning of the SPS processed samples implying that the interactive contributions of the refined grains and the MgO inclusions could have been our primary source of the improved superconducting performance. In *ex-situ* SPS processing, our observation for the optimized sample indicated the presence of nano size grains of MgB_4 as shown in Figure 10(a) which could've been a contributor to supporting the superconducting J_c. The TEM results for this samples in Figure 4.19(a) showed more refined grains of MgB_4 as secondary phase and also what could possibly be the inclusion of the MgO particles. We suppose that the dramatic increase in the superconducting J_c is attributed to this effect. As for the *in-situ* process, the microstructure reveals the occurrence of the MgO system within the MgB_2 matrix for the optimized conditions, but more grains tend to manifest with shorter dwell time resulting in better connectivity and more controlled inclusion of the MgO as illustrated in Figure 4.19(b).

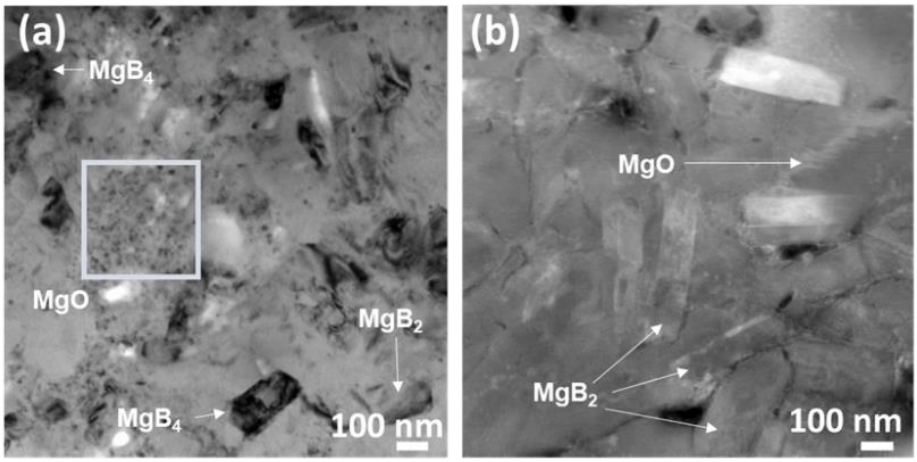

Figure 4.19. The TEM micrographs of optimized polished surfaces of **(a)** SPS *ex-situ* **(b)** SPS *in-situ*

Our findings indicate that both SPS processed bulk samples are superior compared to polycrystalline sample. It could be emphasized here that the grain refinement by virtue of the grain sizes, connectivity and the resulted improved densities aided in enhancing the J_c. Among bulk samples, they exhibit different flux pinning behaviors as the slope of the J_c curves are different at different fields. This clearly indicates that the clean grain boundary, lower porosity along with relatively higher densification supporting high $J_{c,s}$ at moderate applied magnetic fields along with the nano-sized secondary phases as observed from TEM. With this we successfully synthesized the MgB_2 bulk samples via *in-situ* method by SPS in its pure phase. Present self-field results are slightly inferior compared to *ex-situ* bulks. However, it should be noted here that, *in-situ* bulks are of low densification compared to ex-situ but still exhibit high quality of the bulk samples compared to recent report [28]. By further optimization of the processing parameters high quality of MgB_2 bulks can be fabricated

which support even superior field dependence properties compared to any other methods. In our case, processing temperature and dwell time were the variable parameters considered to be effective.

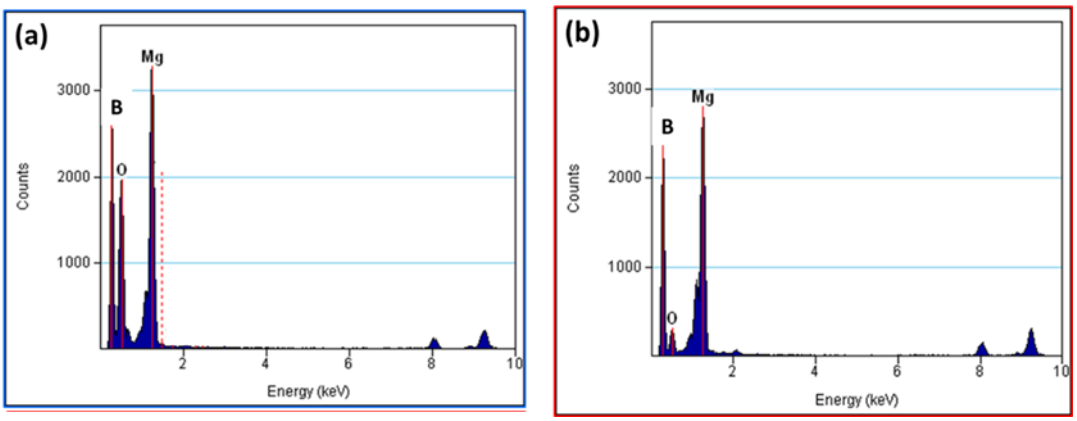

Figure 4.20 EDX spectra of (a) in-situ MgB_2 matrix, (b) the ex-situ MgB_2 matrix

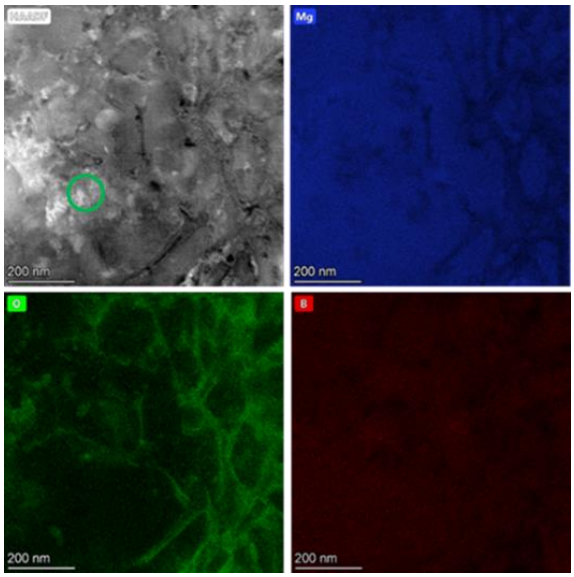

Figure 4.21 Analysis of EDX mapping surface of optimized ex-situ MgB_2 sample

The composition was further investigated using the energy-dispersive spectra (EDX) taken from very thin areas of each optimized ex-situ and in-situ sample edge. Figure 4.20 shows the EDX results of (a) the optimized ex-situ MgB_2 sample (b) optimized in-situ MgB_2 sample. Small amount of oxygen is seen in the in-situ MgB_2 matrix while the oxygen content is higher in the Matrix of MgB_2 ex-situ sample, this reason could be attributed to the large interaction of oxygen in the form of MgO in the ex-situ representative sample than in the in-situ sample. Because of the small precipitate sizes used in this experiment, we believed that the signals from the surrounding matrix material may have also contributed to the EDX spectrum in Figure 4.20 (a) and (b) and therefore the EDX spectrum itself may not conclude our findings. Superimposition of the particles with the MgB_2 is common and expected. This is also supported by reported literatures [39]. To confirm that our sample precipitates

do contain boron or higher borides most especially MgB_4, mapping analysis was carried out to support our earlier claims. The analysis obtained for the MgB_2 matrix for each case of in ex-situ and in-situ and are shown in Figure 4.21 and 4.22 respectively. Small precipitates mostly contain all three elements Mg, B, and O_2 implies that the composition in precipitates varies with precipitate size. The oxygen content increases, while the boron content decreases, with increasing precipitate size, indicating the substitution of boron by oxygen [40]. The oxygen in the samples may have resulted when transferring the samples from the glovebox to the SPS chamber during the MgB_2 synthesis process. It is believed that MgB_2 has relatively high oxygen solubility at the synthesis temperature. Perhaps because of this situation, it is difficult to escape the formation of MgO which is the medium for trapping the precipitated O_2. The mapping analysis explained here only gives us further claims of the existence of residual O_2 and to provide ideas to support our earlier claims of the provisional pinning centers which came from further control of the particle sizes of these inclusions.

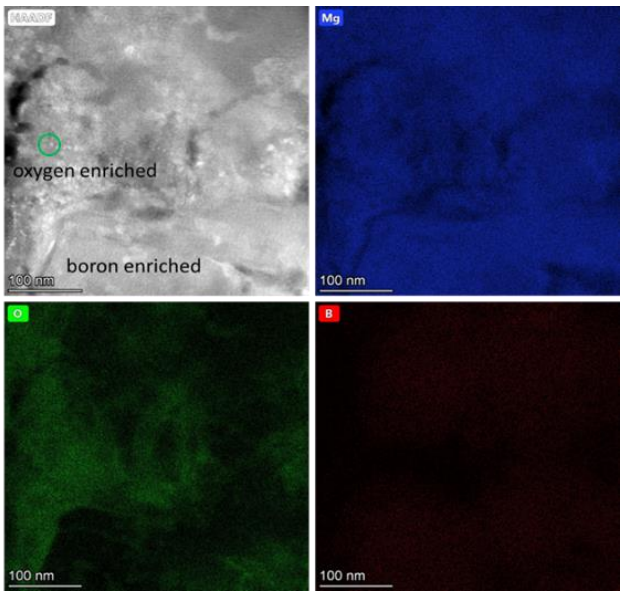

Figure 4.22 Analysis of EDX mapping surface of optimized in-situ MgB_2 sample

4.9. Flux Pinning Analysis

To support our discussions from the TEM analysis, the pinning force, f_p was investigated using a scaling method based on the body of literature data and compared to our studies. We calculated the scaling behavior and the best fits to the theory using the scaling methods of Dew-Hughes [35] and Kramer [36]. Flux pinning of the fabricated MgB_2 bulk samples are scaled using Dew-Hughes general expression

$$f_p = A \cdot (h)^p \cdot (1-h)^q \qquad \text{..... (1)}$$

Constants p and q are describing the actual pinning mechanism. The normalized flux pinning force density is denoted by $f_p=F_p/F_{p,max}$, and the reduced magnetic field is $h=H/H_{irr}$. The value of the irreversibility field, H_{irr}, was estimated as the field where J_c decreased to 100 A/cm^2 at 20 K, which is customary in our works. The normalized pinning force $F_p/F_{p,max}$ versus the reduced fields were plotted and curves are shown in Figure 11. In previous chapters, the analyses of the flux pinning behaviors using the Dew-Hughes model was utilized. The same applies to the samples produced in this section. The model describes the peak position of the $f_p(h)$ dependence which indicates the type of pinning in the superconducting material. The so-called model has the peak positions in f_p vs. h at 0.2 to imply grain boundary pinning, meanwhile 0.33 implies core, δT_c pinning, as also emphasized in previous chapters. This types of flux pinning behaviors was being also further explained in literature reports [37] on the pinning force scaling analysis for high-T_c superconductors. The resulting peak positions, h_o, were found around ~0.25 and ~0.28 respectively for the optimized *in-situ* and *ex-situ* samples, a slight shift to the right towards higher field which supports the indication for particle pinning. The implication here is that some of contributions of the flux pinning may have resulted from nano-sized inclusions of the secondary phases, this assertion is also supported in the TEM analysis discussed in Figure 10. However, the polycrystalline bulk sample tend to exhibit the ideal peak position which is around 0.22 indicating the effect of grain boundaries for vortex pinning. The shifts in the peak positions could also be attributed to the improved connectivity and the resulting refined grains which added to our highly suspicion of the temperature control and dwell time during synthesis. The mechanism for pinning other than grain boundaries for MgB_2 was emphasized by other reports [38] which also supports our findings. The Figure 4.23 shows the flux pinning diagram showing peak positions for the optimized *in-situ* and *ex-situ* samples compared with polycrystalline MgB_2.

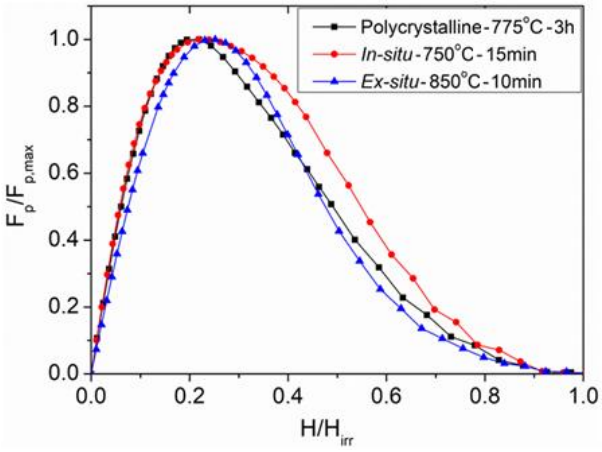

Figure 4.23**:** The flux pinning diagram showing peak positions for the optimized *in-situ* and *ex-situ* samples compared with polycrystalline MgB_2. Slight shift in peak positions to the right.

4.10 Summary On Optimization of Sintering Conditions via In-situ and Ex-situ SPS Process

This chapter have discussed the influence of sintering temperature and dwell-time on J_c-B properties of dense in-situ and ex-situ MgB_2 bulks synthesized by SPS. However, it is obvious that the J_c-B characteristics improved as a result of appropriate nano-inclusions of MgO and MgB_4 impurity phases in the final microstructure, which resulted in significant flux pinning enhancement. In-situ and ex-situ, the best samples demonstrated self-field J_c behaviors at 504 and 517 kA/cm^2, respectively. The good grain refinement and connection, which also influenced the high bulk densities, may have resulted in more improved J_c behaviors. Nevertheless, the ex-situ synthesis is complicated and time-consuming despite the challenges in controlling the impurity phases. We proposed that it might be appropriate to consider in-situ processing method of synthesizing high density MgB_2 bulk which is less complicated and time-saving with ease of control of the impurity phase. Meanwhile, more progress can be achieved for SPS in-situ processing by improving the quality of starting powders and applying high-pressure sintering. Our approach also supports the possibilities of other processing windows in which well-sintered MgB_2 cores in wires and bulk magnets can be fabricated for practical applications.

References

[1] V. Russell, R. Hirst, F.A. Kanda, A. J King, "An X-ray study of the magnesium borides. Acta Cryst. **6** (1953) 870.

[2] J. Nagamatsu, N. Nakagawa, T. Muranaka, Y. Zenitani, J. Akimitsu, "Superconductivity at 39 K in Magnesium Diboride". Nature, **410** (2001) 63.

[3] A. Murakami, J. Noudem, Z. Guesmi, T. Kudo, A. Iwamoto, "Mechanical Properties of MgB_2 Bulk Fabricated by Spark Plasma Sintering" Physics Procedia., *65*, (2015) 77.

[4] A. Murakami, A. Iwamoto, J.G. Noudem, "Mechanical properties of bulk MgB_2 superconductors processed by spark plasma sintering at various temperatures" IEEE Trans Appl Supercond., *28*, (2018) 8400204.

[5] M. Eisterer, M. Zehetmayer, H.W Weber, "Current Percolation and Anisotropy in polycrystalline MgB_2" Phys Rev Lett., **90** (2003) 247002.

[6] A. Murakami, A. Iwamoto, J.G. Noudem, "Mechanical properties of bulk MgB_2 superconductors processed by spark plasma sintering at various temperatures". IEEE Tran. Appl. Supercond.**, 28 3**, (2018) 1.

[7] J.G Noudem, L. Dupont. L. Gozzelino, P. Bernstein, "Superconducting properties of MgB_2 bulk shaped by spark plasma sintering" Mat. Today**,** 3 **2***,* (2016) 545.

[8] D. Gajda, A. Morawski, A. Zaleski, M. Kurnatowska, T. Cetner, G. Gajda, A. Presz, M. Rindfleisch, M. Tomsic, "The influence of HIP on the homogeneity, J_c, *B*irr, T_c and F_p in MgB_2 wires" Superconduc. Sci. Technol.**,** 28 **1**, (2014) 015002.

[9] D. Gajda, A. Morawski, A.J. Zaleski, W. Häßler, K. Nenkov, M.A. Rindfleisch, E. Żuchowska, G. Gajda, T. Czujko, T. Cetner, M.S.A Hossain, "The Critical Parameters in *in-situ* MgB_2 Wires and Tapes with Ex-situ MgB_2 Barrier After Hot Isostatic Pressure, Cold drawing, Cold Rolling and Doping" J. Appl. Phys.**,** 117 **17**, (2015) 173908.

[10] S.H. Shim, K.B Shim, J.W. Yoon, "Superconducting characteristics of polycrystalline MgB_2 ceramics fabricated by a spark plasma sintering technique" J. Am. Ceram. Soc.**,** 88 **4** (2015) 858.

[11] G. Aldica, D. Batalu, S. Popa, I. Ivan, P. Nita, Y. Sakka, O. Vasylkiv, L. Miu, I. Pasuk, P. Badica, "Spark plasma sintering of MgB_2 in the two-temperature route, Physica C: Superconductivity and its applications" **477** (2012) 43.

[12] D. Larbalestier, A. Gurevich, D.M. Feldmann, A. Polyanskii, High-T_c superconducting materials for electric power applications, Nature**, 410** (2001) 368.

[13] V. Braccini, D. Nardelli, R. Penco, G. Grasso, "Development of ex-situ processed MgB_2 wires and their applications to magnets", Physica C**, 456** (2007) 209.

[14] B.A Glowacki, M. Majoros, M. Vickers, J.E. Evetts, Y. Shi, I. McDougall, Superconductivity of powder-in-tube MgB_2 wires. Superconduc. Sci. Technol**,** 14 **4** (2001) 193.

[15] J.H Yi, K.T. Kim, B-H. J. Jun, J.M. Shon, "Pore formation in *in-situ* processed MgB_2 superconductors", Physica C: Superconductivity**,** 469 **15**, (2009) 1192.

[16] W. Jo, J-U. Huh, T. Ohnishi, A.F Marshall, M.R. Beasley; R.H. Hammond, *In-situ* growth of superconducting MgB_2 thin films with preferential orientation by molecular-beam epitaxy, Appl. Phys. Lett.**,** *80*, (2002) 3563.

[17] X.H. Zeng, A. Sukiasyan, X.X. Xi, Y.F. Hu, E. Wertz, Q. Li, "Superconducting properties of nanocrystalline MgB_2 thin films made by an in-situ annealing process", Appl. Phys. Lett**, 79**, (2001) 1840.

[18] Y. Liu, F. Cheng, W. Qiu, Z. Ma, S. Hossain, S.X. Dou, "High performance MgB_2 superconducting wires fabricated by improved internal Mg diffusion process at a low temperature", J. Mat. Chem**,** C **4** (2016) 9469.

[19] G. Giunchi, S. Ceresara, G. Ripamonti, A. Di Zenobi, S. Rossi, S. Chiarelli, M. Spadoni, R. Wesche, P.L. Bruzzone, "High performance new MgB_2 superconducting hollow wires", Supercond. Sci. Technol. 16 **2,** (2003) 285.

[20] Z.Y. Fan, D. Hinks, N. Newman, J. Rowell, "Experimental study of MgB_2 decomposition", Appl. Phys. Lett., 79 **1** ,(2001) 87.

[21] R. Schmitt, J. Glaser, T. Wenzel, K. Nickel, H.-J. Meyer, A reactivity study in the Mg-B system reaching for an improved synthesis of pure MgB_2, Physica C**, 436**, (2006) 38.

[22] S. Brutti, G. Balducci, G. Gigli, A. Ciccioli, P. Manfrinetti, A. Palenzona, "Thermodynamic and kinetic aspects of decomposition of MgB_2 in vacuum: Implications for optimization of synthesis conditions", J. Cryst. Growth**, 289** (2006) 578.

[23] Y. Guo, W. Zhang, D. Yang, R-L. Yao, "Decomposition and oxidation of magnesium diboride", J. Am. Ceram. Soc.**,** 95 **2**, (2012) 754.

[24] D.-K Kang, D.-W. Kim, C.-J. Kim, I.-S. Ahn, The Phase Analysis of Spark Plasma Sintered MgB_2 After Ball Milling, J. Nanosci. Nanotechnol.**,** 10 **1** (2010) 142.

[25] L. J. Dadiel, M. Muralidhar, M. Murakami, Flux pinning and superconducting properties of MgB_2-diamond nanocomposites, J. Phys: Conf. ser.**, 1054**, (2017) 313.

[26] L.J. Dadiel, M. Muralidhar, M.; Murakami, Improved superconducting performance of Ag-added nano-diamond doped MgB_2, Proc. SPIE **11054**, (2019) 110540I.

[27] N. Ojha, G.D Varma, H.K Singh, V.P.S Awana, Effect of rare-earth doping on the superconducting properties of MgB_2, J. Appl. Phys**,** 105 **7** (2009) 07E315.

[28] J.G. Noudem, X. Yiteng, B. Pierre, R. Richard, H. Masaki, S.A. Srikanth, M. Miryala, M. Masato, Improvement of critical current density of MgB_2 bulk superconductor processed by Spark Plasma Sintering, J. Amer. Ceram. Soc. 103 **11** (2020) 6169-6175

[29] D. Chen, R.B Goldfarb, Kim model for magnetization of type-II superconductors, J. Appl. Phys.**,** *66*, (1989) 2489.

[30] G. Balduccia, S. Bruttia, A. Cicciolia, G. Giglia, P. Manfrinettib, A. Palenzonab, M.F. Butmanc, L. Kudinc, Thermodynamics of the intermediate phases in the Mg–B system, J. Phys. Chem. Soli.**, 66** (2005) 292.

[31] T. Prikhna, J. Noudem, W. Gawalek, A. Mamalis, A. Soldatov, Y. Savchuk, V. Moshchil, M. Eisterer, H.W. Weber, S. Dub, T. Habisreuther, J. Dellith, Y. Shujie, C. Schmidt, F. Karau, U., Dittrich, I. Vajda, N. Sergienko, V. Sokolovsky, D. Litzkendorf, X. Chaud, V. Sverdun, R. Kuznietsov, Spark plasma synthesis and sintering of superconducting MgB_2-based materials, Mat. Sci. Forum**, 721** (2012) 3.

[32] W. Häßler, J. Scheiter, P. Hadrich, S. Kauffmann-Weiß, B. Holzapfel, M, Oomen, K. Nielch, Properties of ex-situ MgB_2 samples prepared by uniaxial hot pressing and spark plasma sintering, Physica C: Supercond. and its application **48** (2018) 551.

[33] M.E. Yakıncı, Y. Balcı, M. A Aksan, H.I Adiguzel, A and Gencer, A, Degradation of Superconducting Properties in MgB_2 by Formation of the MgB_4 Phase, Journal of Superconductivity: Incorpo. Nov. Mag., 15 **6** (2002) 607.

[34] C. E.J Dancer, D. Prabhakaran, M. Basoglu, E. Yanmaz, H. Yan, M. Reece, R.I Todd, and C.R.M Grovenor, Fabrication and properties of dense ex-situ magnesium diboride bulk material synthesize using spark plasma sintering, Supercond. Sci. Technol., **22** (2009) 095003.

[35] D. Dew-Hughes, "Flux pinning mechanisms in type-II superconductors", Philos. Mag. **30** (1974) 293.

[36] E.J Kramer, "Scaling laws for flux pinning in hard superconductors", J. Appl. Phys., **44** (1973)1360.

[37] M. Koblischka, and M. Muralidhar**,** Pinning force scaling analysis of Fe-based high-T_c superconductors, Inter. J. Mod. Phys. B **30**, **(**2016**)** 1630017.

[38] A. Kario, R. Nast, W. Häßler, C. Rodig, C. Mickel, W. Goldacker, B. Holzapfel, L. Schultz, "Critical current density enhancement in strongly reactive ex-situ MgB_2 bulk and tapes prepared by high energy milling", Supercond. Sci. Technol**.** 24, **7** (2011) 075011.

[39] X. Z. Liao, A. Serquis, Y. T. Zhu, J. Y. Huang, L. Civale, D. E. Peterson, and F. M. Mueller, "Mg (B, O)$_2$ precipitation in MgB_2" J. of Appl. Phys. **93** (2003**)** 6208

[40] R. F. Klie, J. C. Idrobo, N. D. Browning, K. A. Regan, N. S. Rogado, and R. J. Cava, "Direct observation of nanometer-scale Mg- and B-oxide phases at grain boundaries in MgB_2" Appl. Phys. Lett. **79** (2001**)** 1837

Chapter V

Field-Trapping Performance of Drilled MgB_2 Bulk Superconductor Embedded with Bi-In-Sn Alloy and Al-rod Using Pulse-Field Magnetization Processes

This chapter of the thesis presents the method for characterizing the propagation of the magnetic flux in an artificially drilled MgB_2 bulk superconductor fabricated by the SPS technique. This study helps to solve the flux jump problem in the bulk superconductor resulting from poor heat dissipation during pulse field magnetization experiment. The bulk MgB_2 sample was redesigned to enhance both the thermal properties and to suppress flux jumps during the pulse applications. This study discusses the magnetic flux dissipation, the flux motion, and performance by evaluation of the capture field ratio. The aim of this study is to;

a) Study the effect of applied fields, B_A on the drilled bulk MgB_2 embedded with low melting alloy of Bi-In-Sn alloy and aluminum rods within the holes.
b) To achieved high trapped fields at higher applied fields without flux jumps which will be a vital breakthrough for high magnetic field applications
c) Support the existing simulation studies and reports which helps in giving way for more prospects for high field applications in the development of bulk MgB_2 superconductors.

5.1 Introduction

By virtue of their superconducting state, magnetized bulk superconductors can act as quasi-permanent magnets with the flexibility to come up with magnetic fields of several tesla or larger from a small volume of superconducting material, also as magnetic shields and self-stabilized levitation. Several significant applications were recognized as having a decent market opportunity and being feasible. These fields of applications include portable bulk superconductivity systems, portable high-field magnet systems for medical devices, ultra-light superconducting rotating machines for next-generation transportation and power applications, and magnetic shielding applications for electric machines, equipment, and other high-field devices [1]. In several Nobel reports on other forms of ceramics bulk materials that belongs to the classes of high temperature superconducting bulks, such as REBaCuO bulk superconductors (RE = Y, Sm, Dy, Gd, Eu; RE short for rare earth), are being researched for applications like drug delivery systems (DDS) and magnetic separation, as well as nuclear magnetic resonance (NMR) and semi-permanent magnets. Compared to permanent magnets, bulk superconductors have a number of advantages: Unlike electromagnets, the available field can be up to an order of magnitude higher, and there is no need for a direct, continuous connection to a power supply. Furthermore, unlike wires, tapes and thin films, a sophisticated multi-step processing approach is not required, resulting in a simpler fabrication process. Another advantage is that, unlike

conventional magnets, a bulk superconductor may be turned off safely and easily by merely heating it. [2][3].

To decrease the weak-link behavior at the grain boundary, the melt-texturing technique is required during the production of single domain HTS bulk. The MgB_2 bulk superconductor, on the other hand, has no weak links [4], [5]. As a result, MgB_2 bulk can be made without crystal formation by sintering. In addition, it offers some advantages over HTS bulks, including a homogenous trapped field distribution, inexpensive material costs, and light weight. Furthermore, at 39 K, it possesses the highest critical temperature of all intermetallic compound superconductors. Because of these factors, numerous investigations on the characterization and uses of MgB_2 bulks have been done since Nagamatsu et al. originally discovered MgB_2 in 2001 [6]. The trapped field $B^{FC}{}_T$ has now progressed due to field cooling magnetization (FCM). On a MgB_2 bulk, the strongest trapped field of 5.4 T was recently reported at 12 K [7]. The shortcomings of the ranges of applications are limited by poor mechanical stability, low thermal conductivity and low specific heat of the bulk superconductors. Studies show that to improve the mechanical properties as well as thermal conductivity of a bulk Y-Ba-Cu-O magnet, drilling small holes followed by impregnation of Bi-Pb-Sn-Cd alloy into the superconductor and inclusion of an aluminum wire was reported thereby increasing field-trapping capacity [8], these could be applicable to the numerous ceramic superconductors in existence most especially MgB_2 owing to its very low specific heat.

There are two common ways for magnetizing bulk MgB_2: field cooling (FC) and pulsed field magnetization (PFM). The FC approach may fully leverage a bulk superconductor's flux trapping capabilities; nevertheless, it requires an external field that is greater than or equal to the target field before cooling. As a result, a large diameter superconducting coil magnet is required, which is huge and expensive and eliminates many of the portable benefits gained from the use of bulk materials. The PFM method, on the other hand, is a well-established approach for magnetizing conventional permanent magnets with cost and size benefits [9][10]. The interaction between the external field and the pre-cooled bulk superconductor, on the other hand, occurs in a very short time, often in the tens of milliseconds, making the PFM a quasi-adiabatic process [11]. Rapid flux motion generates a lot of heat, which warms up the bulk superconductor and hence limits the trapped field. [12]. Bulk superconductors as a source of magnetic flux in motors and generators could pave the way for ultra-lightweight, high-power motors with applications in aviation. If the cost and complexity of such motors can be reduced in the future, they may find a larger range of applications [12] [13]. Aside from typical portable high fields, bulk superconducting magnets can be used in medical applications with very particular needs. Bulk superconductors have the potential to carve out a market space between permanent magnet-based systems and massive, expensive superconducting solenoids in low-cost and

portable MRI, for example. Portable bulk-systems' high magnetic fields have the potential to offer novel medical therapies, such as huge field gradients and magnetic drug targeting.

After the precise experiments and simulations on the field trapping behavior, Fujishiro et al. [14] have reported the high trapped field of 1.1 T at 14 K on the MgB_2 bulk magnet fabricated by hot isostatic pressing (HIP) and activation method with use of the split-type coil [15]. Furthermore, the mechanism of field trapping properties was clarified by numerical modelling [16], which referred to the flux jumping during the PFM processes. The highest experimental record at the moment of this study was reported by Hirano et al. [17] which featured large MgB_2 bulk. A trapped field of B_T = 1.61 T was experimentally achieved at the central surface of an MgB_2 bulk composite (60 mm in diameter and 20 mm in height) at 20 K by double pulsed-field magnetization (PFM) using a split-type coil.

Our previous studies reported the time evolutional profiles showing the field trapping and flux jumping behaviors during the PFM processes with respect to the MgB_2 samples with variable thickness [18], [19], and fabrication methods [20]. In this study, we have investigated the detailed flux motion profiles and the resultant trapped field performances with employing the different fabrication methods. Furthermore, we discuss on the unexpected flux jumping phenomena during the PFM processes to promote the field trapping ability. Here we present an enhanced-fabrication treatment that improves the thermal conductivity of our bulk MgB_2 sample, thereby increasing its field-trapping capacity. Small holes drilled into the center of the bulk allows impregnation of U-alloy into the superconductor and inclusion of an aluminum wire support, which results in a significant enhancement of thermal stability and internal mechanical strength. As a result, 0.70 T at 14 K could be trapped at applied field of 1.8 T despite the bulk's low critical current density, bulk density, and without fracturing our pristine bulk MgB_2 sample of 19.6 mm diameter and 1.45 gcm^{-3} density.

5.2 Experimental Procedure

This section summarizes the methodology involved in this section. It is completely different from the methods employed in our previous chapters which were all about the material development and hence the potential applications in this section. The experimental methods employed here are in two stages, the sample preparation stage and the trapped field measurements stage.

5.2.1 Preparation of MgB_2 bulk samples

In this section, we employed MgB_2 bulk sample selected from a previously fabricated set of samples which were synthesized by spark plasma sintering (SPS) in CRISMAT France. Table 5.1 shows the information about parameters of the materials used in fabrication of our bulk MgB_2. This sample is a pristine MgB_2 bulk without any additives. The precursors were sintered by SPS with applying pressure of 75 MPa and heat-treated at 950 °C for 1 min. More details about the sample used in this chapter can be found in some reports [21]. Our sample of 1.45 g/cm^3 density was considered

for this study with the secondary aim of improving the mechanical strength of the bulk and subjecting it to pulse field magnetization. However, some other samples fabricated along with the sample adopted here showed high densities but were not employed for the experiments because of the occurrence of cracks during the drilling process of machining. Perhaps it will be very helpful to consider more high density samples and apply more careful handling in the machining process in the future. This will be later considered for further studies in subsequent works.

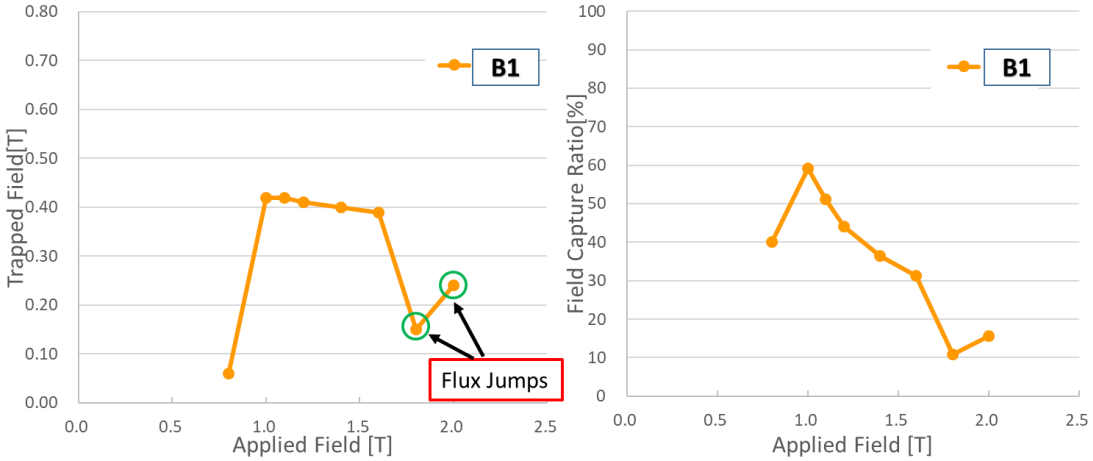

Figure 5.1; Applied field dependence of (a) trapped field B_T and (b) Field capture ratio (%) for the as-received bulk MgB_2 sample at 14 K.

Table 5.1. Characteristic parameters of the materials used in fabrication of the bulk MgB_2 composite. Information on U-alloy properties was obtained from the maker, Asahi metals co., Japan.

Material Type	U-alloy 78	MgB_2 (bulk)	Aluminum
Composition	Bi, In, Sn	Mg, B	Al
Density (g/cm^3)	8.69	1.45 [21]	2.7
Melting Point/ Sintering Temp.(K)	351.8	1223	933.3
Specific Heat (kJ/Kg.K)	0.17	2.7×10^{-6} normal state [22]	0.91
Thermal Conductivity (W/m.K)	9.6	$\approx 2.5 \times 10^{-3}$ [23]	237

The bulk sample used in this chapter had a diameter of 19.6 mm and a height of 12.2 mm, this was the as-received sample named as B1. The as-received bulk sample was initially subjected to pulse field magnetization in which the data is already available in reported literatures, we also included the experimental data obtained in Figure 5.1 for purpose of comparison with the new bulk design.

5 holes were drilled on the bulk in a pentagonal orientation, the aim here is to be able to ensure even distribution of the holes on the bulk. Since it is a manual drilling method, it was important to be more careful when determining the number of holes to be drilled. The 5 holes around the perimeter and the center were all having an average diameter of 2.3 mm. The sample preparation stage took place in three phases, first is the drilling process, second is the impregnation of the drilled holes with

the low melting alloy at around 90°C. Aluminum foils were placed on the bulk to prevent surface deterioration during machining, trapped air was removed from the sample by vacuum. The solidified composite surfaces were polished and subjected to pulse application, the sample design was referred to as B2. The last stage is the insertion of aluminum rods to further improve the heat dissipation from the sample median and then machining. To also improve thermal contact between aluminum wires and the MgB_2, the bulk was still impregnated with U-alloy at 90 °C and any trapped air was removed under vacuum atmosphere. The aluminum rods inserted into the bulk were 2.0 mm in diameters. The process was followed by polishing of the sample surface before subjecting to pulse field magnetization.

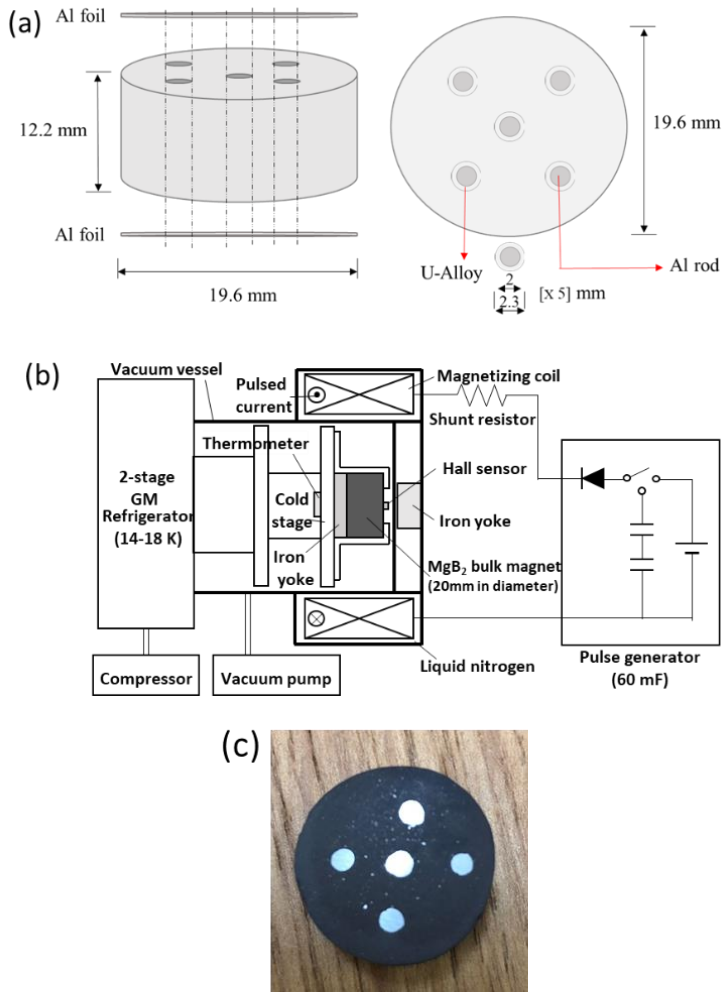

Figure 5.2. (a) Schematics of the modified bulk composite (b) Schematic diagram of pulse the magnetizing system (c) MgB_2 bulk composite sample after machining.

The composite bulk was then referred to as B3 in which pulse was applied in uniform manner as the first two stages. The schematics of assembled composite bulk is shown in Figure 5.2(a). The pulse magnetizing system is illustrated Figure 5.2 (b). In the meantime, the as-received sample was named B1, the drilled sample with alloy impregnation was named as B2, and the final sample design with drilled holes impregnated with U-alloy and aluminum rods inserted was named B3. To aid proper understanding of the schematics of the assembled sample composite, a pictorial representation is

provided in Figure 5.2 (c).

Earlier reports by Murakami et al [8] show significant enhancement of thermal stability by drilling small holes into the center of a YBCO bulk magnet to allows impregnation of Bi-Pb-Sn-Cd alloy into the superconductor and inclusion of an aluminum wire support, which results in higher trapped field of 17.24 T. In this study, the effect of the low melting alloy and aluminum rod embedded in a composite bulk is believed to promote the heat transfer in the MgB_2 sample employed in this work.

5.2.2 Pulsed Field Magnetization and Magnetic Flux Motion

This section discusses the stepwise stages involved in the measurements of the trapped fields. The respective stages of pulse field magnetization, PFM was applied in separate regime of the bulk's designs, B2 and B3, however, since we already mentioned that B1 is an already existing data from our earlier reports in [20]. This was added for the purpose of comparative study of the performance of the bulk MgB_2. At each phase, the sample was magnetized by employing the 2-stage Gifford-McMahon (GM) refrigerator, which are capable of cooling the cold head to 14 K. In addition to this component, an iron yoke was placed between the samples and the cold stage to attract magnetic flux.

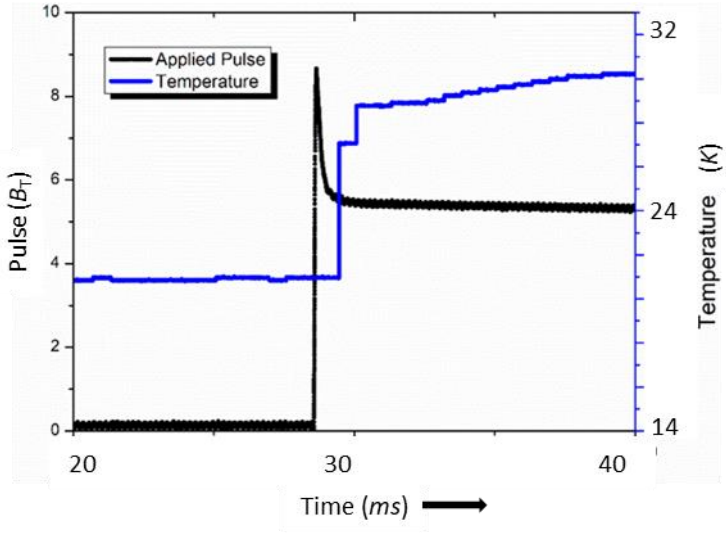

Figure 5.3. Illustration of temperature rise after pulse application

The thermal contact conductance between both the bulks and the iron yoke and the iron yoke and the cold stage compensated for 99.9% pure indium sheets. The temperature data illustrated in Figure 5.3 shows the effect of the resulting pulse application on the temperature read by the temperature sensor. The initial cold stage temperature rises with the corresponding pulse application denoted on the data presented in Figure 5.3. However, this can proof that there was corresponding rise in temperature according to the demonstrated data. Even though the surface temperature shows initial surface temperature around 20 K before it rises to around 30 K, it becomes very easy to establish the relationship between the applied pulse and the effect on the temperature given by the data recorded on the temperature sensor.

The GM refrigerator cooled the samples to the lowest temperature of 14.0 K. Figure 5.1(a) shows the illustration of the experimental setup for the pulse field magnetization. The magnetic field data

were measured at the center of the bulk surface by a Hall sensor (DECO, BHT-921). The parameter B_P/B_A and B_T/B_P represents the penetrated field ratio and trapped field ratio; B_P denotes the highest penetration field measured by the Hall sensor at the center of the bulk surface during the PFM process. B_T denotes the final trapped field after PFM. The value of B_A means the peak value of applied field, which were calculated from the voltage at the shunt resister. The ratio of B_T/B_p indicates the field-trapping ability at the end of the PFM, and is strongly affected by the generation of heat and its propagation in the bulk sample. The applied pulse fields of 0.8 - 2.0 T with a rise time of 10 ms were applied by feeding current from 60 mF condenser to the cryo-cooled bulk MgB_2 samples with use of 112-turn copper coil. The coil is cooled in the liquid nitrogen vessel to reduce the resistance, as also demonstrated in our earlier reports. The coil constant is 1.26 mT/A. Respective stages of the applied fields are characterized by successive heating and cooling of the cold stage for smooth transitions between superconducting and normal state before each subsequent PFM measurements.

5.3 Trapped Field Measurements

Experimentally, several techniques are used to trap the maximum possible field in a given practical application. However, regardless of the magnetization method used, there is a physical limit to the maximum magnetic field that a given superconducting magnet can trap. This limit is given by the geometric design, the particular superconducting material used and the temperature of operation. Knowing the maximum possible trapped field is important for device design as it provides an upper limit for applications such as magnetic bearings or rotating machinery. In this work we used the single pulse method on the drilled MgB_2 impregnated with low melting alloy and Al rod which could be capable of estimating the maximum trapped field without degradation of the trapped field after pulse application.

5.3.1 Flux Penetration and Field Trapping

Figure 5.4(a) and (b) respectively shows the applied field dependence of the penetration field B_P and resultant trapped field B_T. The observed penetrated field in 5.4(b) almost linearly increases with increasing field after the invasion started at 0.8 T for sample B3. The flux invasion occurs almost proportional to applied field with the threshold value at 1.0 T. The initially observed magnetic shielding in B1 tends to disappear gradually with the elimination of the shielding effect in B3. This implies that the applied field overcomes the shielding effect on the bulk magnet surface due to the impregnation of the U-alloy and aluminum rods forming the bulk composite and hence the improved the field trapping capability of the bulk sample. In Figure 5.4(a), the trapped field grows up to 0.41 and 0.70 T for B2 and B3 respectively at 1.8 T applied field without showing any flux jumps for B2 and B3. We can say the occurrence of flux jump at sample stage B1 was eliminated due to the improved thermal conductivity which help to removed most of the heat generated from within the bulk. The data also shows evidence of field trapping ability in the high-field application. However, the decay of the trapped field was observed for all stages of the samples at 2.0 T applied field. These

flux jumps degrade the trapped, even though the penetration field still increases which also means more heat generation. The flux jump regions are indicated by small circles in Figure 5.4(a) which shows the happening of flux jumps on the way of descending stage of PFM. The trapped flux cannot withstand dissipation in the region of greater than 1.8 T at this time.

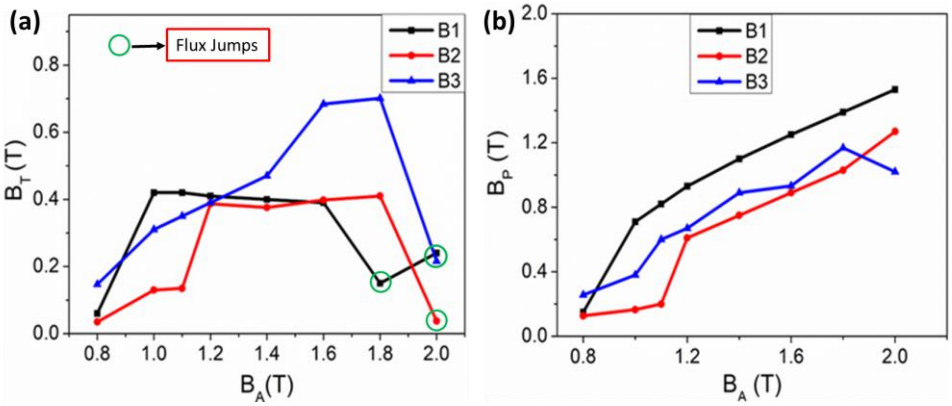

Figure 5.4. Applied field dependence of (a) trapped field B_T and (b) penetration field B_P at 14 K

5.3.2 Penetration Ratio and Field Capture Ratio

Figure 5.5 shows the penetration ratio which is defined by B_P/B_A and field capture ratio B_T/B_P. This also corresponds to the data discussed in Figure 5.3. As shown in Figure 5.5(a), the data of penetration ratio were kept constant around ≈ 80% for B1 for applied field exceeding 1.0 T indicating that the applied field effectively penetrated the sample, this could be another evidence of the resultant heat generation.

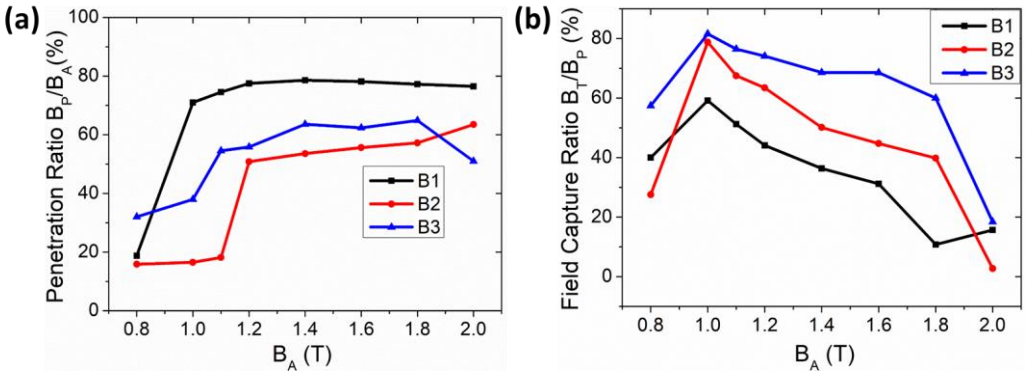

Figure 5.5: Applied field dependence of (a) penetration ratio and (b) field capture ratio at 14 K.

In Figure 5.5(b), the trapping ratio reached 51.2%, 78.8%, 81.6% at 1.0 T for B1, B2 and B3 respectively. At 1.0 T applied field, all the sample stages experienced the least heat generation compared to the other applied field values. These values dropped smoothly with increasing applied field until 1.8 T, at which point flux leaps appeared. The decay of the captured fields at increased applied field was more drastic in the sample B1 and B2, however, B3 showed more improvement in the field capture ratio in the sense that the captured ratio values were sustained above 70% until about

1.8 T. We can easily deduce from the captured field ratio data that the inclusion of the U-alloy and aluminum rods contributed to the magnitude of the captured fields at higher applied fields which is sequel to the heat dissipation in the bulk sample.

5.4 No Flux Flow (NFF) and Fast Flux Flow (FFF) Regions

The dependence of the field capture ratios can also be attributed to three significant regions as shown in Fig. 5.6. The first region is the no flux flow (NFF) region of maximum efficiency of the respective trapped fields of B1, B2, and B3. The NFF zone is an indicator for the best flux trapping with the least amount of heat generation. The fast flux flow region (FFF) shows that the trapped fields are slowly degraded by the fast flux motion followed by heat generation. After the FFF region, flux jumps occur suddenly and at a high rate, causing critical heating in the flux jump regions. In the 1.2–1.8 T applied field range, the FFF area shows linear-like decreases in trapping ratios with no flux jump. The fast flux flow, which appears soon after the peak of B_P, increased heat generation with increasing applied field, resulting in a drop in the ratio B_T/B_P. The other is the area where, due to increased heat output, the observed flux jump reduces the respective trapping ratio to 15.7%, 2.8%, and 18.4% at 2.0 T.

Corresponding to the flux trapping property in Figure 5.3(a), the time evolution profiles were exhibited in Figure 5.6. In the B_A = 1.0 T regions, the invasion keeps the values of about 60% for B1 which was the highest trapping ratio for all the different experiments. The 1.0 T region seems to be the optimize applied field in all sets of the experiments. In contrast, the rapid descend in the decay of B1and B2 owe its effect to the inhomogeneous dissipation of heat generated during PFM, but we observed the gradual and slow decay of the trapped field ratio in B3, perhaps we can also claim that the improved thermal property due to aluminum rod inclusion paved way for a smooth heat dissipation regime. In the region beyond 1.0 T applied fields, the trapped fields are unstable, showing the drop in the captured fields on the way of descending stage of PFM. The drastic changes by trapped field decay may have also resulted in the low trapping ratio beyond the 1.8 T applied field regions.

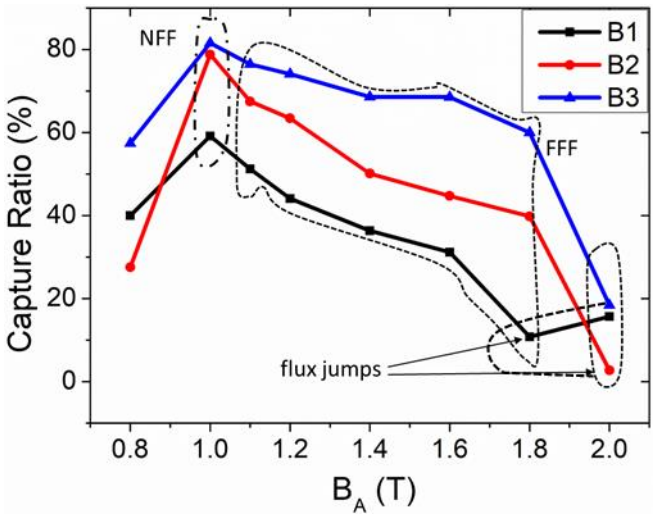

Figure 5.6: Field capture ratio indicator for the FFF and NFF regions at 14 K

In Figure 5.7 we show the high applied field performance of trapped fields. Even though the elimination of the flux jump at high field of 1.8 T as seen in B1 was eradicated in B2. The apparent position of the trapped field without flux jump as indicated by dotted lines in Figure 5.7 shows the real trapped field position of B2 at 1.8 T would've been almost the same as the case of B2 sample at the same applied field, we could ascertain this position by looking at the time evolution profiles which shows the decay in the field captured ratio of B1 down to 10.8% as a result of the flux jump. However, the peak positions for the maximum trapped field in all three experiments B1, B2, B3 were indicated by the green circles on their respective positions of 1, 2, and 3 with the highest trapped field of 0.70 T observed in B3 at 14 K. The improved trapped field performance at higher field was seen in B3 which was the sample embedded with both aluminum and U-alloy. The secondary high trapped field point added on B3 is an indicator for the best performance at high applied fields. The gradual improvement in the trapped field regime occurred almost linearly between 1.1 T and 1.8 T applied fields with its peak at 1.8 T of B_A.

The corresponding time evolution profiles in Figure 5.7 further explains the phenomena of the flux motion behaviors of the high field regions in the respective stages of the different sample designs. Further details about flux motion in the high B_A regions could be explain more clearly in Figure 5.7. As explained earlier, the penetrated flux kept its intensity with no flux flow at 1.0 T of B_A for both B2 and B3. This means that the ideal PFM without heat generation was accomplished in this manner. In Figure 5.8, The time evolution profiles show the overall NFF and FFF regions in both B2 and B3. The FFF regimes gives us more insight on the possible interpretations for the amount of heat dissipations in the selected time evolution profiles.

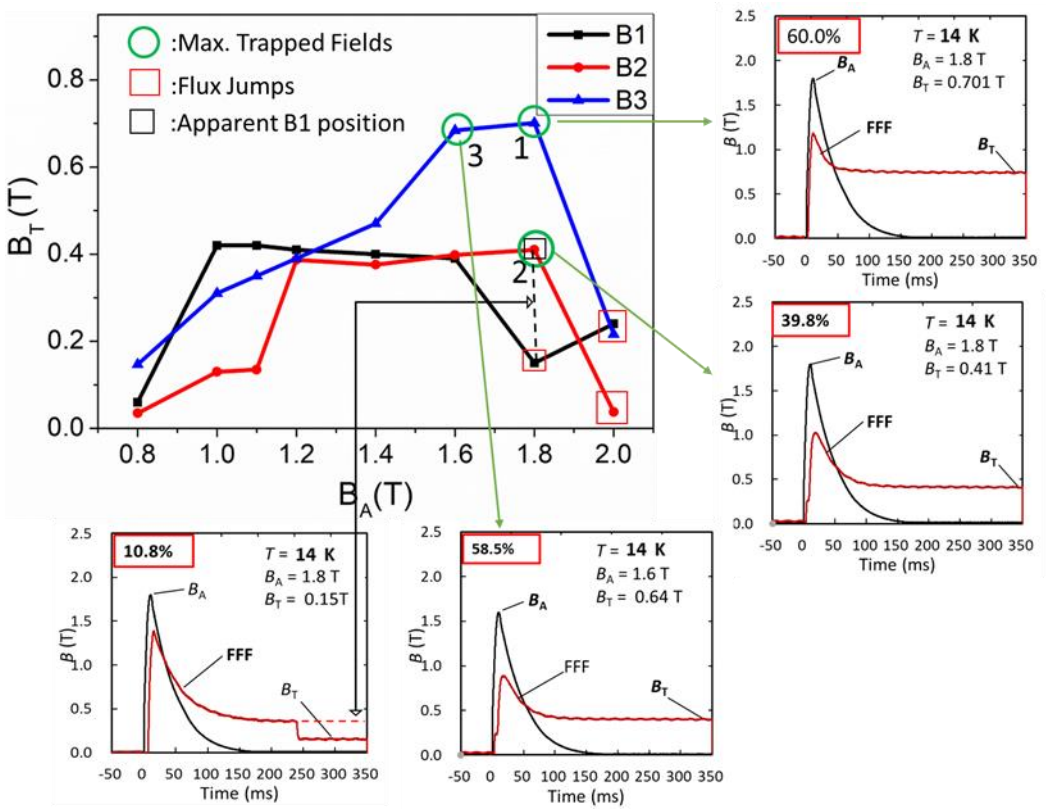

Figure 5.7: Time evolution profiles relating to field dependence at high applied fields

The low field trapping areas are associated with the FFF regions due to the fast degradation of the trapped field which is mostly seen in sample B2 than B3. This implies that the values of trapping ratio descended more at higher applied fields due to the heat generation caused by the fast flux flow. However, the highest trapping ratio at 1.0 T suggests us the effective field trapping up to 78% without any heat generation. Sample B3 show more NFF regions which could be due to the contribution of the heat dissipation from the sample median. This may also suggest the homogeneous heating which occurs at the very beginning of flux invasion for the B3 sample.

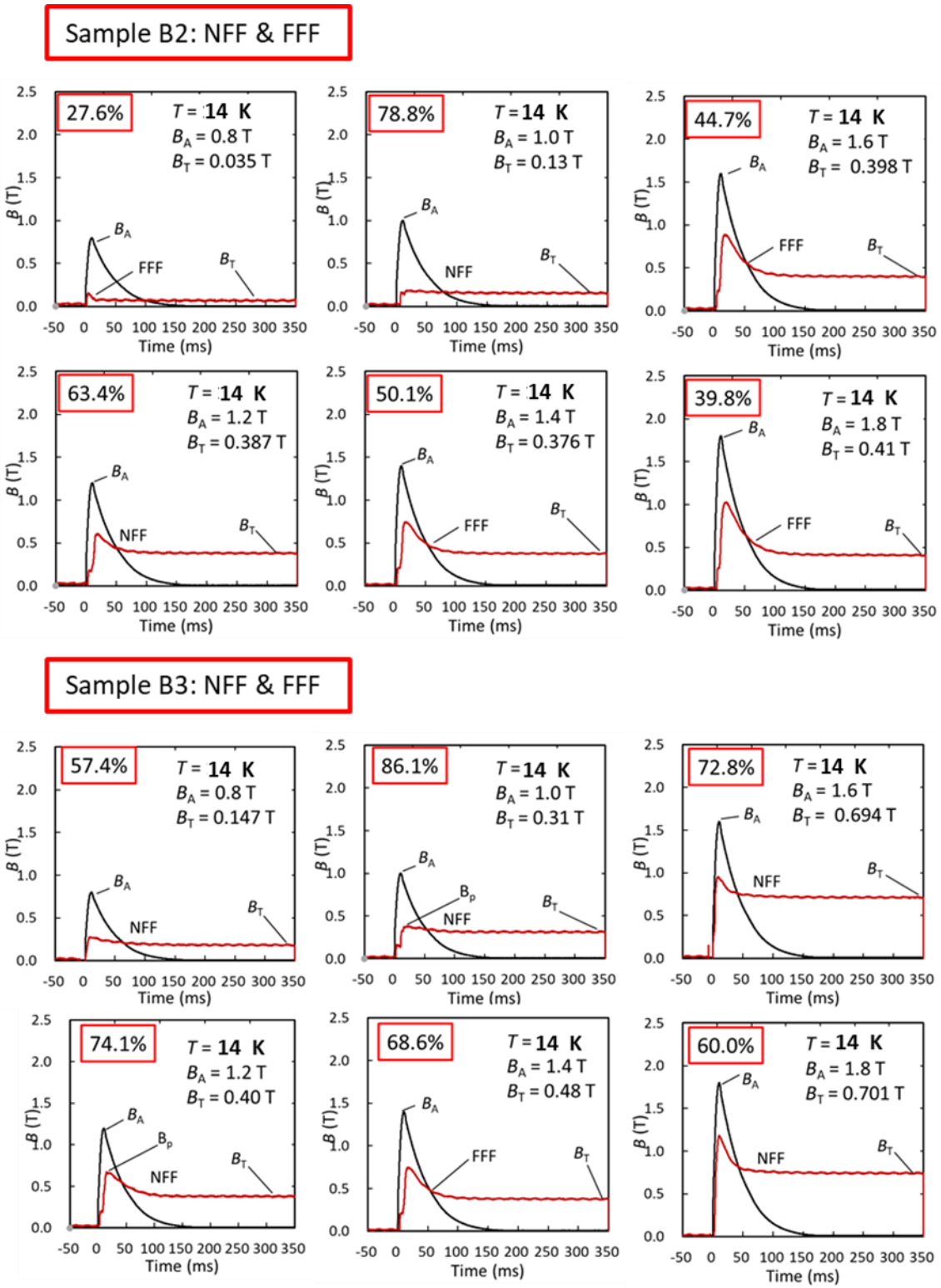

Figure 5.8: NFF and FFF regions for B2 and B3 samples at low and high applied fields

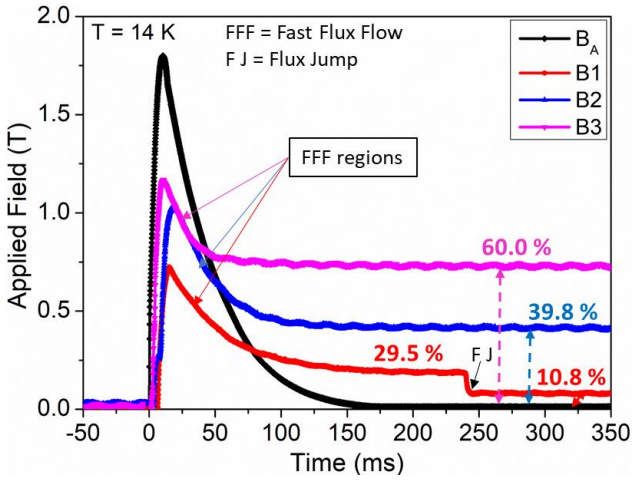

Figure 5.9: Time evolution of the applied field B_A(t) and local fields B1, B2, B3 (t) at the center of the bulk surface for B_A=1.8 T at 14 K

However, in Figure 5.9, the time evolution profiles show the FFF regions in all three sample conditions at 1.8 T of B_A. The FFF regimes gives us more insight on the possible interpretations for the amount of heat dissipations in the selected time evolution profiles. The low field trapping areas are associated with the FFF regions due to the fast degradation of the trapped field which is mostly seen in sample B2 than B3. This implies that the values of trapping ratio descended more at higher applied fields due to the heat generation caused by the fast flux flow. The occurrence of flux jumps in B1 which resulted in the degrading of the trapped field B_T/B_p at 10.8% was prevented by the alloy impregnation in B2 by subsequently improving the ratio to 39.8%. This also implies that the highest trapping performance at 1.8 T B_A suggests to us the effectiveness of the B3 bulk design which later increased the B_T/B_P up to 60% without any heat generation at 1.8 T of B_A for bulk the bulk design. The flux jump after the FFF region was however prevented, this may also suggest the homogeneous heating which occurs at the very beginning of flux invasion for the B3 sample.

5.5 Summary On Trapped Field Measurements

This chapter presented the effect of pulse field magnetization at 14 K on our improvised design of MgB_2 bulk embedded with low melting alloy and aluminum rods. The heat dissipation in the enhanced bulk was successfully improved resulting in the highest flux trapping of 0.70 T at 1.8 T of B_A without flux jumps compared to the as-received bulk sample. The regions of fast flux flow and flux jump regions were similarly observed in all stages of the bulk design. Appearance of fast flux flow degraded the trapped field dependence at high field, but one could see no fast flux flow observed in the low field area of 0.8–1.0 T with high trapping ratios up to 86.1 %. This means no substantial heat generated in the low field region. Making such a composite can be exploited to enhance the trapped field of MgB_2 because of the intrinsic thermal property which was much bigger than the anisotropic thermal property of the bulk MgB_2.

i. The trapped field was enhanced even at higher applied field without flux jumps for the improvised bulk designs. The high trapped fields observed at 1.8 T for the three types of bulk composite were observed to be B_T = 0.41 T for the composite with U-alloy and, finally to B_T = 0.7 T for the composite with U-alloy and aluminum rods. The inserted aluminum rod can be exploited to enhance the trapped field of MgB_2 because of the intrinsic thermal property which was much bigger than the anisotropic thermal property of MgB_2.

ii. In all three sets of sample studies, the fast flux flow and flux jump zones were investigated in the same way. However, compared to the as-received sample and the sample with only U-alloy impregnation, the region of the sample with U-alloy and aluminum migrated to a higher field. Fast flux flow appeared to diminish trapped field performance, however no fast flux flow was seen in the low field area of 0.8–1.0 T with high trapping ratios up to 86.1 %. This means that no significant heat is produced in the low field region.

References

[1] J. H Durrell, M. D Ainslie, D. Zhou, P. Vanderbemden, T. Bradshaw, S. Speller, M. Filipenko and D. A Cardwell "Bulk superconductors: a roadmap to applications" Supercond. Sci. Technol**. 31** (2018) 103501

[2] R. Weinstein, I.-G. Chen, J. Liu, and K. Lau, "Permanent magnets composed of high temperature superconductors," J. Appl. Phys. **10** (1991) 6501–6503

[3] M. Murakami, "Processing and applications of bulk RE-Ba-Cu-O superconductor," Int. J. Appl. Ceram. Technol., **3** (2007) 225–241.

[4] M. Muralidhar, A. Ishihara, K. Suzuki, Y. Fukumoto, Y. Yamamoto, and M. Tomita, "Optimization of the fabrication process for high trapped field MgB_2 bulks," Physica C, vol. **494** (2013) 271–350.

[5] M. Eisterner, "Magnetic properties and critical currents of MgB_2," Supercond. Sci. Technol., **12** (2007) 47–73.

[6] J. Nagamatsu, N. Nakamura, T. Muranaka, Y. Zenitani, and J. Akimitsu, "Superconductivity at 39 K in magnesium diboride," Nature, **410** (2001) 63–64.

[7] G. Fuchs, W Häßler, K Nenkov, J Scheiter, O Perner, A Handstein, T Kanai, L Schultz and B Holzapfel "High trapped fields in bulk MgB_2 prepared by hotpressing of ball-milled precursor powder," Supercond. Sci. Technol. **12** (2013) 122002.

[8] M. Tomita and M. Murakami "High-temperature superconductor bulk magnets that can trap magnetic fields of over 17 tesla at 29 K Nature **421** (2003) 517-520.

[9] Y. Yanagi, M. Yoshikawa, Y. Itoh, T. Oka, H. Ikuta and U. Mizutani "Generation of extremely strong magnetic fields in open space by using metal-ring-reinforced 60 mmØ Sm–Ba–Cu–O superconducting bulk" Physica C **9** (2004) 412–414

[10] N. Saho, N. Nishijima, H. Tanaka and A. Sasaki "Development of portable superconducting bulk magnet system" Physica C **469** (2009) 1286–9

[11] T. Nakamura, D. Tamada, Y. Yanagi, Y. Itoh, T. Nemoto, H. Utumi, and K. Kose "Development of a superconducting bulk magnet for NMR and MRI" J. Magn. Reson. **259** (2015) 68–75

[12] M. Tomita, Y. Fukumoto, A. Ishihara, T. Akasaka, H. Ohsaki and M. Sekino "Evaluation of temperature dependence of magnetic field distributions of bulk superconductor annuli" IEEE Trans. Appl. Supercond. **26** (2016) 8801304

[13] D. Zhou, M.D. Ainslie, Y-H. Shi, A.R, Dennis, K.Y. Huang, J.R. Hull, D.A. Cardwell and J.H. Durrell "A portable magnetic field of >3 T generated by the flux jump assisted pulsed field magnetization of bulk superconductors" Appl. Phys. Lett. **110** (2017) 062601

[14] H. Fujishiro, T. Naito, T. Ujiie, A. F. Albisetti, and G. Giunchi, "Trapped field and flux dynamics in MgB_2 superconducting bulks magnetized by pulsed field," Phys. Procedia, vol. **58**, (2014) 286–289.

[15] H. Fujishiro, H. Mochizuki, M. D. Ainslie, and T. Naito, "Trapped field of 1.1 T without flux jumps in an MgB_2 bulk during pulsed field magnetization using a split coil with a soft iron yoke," Supercond. Sci. Technol. **29** (2016), 084001.

[16] M. Ainslie, D. Zhou, H. Fujishiro, K. Takahashi, Y-H. Shi, and J. H. Durrell, "Flux jump-assisted pulsed field magnetization of high-J_c bulk High-Temperature superconductors," Supercond. Sci. Tech. **29** (2016), 124004.

[17] T. Hirano, Y. Takahashi, S. Namba, T. Naito and H. Fujishiro "A record-high trapped field of 1.61 T in MgB_2 bulk comprised of copper plates and soft iron yoke cylinder using pulsed-field magnetization" Supercond. Sci. Technol. **33** (2020) 085002

[18] T. Miyazaki, S. Fukui, J. Ogawa, T. Sato, T. Oka, J. Scheiter, W. Haßler,¨ . Kulawansha, Z. Yuanding, and K. Yokoyama "Pulse-field magnetization for disc-shaped MgB_2 bulk magnets," IEEE Trans. Appl. Supercond. **4** (2017), 6800504

[19] T. Oka, A. Takeda, S. Sasaki, J. Ogawa, S. Fukui, T. Sato, J. Scheiter, W. Häßler, J. Katsuki, A. Miura, K. Yokoyama, "Magnetic flux invasion and field-capturing in pulsed field magnetization for layered MgB_2" IEEE Transactions on Applied Superconductivity, **28** (2018) 4.

[20] T. Oka, A. Takeda, H. Oki, J. Ogawa, S. Fukui, J. Scheiter, W. Häßler, K. Yokoyama, K. Yamanaka, L. Dadiel, M. Miryala, N. Sakai, M. Murakami, and J. Noudem "Study on Magnetic Flux Dissipation and Field-Trapping Performance of HTS Bulk-Shaped Magnesium Diboride in Pulse-Field Magnetizing Processes" IEEE Transactions On Applied Superconductivity, **29** (2019) 5

[21] N Sakai, T Oka, K Yamanaka, L Dadiel, H Oki, J Ogawa, S Fukui, J Scheiter, W Häßler, K Yokoyama, J Noudem, M Miryala and M Murakami" Occurrence of Flux Jumps in MgB_2 Bulk Magnets During Pulse-Field Magnetization" J. Phys.: Conf. Ser. **1559** (2020) 012024

[22] Y. Wang, T. Plackowski, A. Junod "Specific Heat in the Superconducting and Normal State (2-300 K, 0-16 T) and the Magnetic Susceptibility of the 38 K Superconductor MgB_2" Physica C **355** (2001) 170-193

[23] E Bauer, Ch Paul, St Berger1, S Majumdar, H Michor1, M Giovannini, A Saccone, and A Bianconi "Thermal Conductivity of Superconducting MgB_2" J. Phys.: Condens. Matter **13** (2001) L487–L493

CHAPTER VI

6.1 Conclusion

This thesis basically focused more on two aspects, first is the MgB_2 bulk material processing which explain the processing techniques of improving the superconducting performance of polycrystalline and high density magnesium diboride (MgB_2) as well as the effective cost of production, the second aspect drives us towards practical applications of bulk MgB_2 by study of the magnetic trapped fields. This intermetallic material is highly attractive for practical applications because of its excellent and unique features which ranges from it's simple stoichiometry and high critical temperature for a non-oxide superconductor, low density, high upper critical field and strong trapped field among other features for the samples produced in the bulk form. Several techniques have been suggested and researched to improve the density and connectivity, grain sizes with the resulting effect on the critical current density (J_c), to be utilized for practical applications of the bulk such as magnetic resonance imaging (MRI), nuclear magnetic resonance, trapped field magnets, motors and generators, magnetic separations, flywheel storage, levitation, innovative applications such as biomedical. Classically, most of the samples prepared by conventional powder metallurgy leads to low relative densities which affect the final properties of the bulk materials. Different methods have been used for enhancing the grain refinement, connectivity and densifying the material such as high pressure sintering, hot isostatic pressing (HIP), hot compactions, and nonconventional field assisted sintering techniques (FAST) or spark plasma sintering (SPS) process. However, the challenges in the optimization of the microstructures and material density for effective self-field J_c improvement and high trapped field is still at large.

As a remedy to the aforementioned issues, we suggested possible methods in this thesis to enhance the connectivity between grains in order to improve the bulk superconducting performance. In the material aspect of this thesis, the chemical doping technique was initially adopted to improve the flux pinning properties of MgB_2 bulk superconductor material as discussed in chapters 3, 4, and 5. These techniques were effective for the samples produced at the course of this project. This first series was based on nanoscopic diamond powder addition discussed in chapter 3. Optimization of the nanoscopic diamond powder at 775 ^oC sintering temperature for 3 hours played a vital role in improving the flux pinning performance of the bulk MgB_2 material resulting in high self-field J_c at ~300 kA/cm^2 for 0.8 wt.% of nanoscopic diamond addition. To further improve the superconducting performance of the bulk which is explained in chapter 4, we synthesized the product by silver (Ag) addition using the same processing technique and conditions. XRD and SEM micrograph analyses indicated AgMg secondary phase as nanoparticles embedded in the MgB_2 matrix in the samples with Ag addition. Optimization was achieved for 4.0 wt.% added Ag which showed improved self-field J_c of 398

kA/cm^2 at 20 K. The study showed Ag addition contributed to formation of more effective pinning medium in bulk MgB_2 and helps to further improve performance of the bulk. Nano-diamond and Silver are very expensive raw materials used for bulk MgB_2 synthesis in chapters 3 and 4 and we proposed a target to make the final product costlier. To solve this problem, we employ a cost effective technique in chapter 5 by doping of MgB_2 with ball-milled charcoal powder within the range of 60-100 nm sizes. The resulting optimization at 0.4 % charcoal doping was realized for a superconducting J_c improvement to about 467 kA/cm^2. Charcoal is a cheap source of carbon which could be manufactured by simply oxidation of organic materials (in our case wood).

We achieved successfully developed methods for improving our bulk MgB_2 in previous chapters, however, the density of our final product is an issue to be tackle for the purpose practical applications in real time. In order to achieve high performance by simultaneous structural control and density enhancement of bulk MgB_2 for practical applications, in chapter 6, we synthesize bulk MgB_2 samples via spark plasma sintering *in-situ* for the first time and also utilized *ex-situ* processing by optimizing the sintering temperatures and observing the effects on the bulk density and microstructure. The microstructural characterization by FE-SEM reveals some MgO and MgB_4 inclusions for the *ex-situ* process, better grain connectivity and the size of the MgB_2 grain was statistically analyzed to be within the range of ~100 to 120 nm. The distribution of the generated impurity phases which occurred due to the effect of our processing condition were studied by transmission electron microscope. The onset of the critical temperature, T_c determined by superconducting quantum interference magnetometer was ~38 K showing slight effect of secondary phases in the sample microstructure. The critical current density, J_c is influenced by the sintering temperature for both *ex-situ* and *in-situ* process exhibiting $J_{c,s}$ of the order ~500 kA/cm^2 at self-field and 20 K. The density by SPS *in-situ* is superior to the previous reports by SPS in-situ processing. We urge that the flux pinning was highly promoted by the interactive contributions of the grain refinements and controlled minor secondary phases towards improving the superconducting performance compared to the bulk MgB_2 synthesized by the conventional methods. To give more understanding of the material development, table 6.1 shows a brief summary of the comparative study for ease of understanding of the chapters.

Table 6.1; Overall comparison of bulk samples fabricated by different techniques employed for the bulk MgB_2 material synthesis in this work.

Optimized Sample	Relative Density (%)	J_c (self-field) at 20 K	F_p	Phases Present	Contribution to Bulk Improvement
Tubular Furnace Sintering Technique					
Undoped MgB_2	~ 66	~278	~0.2	MgB_2	_____
Nano-diamond doped MgB_2	~ 66	~300	~0.2	MgB_2 + small MgO	Improved J_c-B
Charcoal doped MgB_2	~ 66	~460	~0.24	MgB_2 + small MgO	Improved J_c-B
Silver doped MgB_2	~ 66	~390	~0.2	MgB_2 + small MgO + AgMg/AgO	AgMg/AgO inclusions
Spark Plasma Sintering Technique					
In-situ	~ 90	~504	~0.25	Little MgO	Improved density/connectivity
Ex-situ	~ 99	~516	~0.28	Nano-sized MgB_4/MgO	Improved density/connectivity/Nano-size inclusions

To complement the application aspect of our study, we subjected bulk MgB_2 of a larger aspect ratio to trapped field measurements through pulse field magnetization (PFM). Degrading of trapped fields B_T in bulk MgB_2 superconductor due to the occurrences of flux jumps has been a lingering challenge due to the anisotropic thermal property of bulk MgB_2. This section of this thesis as discussed in chapter 7 presents the method for characterizing the propagation of the magnetic flux in an artificially drilled MgB_2 bulk superconductor fabricated via spark plasma sintering (SPS) by studying the effect of applied fields, B_A on the bulk MgB_2 embedded with low melting alloy of Bi-In-Sn alloy and aluminum rods within the holes. The bulk MgB_2 sample was redesigned to enhance both the thermal properties and to suppress flux jumps during pulse applications. We discuss the magnetic flux dissipation, the flux motion, and performance by evaluation of the capture field ratio B_T/B_P. We achieved 0.7 T trapped field at 1.8 T applied field without flux jumps which is a vital breakthrough for high magnetic field applications. This study helps to solve the flux jump problem in the bulk superconductor resulting from poor heat dissipation. This is an experimental breakthrough that supports existing simulation studies and reports giving way for more prospects for high field applications in the development of bulk MgB_2 superconductors. Table 6.2 gives a brief summary of the bulk properties before and after modification.

Table 6.2: Summary of bulk MgB_2 properties with respect to pulse field magnetization

Sample Names	Bulk Enhancement	Flux jumps at high B_A (1.8 T)	Highest Trapped Fields B_T measured	Highest Field Capture Ratio (%)
As-received Bulk	No holes	Present	0.4 T at 1 T of B_A	60 % at 1 T of B_A
Final Modified Bulk	Drilled holes impregnated with alloy and Al rod	Absent	0.71 t at 1.8 T of B_A	86 % at 1 T of B_A

6.2 Future

The available data in in this work shows how promising the prospects will be when room is given for future developments on a novel project as such. The prospects and the implication of our results pave way for more future developments in the field of applied superconductivity. Producing a larger sample by SPS process with improved mechanical and physical properties will further promote the development of larger superconducting magnets which is synonymous to high trapped magnetic fields. In addition, the SPS process is reliable when it comes to producing homogenous bulk samples, hence this will make it easier to design a patent for mass production in the future. The trapped field measurement by PFM can be improved by using a high J_c sample in the future. The 0.71 T trapped field obtained without flux jumps for the sample used in this thesis shows how the bulk MgB_2 material used is of low J_c and density when compared to reported literatures of B_T = 1.1 T, 1.6 T by H. Fujishiro et al (2014) and T. Hirano et al (2020). Trapped magnetic field is proportional to the J_c and also size of the bulk which means higher trapped fields can be measured by employing the methods utilized in this project. We intentionally used a low density bulk sample for our experiment in order to avoid destruction of the sample during machining. It is possible to drill holes by employing suitable machining in the future which will also possibly enhance the trapped magnetic field using this technique when considering large sized and high J_c bulk composite bulk MgB_2 superconductors. With the methods employed in this study, there is a high chance to obtain outstanding results that can contribute greatly to the industrial development of superconducting bulk materials.

List of Figures

List of Tables